INVESTIGATION OF TRANSFER TRAJECTORIES TO PERIODIC HORSESHOE ORBITS

A Thesis

Submitted to the Faculty

of

Purdue University

by

Jayme M. Howsman

In Partial Fulfillment of the

Requirements for the Degree

of

Master of Science in Aeronautics and Astronautics

August 2011

Purdue University

West Lafayette, Indiana

To Mom, Dad, Steph, and Neal.

ACKNOWLEDGMENTS

I would first like to express my gratitude toward my wonderful family. They have always been proud of me and believed in me in all aspects of my life. I am very grateful for everything they have done for me, and this work is dedicated to them. My fiancé, Neal, also deserves recognition, as he has greatly contributed to my success at Purdue. He has been unfailingly patient and supportive of me, and I hope I can offer the same encouragement to him.

I would also like to thank my advisor, Professor Kathleen Howell, for her guidance during my time at Purdue. An opportunity to work with her was a large factor in my decision to come to Purdue, and I am very glad to have made that decision. She is a skilled professor, as well as a thoughtful advisor. Professor Howell has provided instrumental guidance and advice on my research topic, and I am extremely grateful to her for devoting the time to carefully review this thesis. I would also like to express my gratitude to the entire research group for their knowledge and support, and for their friendship around and outside of the office. Everyone in the group has contributed to my completion of this investigation, whether it was through offering suggestions at research meetings, answering questions I have had, or providing invaluable advice and support in preparation of my final examination.

Additionally, I would like to thank Professors James Longuski and Martin Corless for serving on my committee and reviewing my thesis. I have enjoyed learning from each of them as a student, and additionally from serving as Professor Corless's teaching assistant. Finally, my graduate studies were made possible by the generous support of Purdue University. My graduate education was funded through the Purdue University Ross Fellowship and the John L. and Patricia R. Rich Fellowship during the first year, and through a teaching assistantship the second year of my graduate studies.

TABLE OF CONTENTS

Page

LIST OF TABLES

LIST OF FIGURES

Figure Page

ABSTRACT

Howsman, Jayme M. M.S.A.A., Purdue University, August 2011. Investigation of Transfer Trajectories to Periodic Horseshoe Orbits. Major Professor: Kathleen C. Howell.

Horseshoe orbits are both an intriguing natural occurrence in the solar system and a viable option for spacecraft mission design. Several asteroids, as well as a pair of Saturnian moons, are known to occupy horseshoe orbits. Since horseshoe orbits encompass three libration points, L_3, L_4, and L_5, they offer a unique scientific exploration opportunity, as well as the potential for extended-mission options for a spacecraft. Therefore, in this preliminary investigation into transfer trajectories to horseshoe orbits, planar, periodic horseshoe orbits are computed and analyzed in both the Saturn-Titan and Sun-Jupiter systems. Several techniques for computing transfer trajectories between libration point orbits and horseshoe orbits are investigated. Significant variation in maneuver cost and time-of-flight is observed in the various types of transfer trajectories. One of the methods investigated for computing transfers incorporates dynamical systems techniques, and achieves extremely low maneuver costs. This technique utilizes Poincaré maps that reflect the unstable manifolds corresponding to a departure orbit and the stable manifolds computed for an arrival horseshoe trajectory to logically uncover low-cost transfers. For examples in both the Saturn-Titan and Sun-Jupiter systems, cost-free (theoretical) heteroclinic connections are determined between Lyapunov orbits and horseshoe trajectories. The results compiled in this preliminary investigation demonstrate that a transfer to a horseshoe orbit is a feasible option for low-cost mission applications.

1. INTRODUCTION

Humankind has long had a desire both to understand and to explore the universe. In particular, motion in the vicinity of libration points has fascinated scientists ever since Lagrange proved the existence of these solutions in the restricted three-body problem in 1772. With the discovery of a Trojan asteroid in 1906, i.e., 588 Achilles in the Sun-Jupiter system, Lagrange's findings were physically realized. This discovery propelled further investigation into similar stable points in other systems [1]. Less well-known than the orbits typically occupied by Trojan asteroids about the linearly stable L_4 and L_5 points are a related group of orbits known as horseshoe orbits, whose existence was proposed by Brown in 1911 [2], [3]. These trajectories trace paths that encompass L_3, L_4, and L_5 [4]. Several bodies in the solar system are recongnized to move along horseshoe orbits, including a few asteroids. One such asteroid is 3753 Cruithne, whose horseshoe trajectory in the Sun-Earth system renders it a "natural companion" of the Earth [5]. The Saturnian moons Epimetheus and Janus are coorbital satellites which move along horseshoe paths with respect to each other [6]. In addition to describing some naturally occurring motion, horseshoe orbits are also potentially interesting for mission applications. For example, a horseshoe orbit was considered for the Space Interferometry Mission (SIM) mission trajectory [7]. Additionally, with the successful completion of baseline missions, such as the Cassini spacecraft's exploration of the Saturnian system, low-cost trajectories are frequently examined for extended missions or end-of-life scenarios [8], [9], [10]. This investigation addresses the problem of modeling horseshoe orbit behavior, as well as the computation of transfer trajectory costs to determine if such low-cost transfers into horseshoe orbits are feasible.

1.1 Problem Definition

The development of strategies to compute horseshoe orbits as well as transfers to theses trajectories is the focus of this investigation. The study is conducted within the context of the Saturn-Titan and Sun-Jupiter systems, each modeled in terms of the circular restricted three-body problem. This system model is established, then numerical methods are developed to compute periodic orbits and other types of trajectories. Horseshoe orbits are then computed and analyzed for stability characteristics. To aid in the construction of transfer trajectories, invariant manifolds associated with the orbits are determined. Once this necessary background is completed, transfer trajectories are computed that link libration point orbits to horseshoe orbits. Poincaré maps reflecting the invariant manifolds associated with these orbits are also developed as a useful tool for low-cost trajectory design.

1.2 Previous Contributions

Many researchers throughout the years have contributed to an advancement in the understanding of the dynamical behavior in the circular restricted three-body problem. In more recent years, much work has also been devoted to the study of horseshoe orbits. Trajectory design for mission applications is increasing in complexity as more exotic trajectories are explored. A compilation of some of these previous contributions is briefly presented.

1.2.1 Historical Review of the System Model

Sir Issac Newton's *PhilosophiæNaturalis Principia Mathematica* was first published in 1687 [11], and it presented one of the first investigations on the problem of three bodies. In this work, Newton presented his law of gravitation and also unsuccessfully attempted to solve the n-body problem [12]. Euler later studied the problem of three bodies and, in 1772, introduced a rotating coordinate system, which greatly

contributed to the formulation of the restricted problem. Euler predicted the three collinear libration points as particular solutions to the problem, and, in 1772, Lagrange proved the existence of both the three collinear points and the two triangular libration points [13]. In 1836, Jacobi identified an integral of the equations of motion for the restricted three-body problem [1]. This integral is known as the Jacobi integral, and offers significant insight into the motion in this formulation of the restricted problem. In 1878, Hill demonstrated that one important application of the Jacobi integral is bounding regions of motion. He used the concept of zero velocity curves to prove that the Moon is bounded in its orbit around the Earth [13]. Poincaré was a great admirer of Hill and his research and, in 1899, the three volumes of Poincaré's famous work *Les Méthodes Nouvelles de la Mécanique Céleste* were completed, as influenced by Hill [1]. Poincaré made significant qualitative contributions to celestial mechanics, in particular, and is considered by many as the "father" of the geometric approach to dynamical analysis which is now generally labeled dynamical systems theory. In his 1899 work, Poincaré proved the nonexistence of analytical integrals to solve the three-body problem. He also incorporated much analysis on periodic solutions, including the result that an infinite number of periodic solutions exist in the restricted three-body problem [13]. Since the publication of Poincaré's *Méthodes Nouvelles*, many investigators have built on the foundation laid by Poincaré. In 1967, Szebehely published *Theory of Orbits: The Restricted Problem of Three Bodies*, as a comprehensive work on the restricted three-body problem and, over 40 years later, it is still an effectual source of information [1]. With the advent of computers in the 20^{th} century, numerical approaches to examine behavior in the restricted three-body problem have been a highly productive resource; extensive numerical explorations of the problem have increased significantly in the last decade.

1.2.2 Horseshoe Orbits

The concept that serves as the basis for horseshoe orbits was first proposed by Brown in 1911. Brown was unable to justify a restriction on the well-known motion of objects in orbits that surround the L_4 and L_5 libration points, i.e., one that would bound their excursions to the vicinity of an equilateral equilibrium point. He surmised that orbits could exist that sweep out an arc to include L_3, L_4, and L_5 [3]. In 1961, Rabe published a survey of periodic Trojan orbits in the Sun-Jupiter restricted three-body problem based on a Jovicentric coordinate system. In this publication, Rabe computes trajectories that enclose only one equilateral point and then extends the analysis to compute horseshoe-shaped periodic orbits that encompass L_3, L_4, and L_5. Particular attention is focused on the horseshoe orbits since they link the equilateral libration points with the region containing Jupiter's moons [14]. In 1967, Schanzle published numerical results in which an alternate technique for computing horseshoe orbits is presented, incorporating a barycentric system. Schanzle produces a family of periodic horseshoe orbits that originates from a horseshoe computed by Rabe [15]. In the 1979 paper by Dermott *et al.*, the phenomenon responsible for the narrow widths and sharp edges of the rings of Uranus is investigated. At the time, the researchers proposed that a small satellite, with associated nearby particles, moves along a horseshoe orbit that is contained in each ring and is responsible for the behavior. Then, in 1981, Taylor demonstrated that smooth horseshoe orbits belong to multiple families, as opposed to the previous view that all smooth horseshoes belong to one natural family [16]. Also in 1981, Dermott and Murray published two articles on horseshoe orbits. The first uses numerical and analytical methods to explore the properties of tadpole orbits (that enclose only one of the equilateral libration points) and horseshoe orbits; the long-term stability of horseshoe orbits is also investigated [4]. In the second paper, the coorbital motion of two Saturnian satellites, Janus and Epimetheus, is investigated. These satellites move along horseshoe orbits with respect to each other and, in their case, the mass of the third particle in the three-body

problem is not negligible [6]. Llibre and Ollé also studied the motion of these coorbital satellites and presented a systematic method for computing periodic horseshoe orbits in 2001 [17]. Since 1997, research involving horseshoe orbits has gained support due to the discovery of several asteroids that apparently move in horseshoe-shaped orbits in the Sun-Earth system [5], [2], [18]. More recently, Barrabés and Mikkola computed families of both planar and three-dimensional periodic horseshoe orbits in 2005 [19]. Later, in 2006, Barrabés and Ollé studied horseshoe orbits from the perspective of homoclinic orbits to L_3 [20], and, along with Mondelo, extended this research to include period-n horseshoe-shaped homoclinic orbits in 2009 [21].

1.2.3 Transfer Trajectories

A primary goal in this investigation is the development of transfer trajectories from orbits in the vicinity of the libration points to horseshoe orbits. In a mission application, before such a transfer can occur, a spacecraft must first reach the vicinity of the libration point. In 1974, D'Amario and Edelbaum first detailed a method for computing optimal impulsive transfers between the Moon and L_2 in the Earth-Moon system [22]. In more recent years, there has been an emergence of research into transfers that exploit the natural dynamics of invariant manifolds. In 1992, Gómez *et al.* completed a study of transfers from the Earth to a halo orbit around L_1 that employ stable manifolds [23]. Many other investigations utilizing invariant manifolds for trajectory design have since been produced [24], [25], [26]. In this investigation, trajectories that reach the vicinity of the libration points are not considered. However, transfers from libration point orbits to horseshoe orbits that incorporate invariant manifolds are investigated.

1.3 Overview of Current Research

A major focus of this investigation is the examination of potential transfer trajectories between libration point orbits and horseshoe orbits. To complete this task,

background on the system model, numerical computation techniques, and horseshoe orbits are first explored. This investigation is arranged into the following chapters:

- Chapter 2: The system model used to compute orbits in this investigation is the Circular Restricted Three-Body Problem (CR3BP). The equations of motion for this system are developed originating with the general representation of the n-body problem, and an integral of the motion is defined. Equilibrium solutions to the CR3BP equations of motion are computed. Once the equilibrium solutions are identified, the equations of motion are linearized relative to these solutions, and approximate linear motion near these points is investigated. Bounds on the motion of the infinitesimally small body in the CR3BP are established with the investigation of zero velocity surfaces. To relate the CR3BP motion, which is typically viewed in a rotating frame, to an inertial frame, a transformation between these two frames is presented.

- Chapter 3: Numerical methods to compute orbits in the CR3BP are discussed. First, the state transition matrix is introduced. Then a general procedure for implementing a differential corrections algorithm using a method of free variables and constraints is presented. Examples of the implementation of this method are included for various targeting schemes. These targeting procedures are used to compute several types of periodic orbits near equilibrium solutions in the CR3BP. Methods for computing families of periodic orbits are also presented. The stability of the periodic orbits is investigated. Using stability information, some invariant manifold theory is summarized to offer context for equilibrium solutions and periodic solutions.

- Chapter 4: Using the numerical methods from Chapter 3, a technique for computing periodic horseshoe orbits is presented. Families of periodic horseshoe orbits are developed and analyzed for stability characteristics. The frequencies and resonances present in horseshoes are discussed. As a precursor to develop-

ing transfers to horseshoe orbits, invariant manifolds associated with unstable horseshoe orbits are computed.

- Chapter 5: Given a set of libration point trajectories and horseshoe orbits, the investigation into transfers between the two types of orbits is now possible. Transfers are computed in both the Saturn-Titan and Sun-Jupiter systems. As a preliminary analysis, an approximation of the classical two-body Hohmann transfer between a libration point orbit and a horseshoe orbit is computed. Next, three approaches are presented to determine transfers between libration point trajectories and horseshoe orbits. The first method is simply an instantaneous transfer between two intersecting orbits. The second scheme uses insight from invariant manifold theory. This technique employs an unstable manifold associated with a libration point orbit to reach a horseshoe orbit. The third procedure, which also incorporates invariant manifolds, employs Poincaré maps to search for very low-cost transfers. Both unstable manifolds originating from a libration point orbit and stable manifolds associated with a horseshoe orbit are used in conjunction with the map. A comparison in cost and time-of-flight is summarized.

- Chapter 6: In the final chapter, a summary of the investigation is presented along with concluding observations. Recommendations for further development are also offered.

With the structure of this investigation available, the necessary components are now explored in detail. The tools and models that are developed facilitate the computation of transfer trajectories from orbits near libration points to horseshoe orbits.

2. THE CIRCULAR RESTRICTED THREE-BODY PROBLEM

The analysis in this investigation is conducted within the context of the circular restricted three-body problem. As a framework, then, the general n-body problem is presented, along with the conditions for the reduction of the n-body problem to the circular restricted three-body problem. Subsequently, the scalar equations of motion are derived and the single available integral is noted. As a basis for understanding the motion, the equilibrium solutions are introduced, along with bounds on the trajectory evolution.

2.1 The *n*-Body Problem

The general n-body problem in celestial mechanics offers a model to obtain information about the motion of n bodies that are coupled by a mutual gravitational attraction. To illustrate such a scenario, let $\hat{X} - \hat{Y} - \hat{Z}$ be inertial unit vectors centered with origin at O in Figure 2.1. Then, $\bar{r}_i$ represents the vector from the origin to each body, P_i. (Note that carets represent a vector of unit length and overbars denote a general vector.)

The motion of each body, modeled as a particle, is assumed to be influenced only by the gravitational forces from each of the other particles. Let m_i be the mass of P_i, and denote the vector locating P_i with respect to P_j as $\bar{r}_{ji}$. The total force exerted on P_i, then, is expressed using Newton's law of gravitation,

$$\bar{F}_i = -G \sum_{\substack{j=1 \\ j \neq i}}^{n} \frac{m_i m_j}{r_{ji}^3} \bar{r}_{ji} \tag{2.1}$$

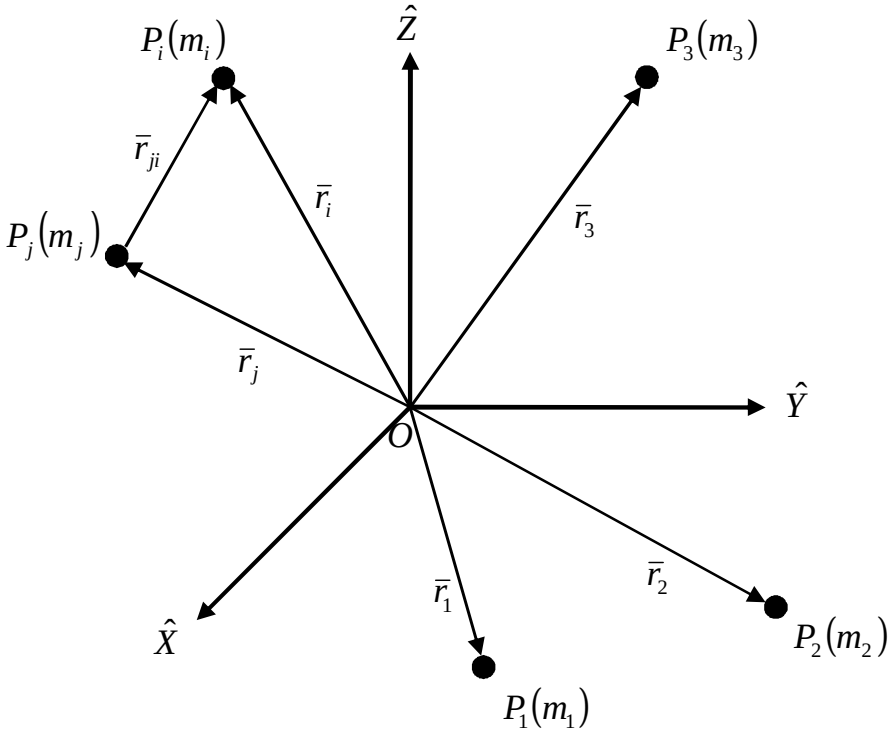

Figure 2.1. Sample n-Body System of Particles

where G is the universal gravitational constant. From this expression for the force exerted on each particle, Newton's second law of motion is employed to yield a vector equation of motion for each particle, that is

$$m_i \bar{r}_i'' = -G \sum_{\substack{j=1 \\ j \neq i}}^{n} \frac{m_i m_j}{r_{ji}^3} \bar{r}_{ji} \tag{2.2}$$

In this formulation, $\bar{r}_i''$ is the acceleration of P_i with respect to an inertial observer. Primes indicate derivatives with respect to dimensional time. To solve the complete set of scalar differential equations for n particles, $6n$ integrals of the motion are required. Currently, only ten constants are known, thus, the general n-body problem

cannot be solved in a closed analytical form. This lack of a solution to Eqn. (2.2) applies even for as few as two bodies since 12 constants are then required. If the general n-body problem is reformulated to describe relative motion, it is more manageable. When the problem is redefined for motion of P_i relative to P_q, the relative vector equation of motion is written

$$\bar{r}''_{qi} + \frac{G(m_i + m_q)}{r^3_{qi}}\bar{r}_{qi} = G\sum_{\substack{j=1 \\ j\neq i,q}}^{n} m_j \left(\frac{\bar{r}_{ij}}{r^3_{ji}} - \frac{\bar{r}_{qj}}{r^3_{qj}}\right) \tag{2.3}$$

where the right side of Eqn. (2.3) describes the effects of perturbing bodies. When $n = 2$, Eqn. (2.3) possesses no perturbing accelerations and appears as $\bar{r}''_{21} + \frac{G(m_1+m_2)}{r^3_{21}}\bar{r}_{21} = \bar{0}$. Therefore, when $n = 2$, a closed form analytical solution to the relative equation of motion exists, and these solutions are the familiar conic sections. For some applications, the insight gained from the conic solutions in the two-body problem serve as a solid basis for trajectory design.

2.2 The Circular Restricted Three-Body Problem

To build upon the insight gained from solutions in the two-body problems, yet incorporate some of the complexities of the n-body problem, add just one additional body. The focus is then the three-body problem. Denote the three bodies as P_1, P_2, and P_3, and let the masses be m_1, m_2, and m_3, respectively. When three bodies are considered, the inertially-based formulation in Eqn. (2.2) reduces to

$$\bar{r_3}'' = -G\frac{m_1}{r^3_{13}}\bar{r_{13}} - G\frac{m_2}{r^3_{23}}\bar{r_{23}} \tag{2.4}$$

which still requires 18 integrals of motion to solve for the motion of P_3 in closed-form. Thus, an analytical solution for Eqn. (2.4) is not available. Consider the relative formulation in Eqn. (2.3). When $n = 3$, Eqn. (2.3) reduces to

$$\bar{r}''_{13} + \frac{G\left(m_1 + m_3\right)}{r^3_{13}}\bar{r}_{13} = Gm_2\left(\frac{\bar{r}_{32}}{r^3_{32}} - \frac{\bar{r}_{12}}{r^3_{12}}\right) \tag{2.5}$$

that is, the vector differential equation that represents the motion of P_3 with respect to P_1. But, to solve for the motion of P_3 also requires the location of P_2. Thus, an additional differential equation is also required, that is,

$$\bar{r}''_{23} + \frac{G\left(m_2 + m_3\right)}{r_{23}^3}\bar{r}_{23} = Gm_1\left(\frac{\bar{r}_{31}}{r_{31}^3} - \frac{\bar{r}_{21}}{r_{12}^3}\right) \tag{2.6}$$

to determine the motion of P_3 with respect to P_2. Although the simultaneous solution of Eqns. (2.5)-(2.6) yields the motion of P_3 relative to the other bodies, a complete solution still requires 12 integrals of motion. With only 10 known constants, neither formulation produces a closed-form analytical solution for the motion of three bodies. Simplifying assumptions produce useful results. (Much of the subsequent development in the circular restricted three-body problem follows the analysis by Victor Szebehely in *Theory of Orbits: The Restricted Problem of Three Bodies* [1].)

2.2.1 Assumptions

To produce insight into the motion of three bodies, several assumptions are useful. First, assume that the mass of the third particle is infinitesimally small in comparison to the masses of the other two particles, and that the second body is less massive than the first, such that $m_3 << m_2 < m_1$. The two massive bodies are denoted primaries. Since the mass of P_3 is infinitesimally small compared to that of P_1 and P_2, the motion of the two primaries is not influenced by P_3 and can be modeled consistent with the relative two-body problem. Recall that this two-body formulation does possess a closed-form analytical solution.

A second reasonable assumption is that the two primaries move on circular orbits about their common center of mass. This center of mass, or barycenter, lies at a fixed position along the line connecting the two primaries. While the motion of P_1 and P_2 is planar, P_3 is free to move in all three dimensions. With this second assumption, the motion of P_3 is termed the solution to the Circular Restricted Three-Body Problem (CR3BP).

To model the CR3BP, it is useful to define a rotating coordinate frame R. First, let the inertial frame be defined by the unit vectors $\hat{X}$, $\hat{Y}$, $\hat{Z}$, as seen in Figure 2.1; this inertial frame is denoted frame I. Then, let unit vectors $\hat{x}, \hat{y}, \hat{z}$ define frame R, which rotates with respect to the inertial frame I, as illustrated in Figure 2.2. Frames R and I are both centered on the barycenter, labeled B, in Figure 2.2. Let P_1 and P_2 lie at fixed positions along the rotating $\hat{x}$-axis which is always directed from P_1 towards P_2. The $\hat{y}$-axis is perpendicular to the $\hat{x}$-axis in the plane of primary motion. The $\hat{z}$-axis coincides with the $\hat{Z}$-axis of the inertial frame, both of which are parallel to the orbital angular momentum vector associated with the primary orbits. The angle θ orients frame R with respect to frame I.

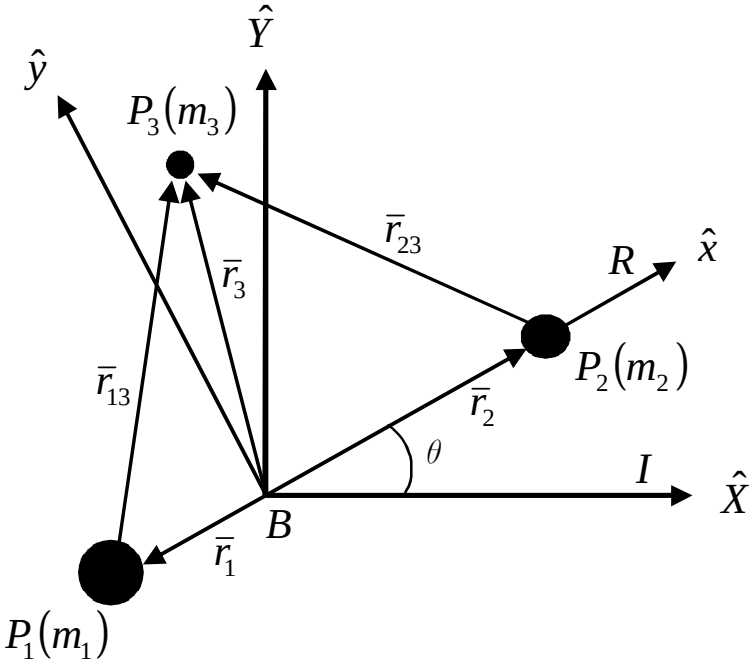

Figure 2.2. Appropriate Definitions in the Circular Three-Body Problem

2.2.2 Derivation of the Equations of Motion in the CR3BP

Prior to developing the equations of motion in the CR3BP, it is useful to define the characteristic quantities of length, mass, and time. Let the characteristic length be defined as

$$l^* = r_1 + r_2 \tag{2.7}$$

where r_i is the distance between a given primary and the barycenter. Since the primaries move in circular orbits, a constant distance from the barycenter is maintained and l^* is a constant value. The characteristic mass is similarly defined as

$$m^* = m_1 + m_2 \tag{2.8}$$

where m_1 is the mass of P_1 and the mass of P_2 is m_2. A third characteristic quantity, time, is evaluated as

$$t^* = \sqrt{\frac{(r_1 + r_2)^3}{G(m_1 + m_2)}} = \sqrt{\frac{l^{*3}}{Gm^*}} \tag{2.9}$$

where G is the universal gravitational constant. Note that this definition for characteristic time corresponds to the inverse of the mean motion of the primaries, or time per radian.

Before proceeding to the derivation of the equations of motion, some useful non-dimensional quantities are defined using the characteristic quantities. First, define a non-dimensional mass parameter as

$$\mu = \frac{m_2}{m^*} = \frac{1 - m_1}{m^*} \tag{2.10}$$

Then, non-dimensional time is denoted

$$\tau = \frac{t}{t^*} \tag{2.11}$$

and non-dimensional mean motion is equal to unity, that is,

$$n = \sqrt{\frac{Gm^*}{l^{*3}}} t^* = 1 \tag{2.12}$$

Note that the non-dimensional mean motion is equal to one in the CR3BP because the primaries are assumed to be moving on circular orbits, thus, the angular velocity is constant. The vectors in Figure 2.2 are also non-dimensionalized as follows

$$\bar{\rho} = \frac{\bar{r}_3}{l^*} \tag{2.13}$$

$$\bar{d} = \frac{\bar{r}_{13}}{l^*} \tag{2.14}$$

$$\bar{r} = \frac{\bar{r}_{23}}{l^*} \tag{2.15}$$

where $\bar{\rho}$ represents the location of P_3 with respect to the barycenter, $\bar{d}$ is the position of P_3 with respect to P_1, and $\bar{r}$ is the vector locating P_3 with respect to P_2.

Once the characteristic quantities and the corresponding non-dimensional scalars and vectors are defined, the non-dimensional equations of motion for the CR3BP can be derived. Recall that the body of interest is P_3, thus, an equation governing the motion of this body is formulated. The inertially-based equation governing the motion of P_3 in Eqn. (2.4) is rewritten in terms of the newly-defined non-dimensional quantities as

$$\ddot{\bar{\rho}} = -(1-\mu)\frac{\bar{d}}{d^3} - \mu\frac{\bar{r}}{r^3} \tag{2.16}$$

where the non-dimensional scalar magnitudes are defined as

$$d = \left|\bar{d}\right| = \sqrt{(x+\mu)^2 + y^2 + z^2} \tag{2.17}$$

and

$$r = |\bar{r}| = \sqrt{(x-1+\mu)^2 + y^2 + z^2} \tag{2.18}$$

Note that a dot indicates a derivative with respect to non-dimensional time. With the establishment of the force model for the motion of P_3 in Eqn. (2.16), it is now desirable to expand the left side of this equation into a more useful form. Recalling the rotating $\hat{x}, \hat{y}, \hat{z}$ frame R from Figure 2.2, the vector $\bar{\rho}$ can be split into vector components as

$$\bar{\rho} = x\hat{x} + y\hat{y} + z\hat{z} \tag{2.19}$$

Using kinematical relationships, the derivative of $\bar{\rho}$, which is expressed in terms of rotating coordinates, is evaluated with respect to an inertial observer. The resulting expression for $\ddot{\bar{\rho}}$ is substituted into the left side of Eqn. (2.16) yielding

$$\left(\ddot{x} - 2\dot{y}n - xn^2\right)\hat{x} + \left(\ddot{y} + 2\dot{x}n - yn^2\right)\hat{y} + \ddot{z}\hat{z} = -\left(1-\mu\right)\frac{\bar{d}}{\bar{d}^3} - \mu\frac{\bar{r}}{r^3} \tag{2.20}$$

Finally, Eqn. (2.20) is rewritten as three scalar, second-order, non-dimensional differential equations to describe the motion of P_3, that is

$$\ddot{x} - 2n\dot{y} - n^2x = -\frac{(1-\mu)(x+\mu)}{d^3} - \frac{\mu(x-1+\mu)}{r^3} \tag{2.21a}$$

$$\ddot{y} + 2n\dot{x} - n^2y = -\frac{(1-\mu)y}{d^3} - \frac{\mu y}{r^3} \tag{2.21b}$$

$$\ddot{z} = -\frac{(1-\mu)z}{d^3} - \frac{\mu z}{r^3} \tag{2.21c}$$

These equations are numerically integrated to solve for the motion of P_3, and supply the foundation for understanding the motion of bodies in the CR3BP.

2.2.3 Integral of Motion

To gain insight into the CR3BP, which has no general closed-form solution, it is reasonable to search for any integrals of the motion that might exist. First, reformulate Eqns. (2.21) in terms of a pseudo-potential function, i.e.

$$u^* = \frac{(1-\mu)}{d} + \frac{\mu}{r} + \frac{1}{2}n^2\left(x^2+y^2\right) \tag{2.22}$$

to produce a new form of the equations of motion

$$\ddot{x} - 2\dot{y} = \frac{\partial u^*}{\partial x} \tag{2.23a}$$

$$\ddot{y} + 2\dot{x} = \frac{\partial u^*}{\partial y} \tag{2.23b}$$

$$\ddot{z} = \frac{\partial u^*}{\partial z} \tag{2.23c}$$

This formulation is easily used to derive an energy-related integral. Consistent with derivations of energy-type constants, a dot product between the equations of motion

in potential form and the rotating velocity of P_3 produces scalar equations that are then summed. Since u^* includes only position terms, the right side of the resulting equation reduces to a total derivative, $\frac{du^*}{d\tau}$, as follows

$$\dot{x}\ddot{x} + \dot{y}\ddot{y} + \dot{z}\ddot{z} = \frac{du^*}{d\tau} \tag{2.24}$$

Equation (2.24) is then integrated, with the result

$$\frac{1}{2}\left(\dot{x}^2 + \dot{y}^2 + \dot{z}^2\right) = u^* - \frac{C_1}{2} \tag{2.25}$$

Rearranging, Eqn. (2.25) is written in the familiar form that defines the Jacobi integral,

$$v^2 = 2u^* - C \tag{2.26}$$

where v is the relative velocity of P_3, and C, denoted the Jacobi constant, is equal to $2C_1$. The Jacobi constant is the only known constant in the CR3BP and is very useful in analyzing orbits and trajectories. Since the Jacobi constant must remain constant at every point along the orbit unless the velocity of P_3 is changed by some external force, it is a convenient check of the accuracy of the numerical integration process.

2.3 Equilibrium Solutions in the CR3BP

Although the Jacobi constant offers useful insight, the equations of motion are still coupled, nonlinear, and complex. Another approach to provide more clarity is a search for equilibrium solutions. An equilibrium solution is determined given zero velocity and acceleration relative to the rotating CR3BP frame, or by solving

$$\frac{\partial u^*}{\partial x} = \frac{\partial u^*}{\partial y} = \frac{\partial u^*}{\partial z} = 0 \tag{2.27}$$

If P_3 is placed at one of these equilibrium locations, it maintains the same position with respect to the rotating frame for all time. The five equilibrium solutions were discovered by Lagrange in 1772, thus they are frequently labeled Lagrange points, and

also libration points [13]. The relative locations of the five Lagrange points, labeled L_1, L_2, L_3, L_4, and L_5, are plotted in Figure 2.3.

Points L_1, L_2, and L_3 are frequently denoted the collinear points since they lie on the $\hat{x}$-axis. Then, points L_4 and L_5 are identified as the equilateral points since they serve as the vertices of equilateral triangles along with the primaries. The locations for the collinear points are the zeros of a fifth-order equation and require iterations to solve numerically. The $\hat{x}$ coordinate that locates a Lagrange point L_i is written in terms of γ_i, defined as the distance from L_i to the nearest primary. The coordinates of the collinear points are then defined as

$$L_1 = (d_2 - \gamma_1)\,\hat{x} + 0\hat{y} + 0\hat{z} \tag{2.28a}$$

$$L_2 = (d_2 + \gamma_2)\,\hat{x} + 0\hat{y} + 0\hat{z} \tag{2.28b}$$

$$L_3 = -(d_1 + \gamma_3)\,\hat{x} + 0\hat{y} + 0\hat{z} \tag{2.28c}$$

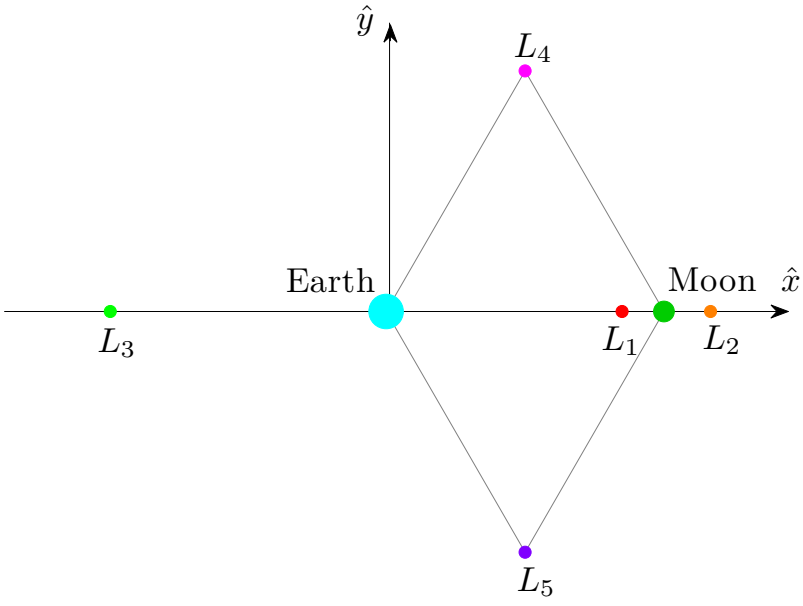

Figure 2.3. Lagrange Points in the Earth-Moon System

where d_1 is the non-dimensional distance between the barycenter and P_1, and d_2 is the non-dimensional distance between the barycenter and P_2. The nondimensional expression for each is given by

$$d_1 = \frac{|\bar{r_1}|}{l^*} \tag{2.29}$$

$$d_2 = \frac{|\bar{r_2}|}{l^*} \tag{2.30}$$

These coordinates are inserted in the expanded form of the partials in Eqn. (2.27), yielding three equations for γ_1, γ_2, and γ_3, that is

$$f_1(\gamma_1) = \frac{(\mu-1)}{(d_2-\gamma_1+\mu)^2} - \frac{\mu}{(d_2-\gamma_1-1+\mu)^2} + (d_2-\gamma_1) = 0 \tag{2.31a}$$

$$f_2(\gamma_2) = \frac{(\mu-1)}{(d_2+\gamma_2+\mu)^2} - \frac{\mu}{(d_2+\gamma_2-1+\mu)^2} + (d_2+\gamma_2) = 0 \tag{2.31b}$$

$$f_3(\gamma_3) = \frac{(\mu-1)}{(-d_1-\gamma_3+\mu)^2} - \frac{\mu}{(-d_1-\gamma_3-1+\mu)^2} + (-d_1-\gamma_3) = 0 \tag{2.31c}$$

An iterative scheme, such as Newton's method, is useful to solve for γ_1, γ_2, and γ_3. Given a nearby initial guess, the Newton method update equation

$$\gamma_i^{k+1} = \gamma_i^k - \frac{f_i\left(\gamma_i^k\right)}{f_i'\left(\gamma_i^k\right)} \tag{2.32}$$

is employed until $\left|\gamma_i^{k+1} - \gamma_i^k\right|$ is sufficiently small, producing the solution for γ_i, which in turn can be used to solve for the position of the collinear Lagrange points. In contrast to the iterative process that is required to determine the locations of the collinear Lagrange points, the position of the equilateral Lagrange points is available analytically to be

$$L_4 = \left(\frac{1}{2} - d_1\right)\hat{x} + \frac{\sqrt{3}}{2}\hat{y} \tag{2.33a}$$

$$L_5 = \left(\frac{1}{2} - d_1\right)\hat{x} - \frac{\sqrt{3}}{2}\hat{y} \tag{2.33b}$$

Once the locations of the Lagrange points have been established, the motion in the nearby vicinity can be further explored.

2.3.1 Linearization of the Equations of Motion Relative to the Equilibrium Solutions

The equilibrium points in the CR3BP are of interest for many exploration missions since, theoretically, a spacecraft located at an equilibrium point remains in such a relative position indefinitely. To further explore the applicability of the equilibrium points, stability information is useful. Approximations for motion in the vicinity of the equilibrium points are the basis for such an analysis. Thus, the EOMs are linearized relative to the equilibrium points. To derive the linear variational equations, recall the form of the EOMs for the CR3BP formulated in terms of the pseudo-potential function u^* in Eqns. (2.23a)-(2.23c). Perturbations are then introduced into the equilibrium solutions such that

$$x = x_{L_i} + \xi \tag{2.34a}$$

$$y = y_{L_i} + \eta \tag{2.34b}$$

$$z = z_{L_i} + \zeta \tag{2.34c}$$

Using a first-order Taylor series expansion for multiple variables and perturbations, the linear equations of motion for the variations ξ, η, and ζ are

$$\ddot{\xi} - 2\dot{\eta} = u^*_{xx}\xi + u^*_{xy}\eta + u^*_{xz}\zeta \tag{2.35a}$$

$$\ddot{\eta} + 2\dot{\xi} = u^*_{yx}\xi + u^*_{yy}\eta + u^*_{yz}\zeta \tag{2.35b}$$

$$\ddot{\zeta} = u^*_{zx}\xi + u^*_{zy}\eta + u^*_{zz}\zeta \tag{2.35c}$$

where u^*_{ij} denotes the second partial derivative $\frac{\partial^2 u^*}{\partial i \partial j}$ evaluated at the Lagrange point of interest. Consider these equations in state space form, where

$$\bar{x} = \begin{bmatrix} \xi & \eta & \zeta & \dot{\xi} & \dot{\eta} & \dot{\zeta} \end{bmatrix}^T \tag{2.36}$$

$$\dot{\bar{x}} = A\bar{x} \tag{2.37}$$

$$A = \begin{bmatrix} 0 & 0 & 0 & 1 & 0 & 0 \\ 0 & 0 & 0 & 0 & 1 & 0 \\ 0 & 0 & 0 & 0 & 0 & 1 \\ u^*_{xx} & u^*_{xy} & u^*_{xz} & 0 & 2 & 0 \\ u^*_{yx} & u^*_{yy} & u^*_{yz} & -2 & 0 & 0 \\ u^*_{zx} & u^*_{zy} & u^*_{zz} & 0 & 0 & 0 \end{bmatrix} \tag{2.38}$$

This system matrix A is useful in determining the stability of the Lagrange points; it is notable that the matrix A is constant. As discussed in Szebehely [1], the stability of the Lagrange points is determined using Lyapunov stability criteria. For a solution given a slight perturbation to be stable in the sense of Lyapunov, the subsequent path must remain bounded within a small region near the reference libration point throughout the system evolution in time [27]. For application to equilibrium point stability, this criteria states that an equilibrium solution, $\bar{x}_{eq}$, is stable if, for some small initial perturbation $\delta > 0$, there exists an $\epsilon > 0$ such that any solution $\bar{x}(t)$ satisfying

$$|\bar{x}(t_0) - \bar{x}_{eq}| < \delta \tag{2.39}$$

also satisfies

$$|\bar{x}(t) - \bar{x}_{eq}| < \epsilon \tag{2.40}$$

If this criteria is met, the solution is considered Lyapunov stable at least within the context of the linear variational equations. If the criteria are not satisfied, the particular solution is unstable. If $\bar{x}(t)$ approaches the equilibrium solution, $\bar{x}_{eq}$, as time approaches infinity, then the equilibrium solution is termed asymptotically stable. In practice, the stability of the equilibrium solutions is determined from the characteristic equation, $|\lambda I - A| = 0$, and the six corresponding eigenvalues, λ_i, where $i = 1, 2 \ldots, 5, 6$. The eigenvalues of a characteristic equation are complex in general, and stability properties can be deduced by inspecting the real component of the eigenvalues. Based on Lyapunov stability criteria, if *any* real component is positive, the point is unstable [1]. If *all* real components are negative, the point is asymptotically stable. If the real component is equal to zero for some eigenvalues, and

negative for all remaining eigenvalues, the point is marginally stable in a linear sense, however, the stability in the nonlinear system cannot be determined from this analysis alone. An eigenvalue analysis based solely on this approach reveals that in the Earth-Moon system, the collinear Lagrange points are unstable, while the equilateral Lagrange points are marginally stable for L_4 and L_5, evaluated in terms of first-order variational equations. Behavior near the Lagrange points can be further analyzed by considering first the motion near the collinear Lagrange points, and then the motion near the equilateral Lagrange points.

2.3.2 Linear Motion Near the Collinear Lagrange Points

Although linear, it is still insightful to explore the variational behavior. Notice that all Lagrange points are located in the $\hat{x}$-$\hat{y}$ plane. Since the partials u^*_{xz}, u^*_{yz}, u^*_{zx}, and u^*_{zy} are all evaluated at L_i and, thus, equal zero, the Eqns. (2.35a)-(2.35c) reduce to

$$\ddot{\xi} - 2\dot{\eta} = u^*_{xx}\xi + u^*_{xy}\eta \tag{2.41a}$$

$$\ddot{\eta} + 2\dot{\xi} = u^*_{yx}\xi + u^*_{yy}\eta \tag{2.41b}$$

$$\ddot{\zeta} = u^*_{zz}\zeta \tag{2.41c}$$

If only in-plane motion near the Lagrange points is considered, then Eqns. (2.41a)-(2.41b) are utilized, and the characteristic equation becomes

$$\lambda^4 + \left(4 - u^*_{xx} - u^*_{yy}\right)\lambda^2 + \left(2u^*_{xy} - 2u^*_{yx}\right)\lambda + \left(u^*_{xx}u^*_{yy} - u^*_{yx}u^*_{xy}\right) = 0 \tag{2.42}$$

The collinear Lagrange points are located on the $\hat{x}$-axis, so $y_{L_i} = z_{L_i} = 0$ and, therefore, $u^*_{xy} = 0$. The characteristic equation in Eqn. (2.42) becomes

$$\lambda^4 + \left(4 - u^*_{xx} - u^*_{yy}\right)\lambda^2 + u^*_{xx}u^*_{yy} = 0 \tag{2.43}$$

For this characteristic equation, the real eigenvalues, $\lambda_{1,2}$, and imaginary eigenvalues, $\lambda_{3,4}$ are then

$$\lambda_{1,2} = \pm\sqrt{-\beta_1 + \sqrt{\beta_1^2 + \beta_2^2}} \tag{2.44a}$$

$$\lambda_{3,4} = \pm\sqrt{-\beta_1 - \sqrt{\beta_1^2 + \beta_2^2}} \tag{2.44b}$$

where

$$\beta_1 = 2 - \frac{u^*_{xx} + u^*_{yy}}{2} \tag{2.45}$$

$$\beta_2^2 = -u^*_{xx} u^*_{yy} \tag{2.46}$$

If the initial conditions are carefully selected such that divergent motion is suppressed, and only the imaginary eigenvalues are excited, the resulting solutions for the variations are written in the form [1]

$$\xi = \xi_0 \cos s\,(t - t_0) + \frac{\eta_0}{\beta_3} \sin s\,(t - t_0) \tag{2.47a}$$

$$\eta = \eta_0 \cos s\,(t - t_0) - \beta_3 \eta_0 \sin s\,(t - t_0)) \tag{2.47b}$$

where s and β_3 are

$$s = \sqrt{\beta_1 + \sqrt{\beta_1^2 + \beta_2^2}} \tag{2.48}$$

$$\beta_3 = \frac{s^2 + u^*_{xx}}{2s} \tag{2.49}$$

The analytical solution plotted in Figure 2.4 is an example of the linear, bounded motion about L_1, and is computed with $\xi_0 = 10$ km and $\eta_0 = 0$ km. Alternatively, if initial conditions are selected to eliminate the bounded motion, and only excite the real roots, the equations describing the variations are expressed as [1]

$$\xi = \xi_0 \cosh \lambda_1\,(t - t_0) + \frac{\eta_0}{\alpha_1} \sinh \lambda_1\,(t - t_0) \tag{2.50a}$$

$$\eta = \eta_0 \cosh \lambda_1\,(t - t_0) + \xi_0 \alpha_1 \sinh \lambda_1\,(t - t_0)) \tag{2.50b}$$

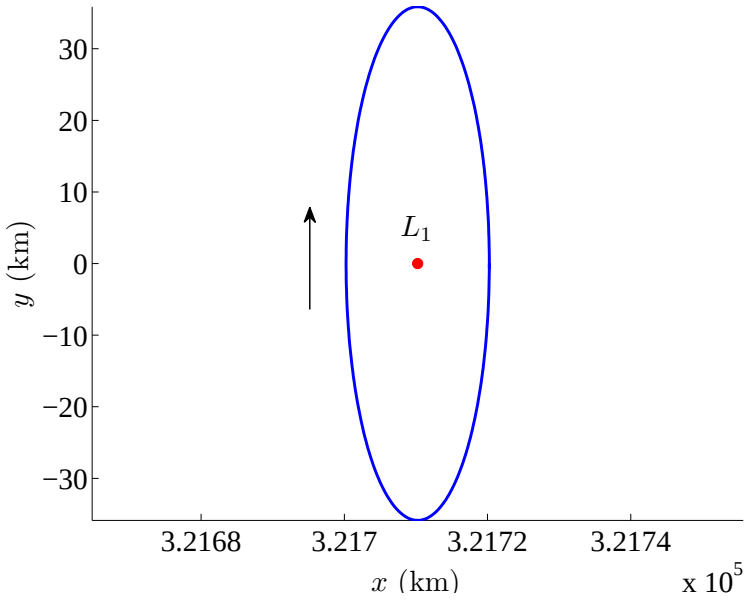

Figure 2.4. Linearized Motion About L_1 in the Earth-Moon System

where α_1 is defined as

$$\alpha_1 = \frac{\lambda_1^2 - u_{xx}^*}{2\lambda_1} \tag{2.51}$$

The flow field plotted in Figure 2.5 is an example of this completely unbounded motion. Consistent with the solution in Eqn. (2.50), the flow around L_1, pictured in magenta, approaches and departs the vicinity of the Lagrange point on hyperbolas. The blue line crossing through L_1 represents the unstable eigenvector direction associated with the L_1 point, while the green line represents the stable eigenvector.

2.3.3 Linear Behavior near the Equilateral Lagrange Points

Linear motion relative to the equilateral Lagrange points is also of interest. Consider in-plane motion about L_4 or L_5. For these Lagrange points, Eqn. (2.42) becomes

$$\lambda^4 + \left(4 - u_{xx}^* - u_{yy}^*\right)\lambda^2 + \left(u_{xx}^* u_{yy}^* - {u_{xy}^*}^2\right) = 0 \tag{2.52}$$

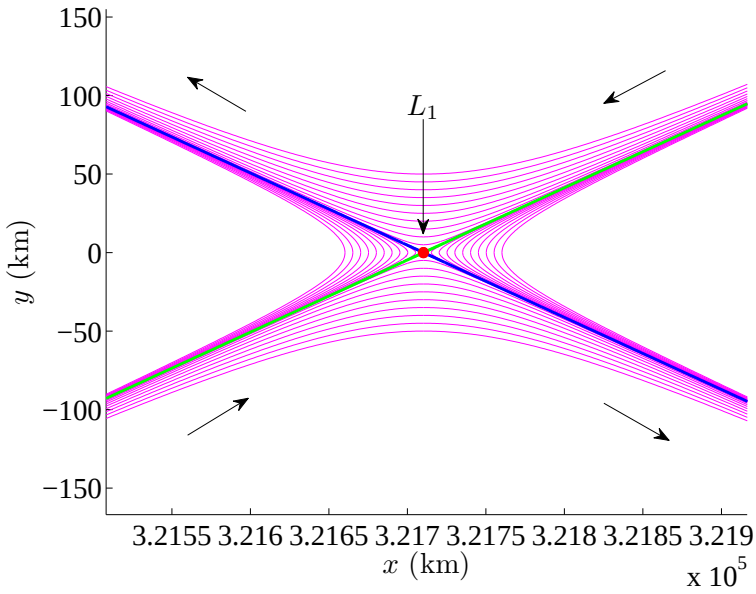

Figure 2.5. Flow Field Around L_1 in the Earth-Moon System

Evaluating Eqn. (2.52) precisely at the L_4 and L_5 locations represented in terms of their $\hat{x}$, $\hat{y}$ coordinates yields a reduced characteristic equation, that is,

$$\lambda^4 + \lambda^2 + \frac{27}{4}\mu\left(1-\mu\right) = 0 \tag{2.53}$$

The roots of this equation yield the in-plane eigenvalues associated with the equilateral points as

$$\lambda_{1,2} = \pm\sqrt{\frac{-1+\sqrt{1-27\mu\left(1-\mu\right)}}{2}} \tag{2.54a}$$

$$\lambda_{1,2} = \pm\sqrt{\frac{-1-\sqrt{1-27\mu\left(1-\mu\right)}}{2}} \tag{2.54b}$$

where λ_i is clearly a function of μ. A linear analysis of the eigenvalues as a function of μ reveals that motion near the equilateral points is marginally stable over the following range: $0 \leq \mu \leq 0.03852$. Most restricted three-body systems of interest in the solar system possess a μ value within this range and, therefore, exhibit marginally stable behavior in the linear sense in the vicinity of L_4 and L_5. Szebehely [1] provides a

thorough investigation of the stable solutions of the linear equation. First, to simplify notation, let $\lambda_{1,2} = \pm s_1 i$ and $\lambda_{3,4} = \pm s_2 i$. The frequencies s_1 and s_2 are defined such that $s_1 < s_2$. Since the period associated with this linear motion is defined as $2\pi/s$, the linear motion near L_4 and L_5 is clearly a composite of both short- and long-period terms. The short-period terms are those involving s_2, and the long-period terms incorporate s_1. The variational equations of motion for ξ and η yield solutions that decompose the solution into the short- and long-period responses. When isolating the short-period motion near the equilateral points, the resulting equations of motion are written

$$\xi = \xi_0 \cos s_2 t + \frac{\dot{\xi}_0}{s_2} \sin s_2 t \tag{2.55a}$$

$$\eta = \eta_0 \cos s_2 t + \frac{\dot{\eta}_0}{s_2} \sin s_2 t \tag{2.55b}$$

Conversely, the long-period motion is also available, resulting in the following equations of motion for the long-period variations

$$\xi = \xi_0 \cos s_1 t + \frac{\dot{\xi}_0}{s_1} \sin s_1 t \tag{2.56a}$$

$$\eta = \eta_0 \cos s_1 t + \frac{\dot{\eta}_0}{s_1} \sin s_1 t \tag{2.56b}$$

To illustrate the analytical solutions for short- and long-period behavior near the equilateral Lagrange points, refer to Figure 2.6. Note that the corresponding solutions near L_5 are apparent by mirroring the solutions for L_4 across the $\hat{x}$-axis.

2.4 Zero Velocity Surfaces

Another important tool in understanding the motion of P_3 in the CR3BP is the boundary of the motion, that is, the zero velocity surfaces. Recall from Eqn. (2.26) the definition of the Jacobi constant, C. If the relative velocity is zero, the Jacobi constant is evaluated as

$$C = x^2 + y^2 + \frac{2\,(1-\mu)}{d} + \frac{2\mu}{r} \tag{2.57}$$

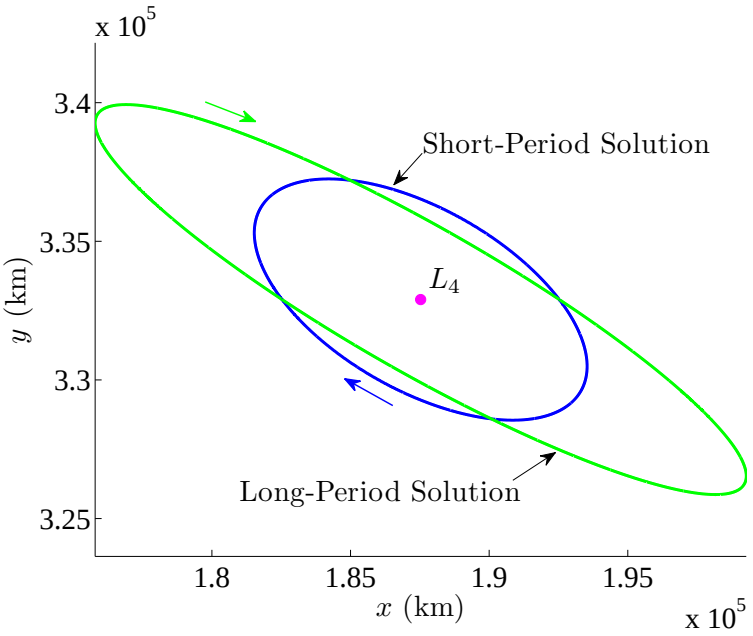

Figure 2.6. Analytical Approximations of Short- and Long-Period Motion Near L_4

From this relationship, it is clear that, for a particular value of C, there are an infinite number of locations that satisfy the condition of zero velocity. This collection of position coordinates comprises a zero velocity surface, essentially a barrier that bounds the excursions of P_3 in its orbit given a particular value of C. Thus, a zero velocity surface (ZVS), or zero velocity curve (ZVC) when considering motion restricted within a plane, bounds the motion of a particular orbit.

Several examples of ZVCs in the Earth-Moon system are plotted in Figure 2.7. In each of the figures, the curves represent the locations corresponding to zero relative velocity, while the space shaded in blue is physically unreachable for P_3. The progression of the ZVCs with changing values of the Jacobi constant in Figure 2.7 reveals an important concept. Note that the ZVCs actually reflect the intersection of the ZVS with the $\hat{x}$-$\hat{y}$ plane. As C decreases, which is analogous to an increase in energy, the ZVCs tend to "open up", increasing the range of space which is accessible. Additionally, for a value of Jacobi constant equal to that of any given Lagrange point, the ZVCs intersect the specified location. Thus, for L_1 and L_2, the corresponding value

of Jacobi constant marks the value of C at which the gateway opens. To illustrate, note Figure 2.7(a), where the ZVC intersects L_1. Decreasing the value of Jacobi constant to correspond to L_2 in Figure 2.7(b), the L_1 gateway is now open, and the ZVC intersects L_2. This trend continues as the Jacobi constant further decreases, until the ZVCs reach L_4 and L_5. At this value of Jacobi constant, the ZVS contracts to L_4 and L_5, and leave the $\hat{x}$-$\hat{y}$ plane. In this process, the ZVCs appear to collapse to L_4 and L_5 and disappear. In Figure 2.7, the $\hat{z}$ components associated with the ZVS are not apparent but do exist. A selected three-dimensional ZVS in the the Earth-Moon system appears in Figure 2.8. At the value of Jacobi constant corresponding to the surface in Figure 2.8, the L_1 gateway is open. Thus, the trajectory remains within the boundaries of the two connected bubbles surrounding each primary, or beyond the cylindrical surface. The inaccessible space between the cylindrical boundary and the bubble is termed the "forbidden region".

2.5 Transformation Between Rotating and Inertial Coordinate Frames

Trajectories in the CR3BP are typically viewed from the perspective of a rotating coordinate frame, which often reveals structure that is not apparent in the inertial frame. However, regardless of the formulation for computation, it is frequently useful to transform the trajectories for viewing in the inertial frame. Transformation of the entire state from inertial to rotating coordinates and vice versa is also useful for design and optimization. To illustrate the visual differences in the appearance of a trajectory as plotted in the inertial and rotating frames, consider Figure 2.9. In each plot, the initial position is denoted by a small black dot. Both the rotating and inertial views of the orbit are valuable. The evolution of the trajectory in time, relative to the Moon, is much clearer in the rotating view in Figure 2.9(a). The inertial view of the orbit in Figure 2.9(b) yields different insights. In the inertial view, it is difficult to visualize the distinction of each revolution along the orbit, and the impact of the Moon is also unclear since the Moon is constantly in motion about the Earth. However, the inertial

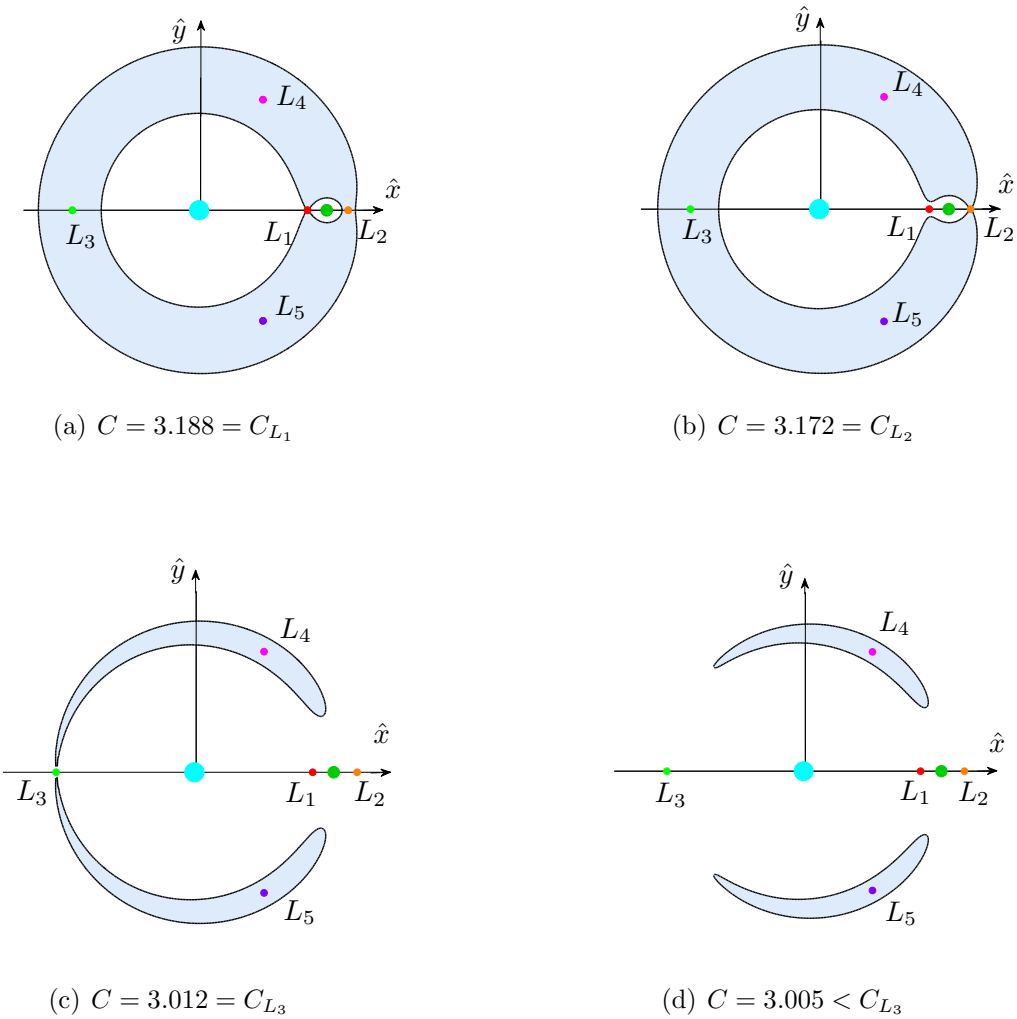

(a) $C = 3.188 = C_{L_1}$

(b) $C = 3.172 = C_{L_2}$

(c) $C = 3.012 = C_{L_3}$

(d) $C = 3.005 < C_{L_3}$

Figure 2.7. Zero Velocity Curves in the Earth-Moon System

view clearly offers more immediate interpretation in terms of the overall shape of the orbit. This inertial clarity is important for many applications, including transfers.

To derive a transformation from the inertial frame I to the rotating frame R, consider the relationship between the frames in Figure 2.10. By inspection, the transformation matrix, ${}^{I}C^{R}$, from the inertial unit vectors to rotating coordinates is apparent, that is, the direction cosine matrix is written

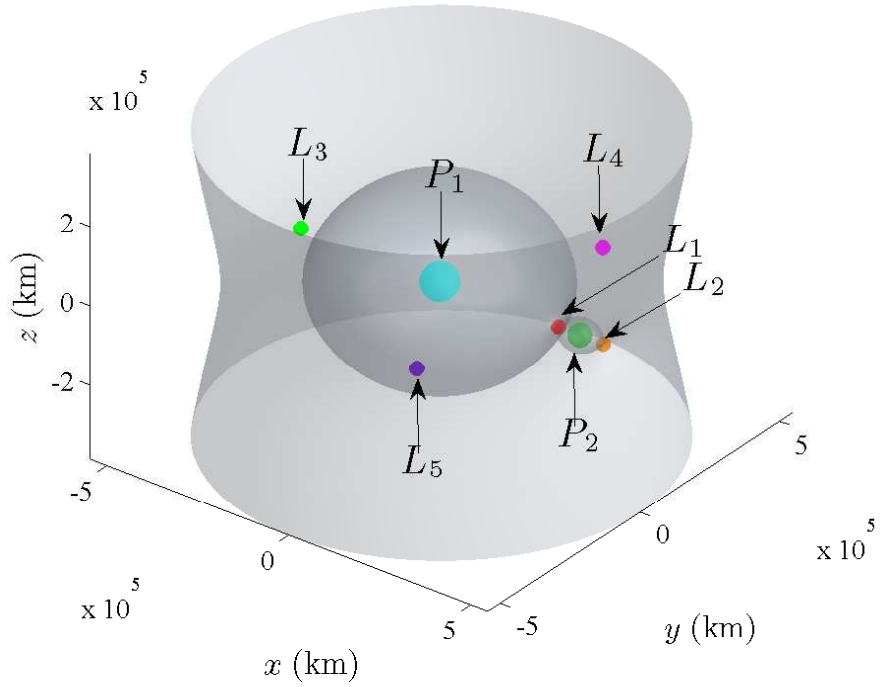

Figure 2.8. The three-dimensional ZVS for $C = C_{L_2}$ in the Earth-Moon System

$$ {}^{I}C^{R} = \begin{bmatrix} cos\,(\tau) & sin\,(\tau) & 0 \\ -sin\,(\tau) & cos\,(\tau) & 0 \\ 0 & 0 & 1 \end{bmatrix} \tag{2.58} $$

where ${}^{I}C^{R}$ relates the components expressed in terms of I and R by

$$ \begin{bmatrix} r_x \\ r_y \\ r_z \end{bmatrix} = {}^{I}C^{R} \begin{bmatrix} r_X \\ r_Y \\ r_Z \end{bmatrix} \tag{2.59} $$

Transforming the inertial velocity into the corresponding relative velocity requires additional consideration. Recall that the relative and inertial velocities are related by the kinematic equation

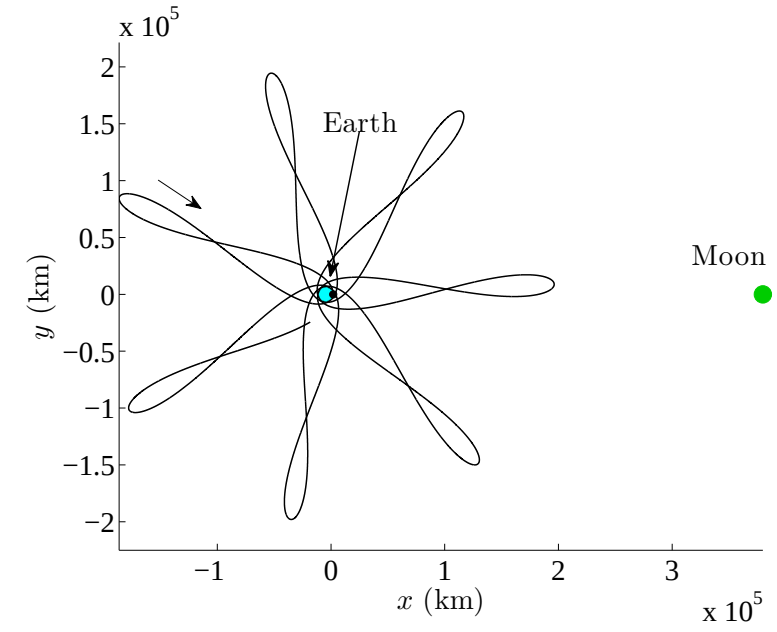

(a) Rotating View

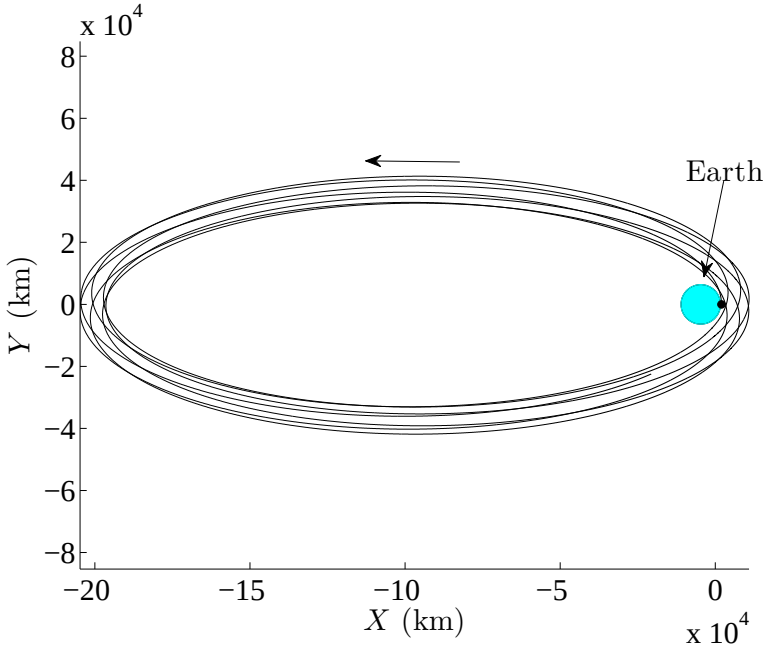

(b) Inertial View

Figure 2.9. Rotating and Inertial View of an Orbit in the Earth-Moon System

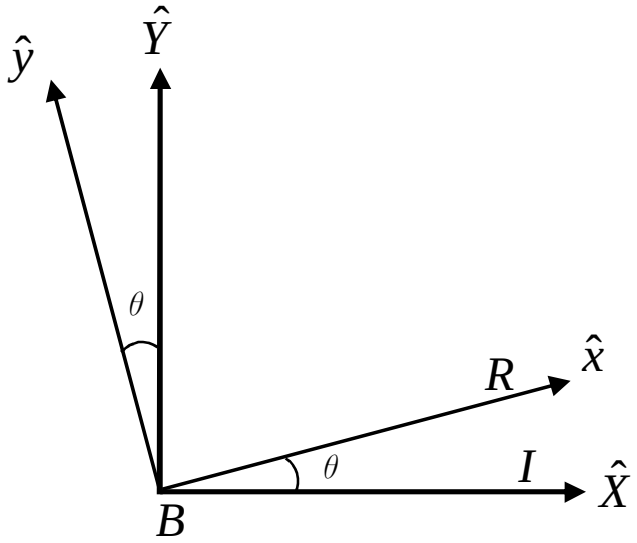

Figure 2.10. Inertial and Rotating Coordinate Frames

$$\frac{^{I}d\bar{q}}{dt} = \frac{^{R}d\bar{q}}{dt} + ^{I}\bar{\omega}^{R} \times \bar{q} \tag{2.60}$$

where the angular velocity of frame R relative to I is $^{I}\bar{\omega}^{R} = \dot{\theta}\hat{z}$, and $\bar{q}$ is any position vector expressed in terms of unit vectors fixed in frame R. Thus, transforming both position and velocity states is accomplished using the complete transformation matrix, i.e.

$$\begin{bmatrix} r_x \\ r_y \\ r_z \\ v_x \\ v_y \\ v_z \end{bmatrix} = \begin{bmatrix} ^{I}C^{R} & 0_{3\times3} \\ ^{I}\dot{C}^{R} & ^{I}C^{R} \end{bmatrix} \begin{bmatrix} r_X \\ r_Y \\ r_Z \\ v_X \\ v_Y \\ v_Z \end{bmatrix} \tag{2.61}$$

which produces the full inertial state given the position and velocity relative to a rotating observer and expressed in terms of rotating unit vectors. The coordinate system can also be transformed in the opposite direction. If the matrix in Eqn. (2.61) is simply inverted,

$$\begin{bmatrix} r_X \\ r_Y \\ r_Z \\ v_X \\ v_Y \\ v_Z \end{bmatrix} = \begin{bmatrix} {}^{I}C^{R} & 0_{3\times 3} \\ {}^{I}\dot{C}^{R} & {}^{I}C^{R} \end{bmatrix}^{-1} \begin{bmatrix} r_x \\ r_y \\ r_z \\ v_x \\ v_y \\ v_z \end{bmatrix} \tag{2.62}$$

Then, a full relative state expressed in terms of rotating unit vectors is easily transformed to a full inertial state.

3. NUMERICAL METHODS FOR ORBIT COMPUTATION

The basic equations of motion and the fundamental properties of the CR3BP are now established. Therefore, the next natural step is to develop numerical schemes to determine particular orbits and transfers. Several types of orbits in the CR3BP are introduced, and numerical techniques to produce the orbits are detailed. One of the most important tools, both in computing periodic orbits and in targeting particular trajectories, is the state transition matrix.

3.1 The State Transition Matrix

The State Transition Matrix (STM) and the relationships between the variations with respect to a reference solution at different times is a fundamental concept in many disciplines, including control theory. As a sensitivity matrix, the STM offers a linear estimate of some final state at time t as the result of perturbations introduced into the initial state at time t_0. The information supplied by the STM is, therefore, useful in modifying trajectories to meet a set of desired characteristics, that is, targeting.

The STM provides a linear estimate of a state and, as such, is derived from linear equations of motion. In Section 2.3.1, the EOMs are linearized with respect to the equilibrium solutions. For targeting applications, a similar process is employed to linearize the EOMs with respect to a more general reference trajectory, denoted $\bar{x}_r(t)$. If a variation $\delta\bar{x}(t)$ is introduced to a reference state, such that $\bar{x}(t) = \bar{x}_r(t) + \delta\bar{x}(t)$, a first-order Taylor series expansion is evaluated, resulting in the following differential equation in matrix form

$$\delta\dot{\bar{x}}(t) = A(t)\,\delta\bar{x}(t) \tag{3.1}$$

where $A(t)$ is

$$A(t) = \begin{bmatrix} 0 & 0 & 0 & 1 & 0 & 0 \\ 0 & 0 & 0 & 0 & 1 & 0 \\ 0 & 0 & 0 & 0 & 0 & 1 \\ u^*_{xx} & u^*_{xy} & u^*_{xz} & 0 & 2 & 0 \\ u^*_{yx} & u^*_{yy} & u^*_{yz} & -2 & 0 & 0 \\ u^*_{zx} & u^*_{zy} & u^*_{zz} & 0 & 0 & 0 \end{bmatrix} \tag{3.2}$$

and u^*_{ij} denotes the second partial derivative $\frac{\partial^2 u^*}{\partial i \partial j}$ evaluated along the reference trajectory at time t. The solution to the differential equation in Eqn. (3.1) is

$$\delta\bar{x}(t) = \Phi(t, t_0)\,\delta\bar{x}_0 \tag{3.3}$$

where $\delta\bar{x}_0$ is the variation at time $t = t_0$, $\delta\bar{x}(t)$ is the variation at another time t, and $\Phi(t, t_0)$ is the matrix of partials denoted as the STM [28]. In the CR3BP, the STM is therefore defined as the 6×6 matrix

$$\Phi(t, t_0) = \begin{bmatrix} \frac{\partial x}{\partial x_0} & \frac{\partial x}{\partial y_0} & \frac{\partial x}{\partial z_0} & \frac{\partial x}{\partial \dot{x}_0} & \frac{\partial x}{\partial \dot{y}_0} & \frac{\partial x}{\partial \dot{z}_0} \\ \frac{\partial y}{\partial x_0} & \frac{\partial y}{\partial y_0} & \frac{\partial y}{\partial z_0} & \frac{\partial y}{\partial \dot{x}_0} & \frac{\partial y}{\partial \dot{y}_0} & \frac{\partial y}{\partial \dot{z}_0} \\ \frac{\partial z}{\partial x_0} & \frac{\partial z}{\partial y_0} & \frac{\partial z}{\partial z_0} & \frac{\partial z}{\partial \dot{x}_0} & \frac{\partial z}{\partial \dot{y}_0} & \frac{\partial z}{\partial \dot{z}_0} \\ \frac{\partial \dot{x}}{\partial x_0} & \frac{\partial \dot{x}}{\partial y_0} & \frac{\partial \dot{x}}{\partial z_0} & \frac{\partial \dot{x}}{\partial \dot{x}_0} & \frac{\partial \dot{x}}{\partial \dot{y}_0} & \frac{\partial \dot{x}}{\partial \dot{z}_0} \\ \frac{\partial \dot{y}}{\partial x_0} & \frac{\partial \dot{y}}{\partial y_0} & \frac{\partial \dot{y}}{\partial z_0} & \frac{\partial \dot{y}}{\partial \dot{x}_0} & \frac{\partial \dot{y}}{\partial \dot{y}_0} & \frac{\partial \dot{y}}{\partial \dot{z}_0} \\ \frac{\partial \dot{z}}{\partial x_0} & \frac{\partial \dot{z}}{\partial y_0} & \frac{\partial \dot{z}}{\partial z_0} & \frac{\partial \dot{z}}{\partial \dot{x}_0} & \frac{\partial \dot{z}}{\partial \dot{y}_0} & \frac{\partial \dot{z}}{\partial \dot{z}_0} \end{bmatrix} \tag{3.4}$$

From Eqn. (3.3), at $t = t_0$, $\Phi(t, t_0)$ must equal the identity matrix, and therefore satisfies the following initial condition

$$\Phi(t_0, t_0) = I \tag{3.5}$$

Substituting Eqn. (3.3) into Eqn. (3.1) yields the matrix differential equation

$$\dot{\Phi}(t, t_0) = A(t)\,\Phi(t, t_0) \tag{3.6}$$

For targeting purposes in the CR3BP, the STM can be evaluated at every point along a simulated trajectory. To that end, let $\Phi(t, t_0) = I$ initially, and then numerically integrate Eqn. (3.6) to obtain $\Phi(t, t_0)$ at every time step along the path, where $A(t)$ is calculated from Eqn. (3.2).

3.2 A General Method for Implementation of a Differential Corrections Process

A wide variety of tasks in trajectory design and analysis require the use of corrections schemes. Fundamentally, differential corrections is based on targeting. But, as the problems and goals become increasingly complex, more sophisticated algorithms are employed to implement any differential corrections methodology. Since the STM supplies a linear estimate of a state at a future time, it is a powerful tool in implementing such schemes. In general, a baseline, or reference, trajectory that may not satisfy all the desired criteria is computed. Then, some differential corrections algorithm involving the STM is iteratively applied to the reference trajectory until it is corrected to meet the desired criteria.

Although there are many ways to implement this simple targeting concept, the implementation of the various targeting schemes described in this investigation use one specific approach. This method of free variables and constraints has been successfully utilized by many researchers in various disciplines and is simple to implement [27], [29], [30]. The first step in formulating this algorithm is constructing a design vector, $\bar{X}$,

$$\bar{X} = \begin{bmatrix} X_1 \\ X_2 \\ \vdots \\ X_n \end{bmatrix} \tag{3.7}$$

in which the elements are defined as the variables that are free to change, or can be adjusted, in the problem. The vector $\bar{X}$ may include position and/or velocity states, time, or other variables as needed. Then, a vector of constraints, $\bar{F}\left(\bar{X}\right)$,

$$\bar{F}\left(\bar{X}\right) = \begin{bmatrix} \bar{F}_1\left(\bar{X}\right) \\ \bar{F}_2\left(\bar{X}\right) \\ \vdots \\ \bar{F}_m\left(\bar{X}\right) \end{bmatrix} = \bar{0} \tag{3.8}$$

is constructed. The goal of the targeting scheme is the correction of the design vector until all the constraints are satisfied such that $\bar{F}\left(\bar{X}\right) = \bar{0}$. To develop the algorithm to correct the design variables such that the constraint relationships are satisfied, a first-order Taylor series expansion of $\bar{F}\left(\bar{X}\right)$ is employed. Given an initial guess for the design vector, $\bar{X}_0$, then

$$\bar{F}\left(\bar{X}\right) = \bar{F}\left(\bar{X}_0\right) + D\bar{F}\left(\bar{X}_0\right)\left(\bar{X} - \bar{X}_0\right) \tag{3.9}$$

where $D\bar{F}\left(\bar{X}_0\right)$ is an $m \times n$ matrix of first-order partials. The elements of this Jacobian matrix are derived as follows

$$D\bar{F}\left(\bar{X}_0\right) = \frac{\partial \bar{F}\left(\bar{X}_0\right)}{\partial \bar{X}_0} = \begin{bmatrix} \frac{\partial F_1}{\partial X_1} & \cdots & \frac{\partial F_1}{\partial X_n} \\ \vdots & \ddots & \vdots \\ \frac{\partial F_m}{\partial X_1} & \cdots & \frac{\partial F_m}{\partial X_n} \end{bmatrix} \tag{3.10}$$

Combining Eqns. (3.8) and (3.9) and formulating in terms of a recursive relationship, Eqn. (3.9) becomes

$$\bar{F}\left(\bar{X}^j\right) + D\bar{F}\left(\bar{X}^j\right)\left(\bar{X}^{j+1} - \bar{X}^j\right) = \bar{0} \tag{3.11}$$

which is iteratively solved for $\bar{X}^{j+1}$ until a design vector is determined such that $\bar{F}\left(\bar{X}\right) = \bar{0}$. Of course, this condition, as expressed in Eqn. (3.8), is the simplest form of some convergence criteria. It can be modified, for example, to employ some weighting scheme. However, the basic form is used in this analysis. The procedure to solve Eqn. (3.11) depends on the number of design variables, n, and the number of constraints, m. If $n = m$, then Eqn. (3.11) can be directly solved for $\bar{X}^{j+1}$ such that

$$\bar{X}^{j+1} = \bar{X}^j - D\bar{F}\left(\bar{X}^j\right)^{-1}\bar{F}\left(\bar{X}^j\right) \tag{3.12}$$

If, however, $n > m$, there are infinite solutions to Eqn. (3.11). The approach to solve the problem selected in this investigation is the minimum norm solution,

$$\bar{X}^{j+1} = \bar{X}^j - D\bar{F}\left(\bar{X}^j\right)^T\left[D\bar{F}\left(\bar{X}^j\right)D\bar{F}\left(\bar{X}^j\right)^T\right]^{-1}\bar{F}\left(\bar{X}^j\right) \tag{3.13}$$

Since this is a numerical process, iterations continue until $\left\|\bar{F}\left(\bar{X}\right)\right\| < \epsilon$, where ϵ is sufficiently small.

3.3 Single Shooting

The usefulness of the STM for any type of targeting scheme in the CR3BP is well illustrated by the single shooting method. "Single shooting" implies correcting a single transfer arc to reach a pre-specified target. In general, this method requires a start-up arc, that is, a reference trajectory arc, then uses the STM to iteratively correct the initial velocity on the reference arc until it meets the desired end conditions. A more explicit description of the implementation of this process is detailed for two examples involving (a) a single shooting fixed-time position targeting method and (b) a variable-time position targeting algorithm.

3.3.1 Fixed-Time Position Targeting

One form of "single shooting" is the simple fixed-time position targeting scheme. Let there be a fixed target position, $\bar{r}_d$, that is specified a priori. For a given reference trajectory, such as the red reference arc in Figure 3.1, let the initial state be denoted $\bar{x}_0$. Then, after numerical integration of the nonlinear differential equations for a predetermined time T, the final state is denoted $\bar{x}^t$, where $\bar{x}^t$ is equivalent to $\bar{x}\left(\bar{x}_0, T\right)$. Thus, $\bar{x}^t$ is the resulting state from propagation of the initial state $\bar{x}_0$ for time T. Velocity at target arrival is unconstrained, and the time T along the final trajectory is fixed to be the same as the time T along the reference trajectory. Since the initial position is fixed, this problem is equivalent to determining the necessary adjustment of the velocity states, i.e., the Δv maneuver, that is required to reach some target position vector.

The solution to the position targeting problem is approached in a systematic and iterative manner. First, consider which variables are free to be adjusted. For this

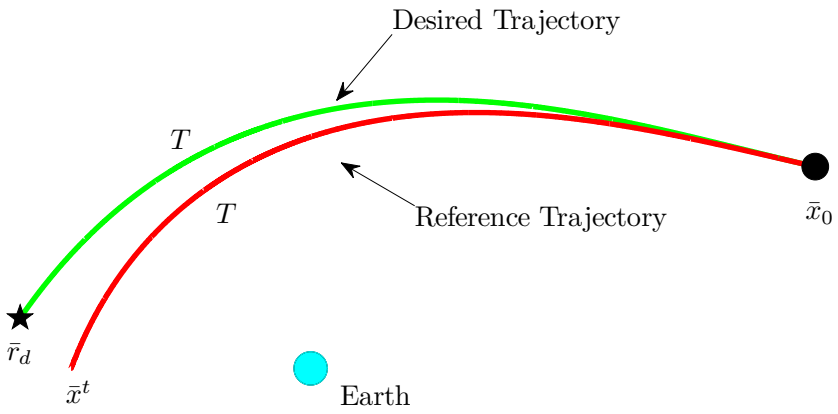

Figure 3.1. Fixed-Time Position Targeting Scheme

problem, only the initial velocities are variable, therefore the initial velocities are included in the design vector, $\bar{X}$ such that

$$\bar{X} = \begin{bmatrix} \dot{x_0} \\ \dot{y_0} \\ \dot{z_0} \end{bmatrix} \tag{3.14}$$

Next, consider the constraints. Only the final position is constrained to equal the target position, $\bar{r_d} = \begin{bmatrix} x_d & y_d & z_d \end{bmatrix}^T$, therefore the constraint vector, $\bar{F}\left(\bar{X}\right)$ is defined

$$\bar{F}\left(\bar{X}\right) = \begin{bmatrix} x^t - x_d \\ y^t - y_d \\ z^t - z_d \end{bmatrix} \tag{3.15}$$

where the desired trajectory satisfies $\bar{F}\left(\bar{X}\right) = \bar{0}$. For the fixed-time position targeting application, this $D\bar{F}\left(\bar{X}\right)$ matrix in Eqn. (3.10) is to be evaluated with the following elements

$$D\bar{F}\left(\bar{X}\right) = \begin{bmatrix} \frac{\partial F_1}{\partial X_1} & \frac{\partial F_1}{\partial X_2} & \frac{\partial F_1}{\partial X_3} \\ \frac{\partial F_2}{\partial X_1} & \frac{\partial F_2}{\partial X_2} & \frac{\partial F_2}{\partial X_3} \\ \frac{\partial F_3}{\partial X_1} & \frac{\partial F_3}{\partial X_2} & \frac{\partial F_3}{\partial X_3} \end{bmatrix} = \begin{bmatrix} \frac{\partial x^t}{\partial \dot{x}_0} & \frac{\partial x^t}{\partial \dot{y}_0} & \frac{\partial x^t}{\partial \dot{z}_0} \\ \frac{\partial y^t}{\partial \dot{x}_0} & \frac{\partial y^t}{\partial \dot{y}_0} & \frac{\partial y^t}{\partial \dot{z}_0} \\ \frac{\partial z^t}{\partial \dot{x}_0} & \frac{\partial z^t}{\partial \dot{y}_0} & \frac{\partial z^t}{\partial \dot{z}_0} \end{bmatrix} \tag{3.16}$$

It is quickly observed that this $D\bar{F}\left(\bar{X}\right)$ matrix of partials incorporates elements of the STM, such that

$$D\bar{F}\left(\bar{X}\right) = \begin{bmatrix} \phi_{14} & \phi_{15} & \phi_{16} \\ \phi_{24} & \phi_{25} & \phi_{26} \\ \phi_{34} & \phi_{35} & \phi_{36} \end{bmatrix} \tag{3.17}$$

where ϕ_{ij} refers to the element in the i^{th} row and j^{th} column of the STM matrix in Eqn. (3.4). Once the design vector, constraint vector, and Jacobian matrix are evaluated, each is employed to compute an update to the initial state, which ideally results in an updated trajectory that approaches the target state with less error than the previous iteration. For this particular problem formulation, observe that the $D\bar{F}\left(\bar{X}\right)$ matrix is square, therefore Eqn. (3.12) is employed to determine the appropriate correction to be applied to the initial design vector, $\delta\bar{X}$, such that

$$\delta\bar{X} = -D\bar{F}\left(\bar{X}\right)^{-1}\bar{F}\left(\bar{X}\right) \tag{3.18}$$

Then, simply update the design vector as

$$\bar{X}^{j+1} = \bar{X}^{j} + \delta\bar{X}^{j} \tag{3.19}$$

where j refers to the j^{th} iteration of the update process. To converge on a solution that reaches the target, this procedure is repeated until the norm of the constraint vector, $\left\|\bar{F}\left(\bar{X}\right)\right\|$, is less than the desired tolerance, indicating that the trajectory has reached the target to an acceptable level of accuracy.

3.3.2 Variable-Time Position Targeting

For some position targeting applications, it is desirable to let the time-of-flight (TOF) along the trajectory vary, as illustrated in the sketch in Figure 3.2. A variation in TOF is achieved with a variable-time position targeter. This targeting scheme is

very similar to the fixed-time position targeter, but with the addition of TOF, or T, to the design vector, such that

$$\bar{X} = \begin{bmatrix} \dot{x}_0 \\ \dot{y}_0 \\ \dot{z}_0 \\ T \end{bmatrix} \tag{3.20}$$

This addition to the design vector allows the TOF to vary during each subsequent iteration of the targeting procedure. The constraint vector remains the same as in Eqn. (3.15) for the fixed-time case. The Jacobian matrix, now evaluated as

$$D\bar{F}\left(\bar{X}\right) = \begin{bmatrix} \frac{\partial x^t}{\partial \dot{x}_0} & \frac{\partial x^t}{\partial \dot{y}_0} & \frac{\partial x^t}{\partial \dot{z}_0} & \frac{\partial x^t}{\partial T} \\ \frac{\partial y^t}{\partial \dot{x}_0} & \frac{\partial y^t}{\partial \dot{y}_0} & \frac{\partial y^t}{\partial \dot{z}_0} & \frac{\partial y^t}{\partial T} \\ \frac{\partial z^t}{\partial \dot{x}_0} & \frac{\partial z^t}{\partial \dot{y}_0} & \frac{\partial z^t}{\partial \dot{z}_0} & \frac{\partial z^t}{\partial T} \end{bmatrix} = \begin{bmatrix} \phi_{14} & \phi_{15} & \phi_{16} & \dot{x}^t \\ \phi_{24} & \phi_{25} & \phi_{26} & \dot{y}^t \\ \phi_{34} & \phi_{35} & \phi_{36} & \dot{z}^t \end{bmatrix} \tag{3.21}$$

is no longer square since there are more design variables than constraints. The minimum norm solution in Eqn. (3.13) is now used to compute the variation to be applied to the design vector, that is

$$\delta\bar{X} = -D\bar{F}\left(\bar{X}\right)^T \left[D\bar{F}\left(\bar{X}\right) D\bar{F}\left(\bar{X}\right)^T\right]^{-1} \bar{F}\left(\bar{X}\right) \tag{3.22}$$

and the updating process continues until the constraint vector is sufficiently small.

Numerical Example: Lyapunov Orbits

Spacecraft motion in the vicinity of the Lagrange points is of great interest for many mission applications. In Section 2.3.2, approximate, linear motion with respect to the collinear Lagrange points is analyzed. In this section, the STM and targeting techniques are employed with the nonlinear equations of motion to compute planar periodic orbits in the vicinity of the collinear points in the CR3BP. These orbits, sometimes labeled Lyapunov orbits, possess symmetry properties that are exploited to aid in the targeting process. The CR3BP is well known to exhibit symmetry across the $\hat{x}$-$\hat{z}$ plane. The planar Lyapunov orbits exist near the collinear points and are

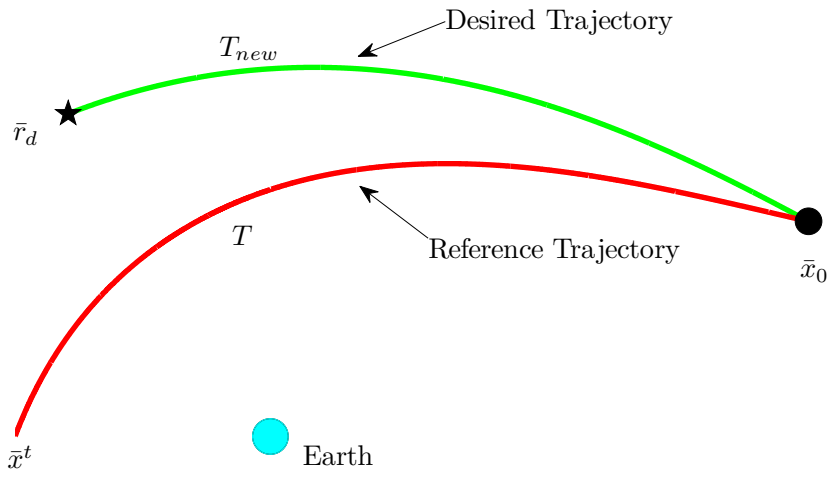

Figure 3.2. Variable-Time Position Targeting Scheme

planar. These periodic orbits are determined by exploiting the symmetry properties and the STM. Since the Lyapunov orbits are symmetric across the $\hat{x}$-axis, the Mirror Theorem [31] specifies that these orbits include two perpendicular $\hat{x}$-axis crossings. Therefore, in practice, only one-half of the orbit must be computed, i.e., time $t = 0$ to $t = T/2$; the second half of the trajectory, from $T/2$ to T, is simply determined by mirroring the first half of the orbit across the $\hat{x}$-axis.

To compute a reference trajectory to target a Lyapunov orbit, a convenient initial guess originates with the linear motion about the collinear points, assuming that the initial state is near the L_i point such that the linear approximation remains valid. Specifically, the initial condition is approximated from the linear motion that suppresses all divergent behavior, as in Eqns. (2.47). When these linear initial conditions are propagated in the nonlinear CR3BP model, the subsequent $\hat{x}$-axis crossing of the resulting trajectory is not perpendicular. The goal of the targerter, then, is to compute an orbit that does possess two perpendicular crossings, as appears in Figure 3.3.

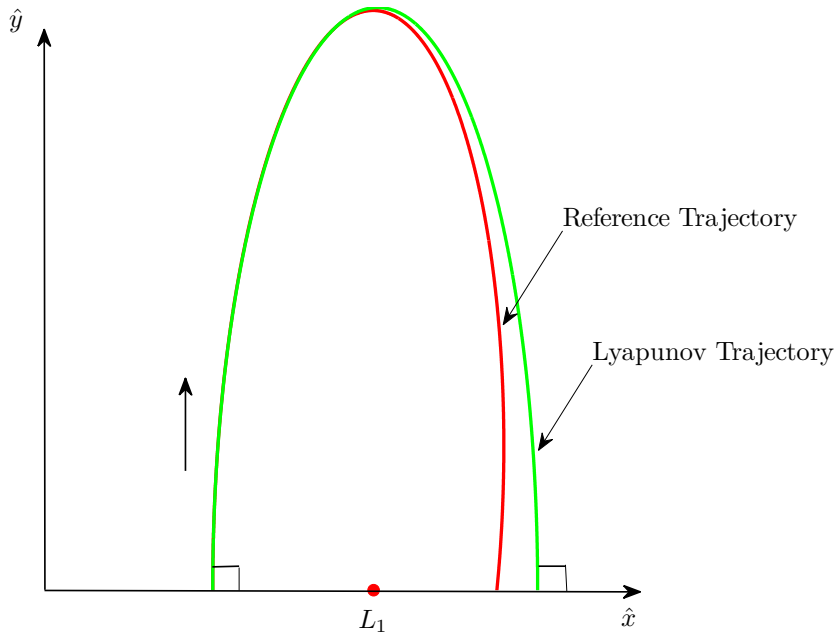

Figure 3.3. Targeting Scheme to Produce Perpendicular Crossings

Consistent with the formulation of a position targeter, implementation of the targeting algorithm for Lyapunov orbits is approached methodically by establishing design and constraint vectors. To define the design vector, first recall that this orbit is planar and let the linear initial conditions be located at a perpendicular $\hat{x}$-axis crossing; therefore, $y_0 = 0$, $\dot{x}_0 = 0$, and $z = \dot{z} = 0$ for all time along the Lyapunov. Next, let x_0 be fixed throughout the targeting iterations such that the final orbit possesses the same x_0. Given these considerations, the design vector only includes variables for the initial $\hat{y}$ velocity and the TOF along the trajectory, such that

$$\bar{X} = \begin{bmatrix} \dot{y}_0 \\ T \end{bmatrix} \tag{3.23}$$

To ensure another perpendicular crossing at the end of the trajectory, the constraint vector $\bar{F}\left(\bar{X}\right)$ is defined

$$\bar{F}\left(\bar{X}\right) = \begin{bmatrix} y^t \\ \dot{x}^t \end{bmatrix} = \bar{0} \tag{3.24}$$

Based on the given design and constraint vectors, the Jacobian matrix becomes

$$D\bar{F}\left(\bar{X}\right) = \begin{bmatrix} \frac{\partial y^t}{\partial \dot{y}_0} & \frac{\partial y^t}{\partial T} \\ \frac{\partial \dot{x}^t}{\partial \dot{y}_0} & \frac{\partial \dot{x}^t}{\partial T} \end{bmatrix} = \begin{bmatrix} \phi_{25} & \dot{y}^t \\ \phi_{45} & \ddot{x}^t \end{bmatrix} \tag{3.25}$$

Since the Jacobian matrix is square, the corrections to be applied to the initial state are solved using Eqn. (3.18) such that

$$\begin{bmatrix} \delta\dot{y}_0 \\ \delta T \end{bmatrix} = - \begin{bmatrix} \phi_{25} & \dot{y}^t \\ \phi_{45} & \ddot{x}^t \end{bmatrix}^{-1} \begin{bmatrix} y^t \\ \dot{x}^t \end{bmatrix} \tag{3.26}$$

However, a further simplification is exploited for the Lyapunov orbits. The numerical integration is terminated when the trajectory reaches the next $\hat{x}$-axis crossing and, thus, $y^t = 0$ is the stopping condition for the integration process rather than time. As noted in Figure 3.3, at the stopping condition, $\dot{y}^t < 0$ and the linear estimate for the time correction is then

$$\delta T = -\frac{1}{\dot{y}^t}\left(\phi_{25}\delta\dot{y}_0\right) \tag{3.27}$$

Essentially, the TOF is defined as the value of T to reach the next crossing of the $\hat{x}$-axis. Generally, the condition for a perpendicular crossing, $\dot{x}^t = 0$, is not satisfied. The relationship in Eqn. (3.27) is substituted into the second equation for δT in Eqn. (3.26). The equation is then rewritten to solve directly for the correction term $\delta\dot{y}_0$

$$\delta\dot{y}_0 = -\left(\phi_{45} - \frac{\ddot{x}^t}{\dot{y}^t}\phi_{25}\right)^{-1}\dot{x}^t \tag{3.28}$$

where $\delta\dot{y}_0$ is now a scalar, and is the only variable that requires correction to compute the Lyapunov orbit. A representative Lyapunov computed with this approach appears in Figure 3.4. Note that this Lyapunov orbits exists near the L_1 Lagrange point, but Lyapunov orbits exist in the vicinity of all of the collinear libration points.

3.4 Multiple Shooting Technique

The single-shooting targeting techniques use one trajectory arc to satisfy the desired conditions. A single-shooting algorithm is useful for many applications, but

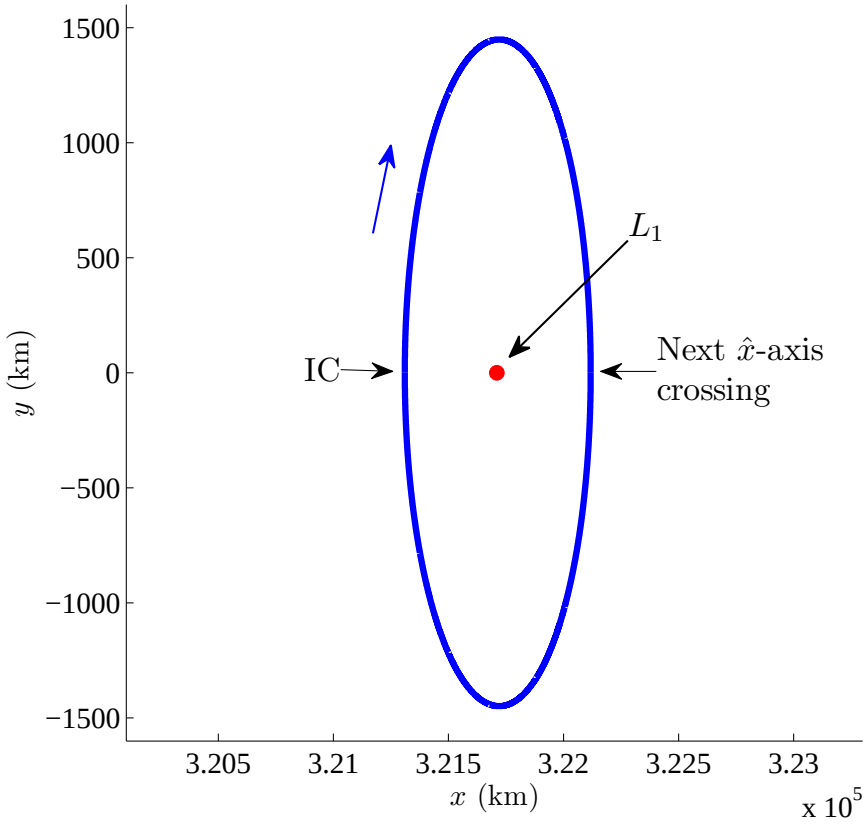

Figure 3.4. A Single L_1 Lyapunov Orbit in the Earth-Moon System

in some scenarios, the numerical sensitivities are extremely high, and one arc is not sufficient. In such examples, which may include trajectories with many nonlinear elements, for example, trajectories that pass very close to a primary body, the targeting process is more successful if the path is decomposed into multiple smaller arcs. This technique is frequently denoted "multiple shooting".

A schematic of the multiple shooting concept appears in Figure 3.5. The reference states, also labeled patch points, are denoted $\bar{x}_i$. The state vectors corresponding to the patch points are integrated forward by some time T, resulting in the final states, labeled $\bar{x}_i^t$. Such a final state usually does not coincide with the subsequent patch point state. Therefore, the goal of a multiple shooting algorithm is generally to create a trajectory continuous in position and velocity through all the patch points. The

specific implementation algorithm for several types of multiple shooting schemes is detailed below.

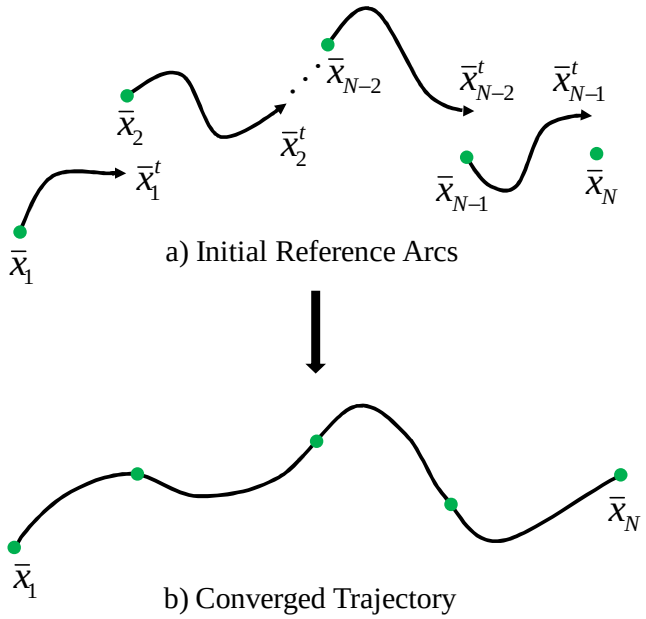

Figure 3.5. Multiple Shooting Conceptual Diagram

3.4.1 Fixed-Time Multiple Shooting

Consistent with single-shooting targeters, the development of a multiple shooting algorithm is approached from the perspective of design variables and constraint vectors. Assume that the integration time along each arc segment, T_i, is fixed. Then, the design vector $\bar{X}$ includes the variables available for adjustment. For simplicity, it is initially assumed in this example that all of the patch point position and veloc-

ity states are free, therefore, all six-dimensional vectors are included in the complete design vector $\bar{X}$, yielding a design vector of length $6N$, that is

$$\bar{X} = \begin{bmatrix} \bar{x}_1 \\ \bar{x}_2 \\ \vdots \\ \bar{x}_{N-1} \\ \bar{x}_N \end{bmatrix} \tag{3.29}$$

Next, the constraint vector $\bar{F}\left(\bar{X}\right)$ is formulated. In general, the final trajectory is not required to be continuous in velocity at every patch point. This discontinuity in velocity would simply imply that impulsive maneuvers are required at these locations. However, in this example, assume that the desired trajectory is continuous in position and velocity, resulting in the constraint vector

$$\bar{F}\left(\bar{X}\right) = \begin{bmatrix} \bar{x}_1^t - \bar{x}_2 \\ \bar{x}_2^t - \bar{x}_3 \\ \vdots \\ \bar{x}_{N-2}^t - \bar{x}_{N-1} \\ \bar{x}_{N-1}^t - \bar{x}_N \end{bmatrix} \tag{3.30}$$

of length $6\left(N-1\right)$. This constraint vector requires that the final state corresponding to patch point $i-1$ is equal to the initial state originally specified for patch point i, resulting in a continuous trajectory. From the design and constraint vectors, the Jacobian matrix is

$$D\bar{F}\left(\bar{X}\right) = \begin{bmatrix} \left(\frac{\partial \bar{x}_1^t}{\partial \bar{x}_1} - \frac{\partial \bar{x}^2}{\partial \bar{x}_1}\right) & \left(\frac{\partial \bar{x}_1^t}{\partial \bar{x}_2} - \frac{\partial \bar{x}^2}{\partial \bar{x}_2}\right) & & \\ & \ddots & \ddots & \\ & & \left(\frac{\partial \bar{x}_1^t}{\partial \bar{x}_{N-1}} - \frac{\partial \bar{x}^2}{\partial \bar{x}_{N-1}}\right) & \left(\frac{\partial \bar{x}_1^t}{\partial \bar{x}_N} - \frac{\partial \bar{x}^2}{\partial \bar{x}_N}\right) \end{bmatrix} \tag{3.31}$$

which, from observation, is further reduced to

$$D\bar{F}\left(\bar{X}\right) = \begin{bmatrix} \Phi_1^t & -I_{6\times 6} & & \\ & \ddots & \ddots & \\ & & \Phi_{N-1}^t & -I_{6\times 6} \end{bmatrix} \tag{3.32}$$

where Φ_i^t refers to the 6×6 STM resulting from the state at patch point i numerically propagated forward in time. Now, the update equation in Eqn. (3.22) is applied, and the process is repeated iteratively until the norm of the constraint vector is sufficiently small.

3.4.2 Variable-Time Multiple Shooting

For added flexibility, the multiple shooting algorithm is modified so that the time T_i between patch points is allowed to vary. To implement this alternative formulation, let the design vector be augmented with $N-1$ additional scalars, i.e., the times between patch points, such that $\bar{X}$ is of length $7N-1$

$$\bar{X} = \begin{bmatrix} \bar{x} \\ \vdots \\ \bar{x}_N \\ T_1 \\ \vdots \\ T_{N-1} \end{bmatrix} \tag{3.33}$$

Again assuming that the only constraints on the trajectory are continuity in position and velocity, the constraint vector of length $6\,(N-1)$ is identical to the vector defined in the fixed-time alternative,

$$\bar{F}\left(\bar{X}\right) = \begin{bmatrix} \bar{x}_1^t - \bar{x}_2 \\ \bar{x}_2^t - \bar{x}_3 \\ \vdots \\ \bar{x}_{N-2}^t - \bar{x}_{N-1} \\ \bar{x}_{N-1}^t - \bar{x}_N \end{bmatrix} \tag{3.34}$$

Since the design vector now includes time variables, the Jacobian matrix is more complex than for the fixed-time case. It is evaluated as

$$D\bar{F}\left(\bar{X}\right) = \begin{bmatrix} \Phi_1^t & -I_{6\times 6} & & & \dot{\bar{x}}_1^t & \\ & \ddots & \ddots & & & \ddots \\ & & \Phi_{N-1}^t & -I_{6\times 6} & & \dot{\bar{x}}_{N-1}^t \end{bmatrix} \tag{3.35}$$

where $\dot{\bar{x}}_i^t$ refers to the time derivative $\frac{\partial \bar{x}_i^t}{\partial T_i}$. The update formula in Eqn. (3.22) is now applied, and repeated iteratively until the norm of the constraint vector is sufficiently small.

3.4.3 Targeting Asymmetric Periodic Orbits with Multiple Shooting

As an example in Section 3.3.2, periodic orbits are targeted by exploiting symmetry properties in the CR3BP. However, when targeting periodic orbits that lack symmetry, a more general method is necessary. A general approach is implemented within the context of either a single shooting or multiple shooting scheme; in this application, a multiple shooting algorithm is appropriate. Since symmetry and perpendicular crossings are not utilized, periodicity constraints are introduced, such that $x_1 = x_N$, $y_1 = y_N$, and so on. Note that if periodicity constraints are enforced on all 6 states, however, the numerical algorithm may struggle to converge since the problem is over-constrained. To overcome this difficulty, only five states (three position states and two velocity states) possess periodicity constraints, and an additional slack variable is introduced. A slack variable is generally used to rewrite inequality constraints as equalities [32]. The periodicity requirement is enforced but formulated in terms of an inequality constraint. For this application, it is useful to define a slack variable, β, such that $\dot{y}_N^t + \beta^2 = 0$. This ensures that the final $\hat{y}$-velocity, $\dot{y}_N^t$, is always negative. The selection of a negative $\dot{y}_N^t$ is based upon the location of the first patch point, i.e., $t = 0$, along the orbit, in this example, possibly a periodic orbit about L_4. Assuming an orbital motion that is clockwise, and a first patch point that is near the position of maximum x-excursion, then the initial and final $\hat{y}$-velocity

is expected to be negative. Since the slack variable depends on the initial position, it is also convenient, then, to fix the initial $\hat{y}$-position. The combination of the slack variable constraint and the constraint on initial $\hat{y}$-position should ensure that the orbit maintains the desired characteristics throughout the targeting process without explicitly incorporating a 6^{th} periodicity constraint. Once this general formulation is established, the design and constraint vectors are defined as required for a particular application.

Numerical Example: Asymmetric Short-Period Orbit about L_4

Since L_4 and L_5 are not located on the $\hat{x}$-axis, the planar, periodic orbits that exist in their vicinity do not possess axial or planar symmetry. Therefore, a periodic orbit about L_4 is computed to illustrate the process to target asymmetric periodic orbits. First, let the design vector, of length $6N + 2$ include the patch point states, the total period, T, and the slack variable, β, such that

$$\bar{X} = \begin{bmatrix} \bar{x}_1 \\ \vdots \\ \bar{x}_N \\ T \\ \beta \end{bmatrix} \tag{3.36}$$

Note that, in this formulation, the period is variable, and the time between the N patch points is evenly spaced into intervals of duration of T/N. An initial guess for the state vectors at the patch points originates with the analytical solution for short-period motion about L_4 developed in Section 2.3.3. The patch points are arbitrarily selected to be evenly spaced in time along the analytically determined reference. Note that this analytical solution is only valid in the nearby vicinity of L_4. The constraint vector is developed next. Consistent with the previous multiple shooting algorithms, constraints are included such that position and velocity is continuous at the patch points. Then, the asymmetric targeting constraints are included, that is,

five periodicity constraints, a slack variable constraint, and a constraint on the initial $\hat{y}$-position. In this example, the initial $\hat{y}$-position is constrained to equal that of L_4. The design vector of length $6N+1$, then, is defined as

$$\bar{F}\left(\bar{X}\right) = \begin{bmatrix} \bar{x}_1^t - \bar{x}_2 \\ \vdots \\ \bar{x}_{N-1}^t - \bar{x}_N \\ x_N^t - x_1 \\ y_N^t - y_1 \\ z_N^t - z_1 \\ \dot{x}_N^t - \dot{x}_1 \\ \dot{y}_N^t + \beta^2 \\ \dot{z}_N^t - \dot{z}_1 \\ y_1 - y_{L_4} \end{bmatrix} \tag{3.37}$$

From the design and constraint vectors, the Jacobian matrix is derived. After simplification, the resulting Jacobian is evaluated from

$$D\bar{F}\left(\bar{X}\right) = \begin{bmatrix} \Phi_1^t & -I_{6\times 6} & & & \frac{\dot{\bar{x}}_1^t}{N} & \\ & \ddots & \ddots & & \vdots & \\ & & \Phi_{N-1}^t & -I_{6\times 6} & \frac{\dot{\bar{x}}_{N-1}^t}{N} & \\ A & & & \Phi_N^t & \frac{\dot{\bar{x}}_N^t}{N} & B \\ C & & & & & \end{bmatrix} \tag{3.38}$$

where the unspecified elements of the matrix are zero, and the submatrices A, B, and C are defined as

$$A = \begin{bmatrix} -1 & 0 & 0 & 0 & 0 & 0 \\ 0 & -1 & 0 & 0 & 0 & 0 \\ 0 & 0 & -1 & 0 & 0 & 0 \\ 0 & 0 & 0 & -1 & 0 & 0 \\ 0 & 0 & 0 & 0 & 0 & 0 \\ 0 & 0 & 0 & 0 & 0 & -1 \end{bmatrix} \tag{3.39}$$

$$B = \begin{bmatrix} 0 \\ 0 \\ 0 \\ 0 \\ 2\beta \\ 0 \end{bmatrix} \tag{3.40}$$

$$C = \begin{bmatrix} 0 & 1 & 0 & 0 & 0 & 0 \end{bmatrix} \tag{3.41}$$

Now, the update equation in Eqn. (3.22) is implemented, and the iterations continue until the norm of the constraint vector is sufficiently small. The resulting trajectory, plotted in Figure 3.6, is a continuous, asymmetric periodic orbit. For this particular example, four patch points from the analytical solution are used to initiate the multiple shooting process in the nonlinear CR3BP system. Note that alternative numerical implementations of single- and multiple-shooting concepts, such as the approach by Markellos and Halioulias [33], are equally as effective in computing asymmetric periodic orbits.

3.5 Generating Families of Periodic Orbits

Periodic orbits that exist in the vicinity of the libration points are examples of the application of numerical targeting techniques. However, an infinite number of periodic orbits exist near the libration points [13]. To uncover some subset of these orbits, a family of periodic orbits is computed using a continuation scheme from one initial periodic orbit. Natural parameter continuation as well as pseduo-arclength continuation are two techniques for computing these families.

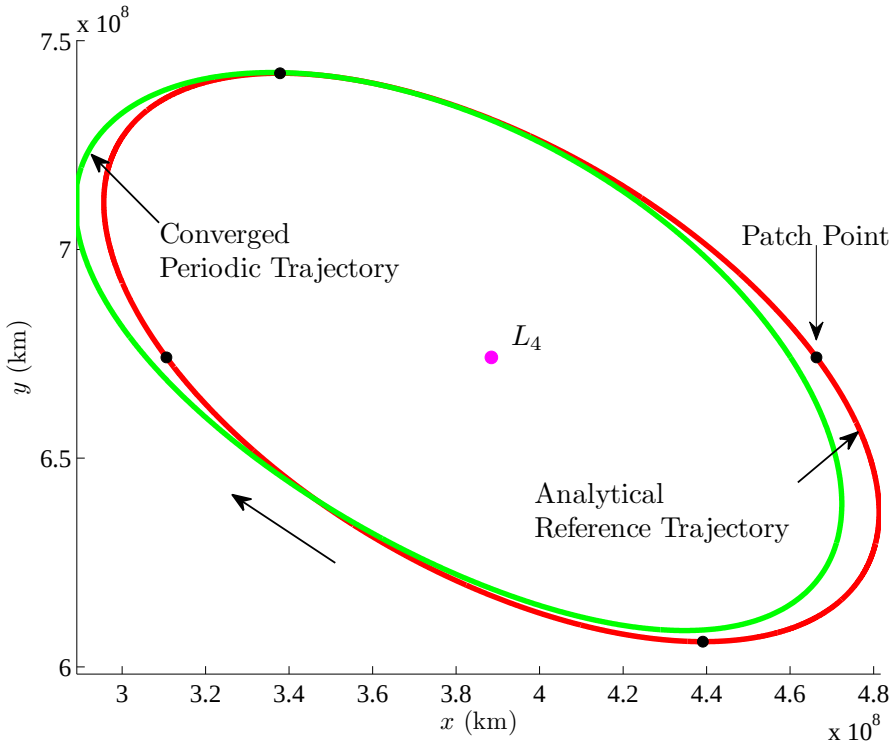

Figure 3.6. Nonlinear Short-Period Orbit about L_4 Computed via Multiple Shooting Technique

3.5.1 Method: Natural Parameter Continuation

Natural parameter continuation is one of the simplest methods for generating a family of periodic orbits [30]. A natural parameter refers to a naturally occurring variable that appears in the system model, such as an initial Cartesian coordinate, time-of-flight, or energy. In a natural parameter continuation scheme, this natural parameter is selected to define a family of orbits; a unique orbit is defined for each value of the parameter. A new member of a family is computed by using the initial conditions from a previously converged member as an initial guess, and varying the desired natural parameter. Using this method, the initial guess for targeting a periodic orbit originates from slightly altering a previously converged nearby family member instead of developing entirely new initial conditions.

3.5.2 Numerical Example: Families of Lyapunov Orbits

From a single Lyapunov orbit computed using any targeting technique, a family of Lyapunov orbits is developed using natural parameter continuation. The parameter selected to define the family is the distance between the libration point of interest and the $\hat{x}$-axis crossing of a Lyapunov orbit. Given the two $\hat{x}$-axis crossings for a specific Lyapunov orbit in the vicinity of a particular libration point, it is convenient to select the crossing located opposite the nearest primary with respect to the libration point to define the orbit. Thus, the natural parameter representing each member of the family is x_0. Then, a new Lyapunov orbit is identified by varying the location of x_0 from the previously converged periodic orbit; the value of x_0 is constrained to be fixed during the targeting procedure to converge this initial guess to a periodic orbit. Families of L_1, L_2, and L_3 Lyapunov orbits that are computed with this continuation strategy appear in Figure 3.7. Note that, for visual clarity, only select members of the family are plotted.

3.5.3 Method: Pseudo-Arclength Continuation

An alternative to a natural parameter continuation technique is pseudo-arclength continuation. In this approach, introduced in 1977 by Keller [34], subsequent family members are determined by "stepping off" the previous orbit and approximating the arclength to reach the next member in a direction tangent to the family. Pseudo-arclength continuation is not intuitive in contrast to natural parameter continuation. However, in using pseudo-arclength continuation, prior knowledge of the evolution of an orbit family is not necessary, which is a significant advantage. In natural parameter continuation, for instance, the algorithm may attempt to step in a direction in which the orbit family simply does not actually evolve.

The procedure for implementing Keller's pseudo-arclength continuation scheme requires only minor alterations to an existing targeting scheme, and is outlined by Pavlak [30] and Chen [35]. The corrections process originates from a previously

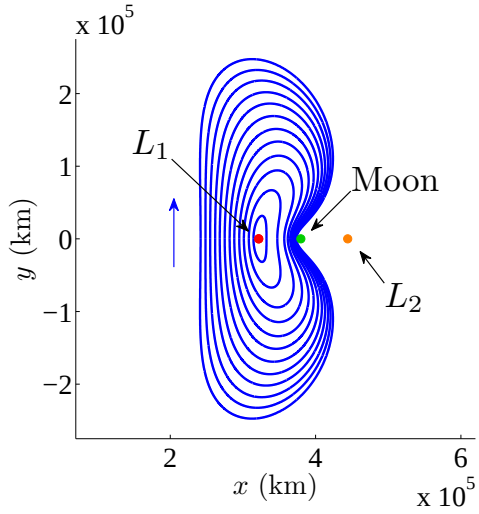

(a) L_1 Lyapunov Family

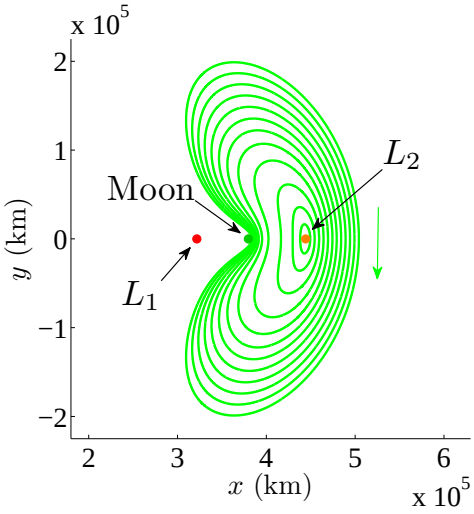

(b) L_2 Lyapunov Family

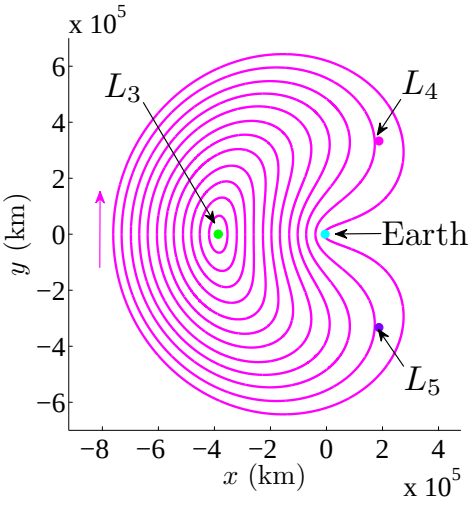

(c) L_3 Lyapunov Family

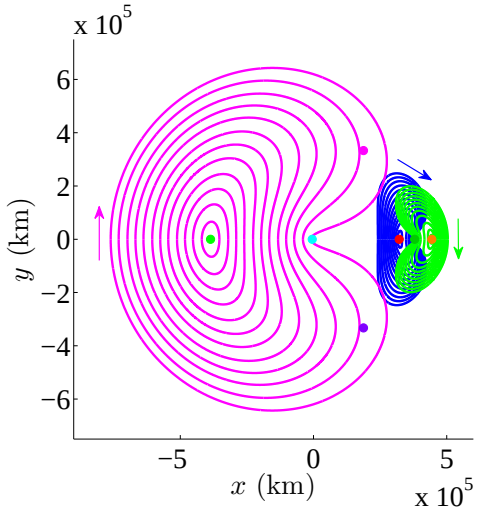

(d) L_3, L_2, L_3 Lyapunov Families

Figure 3.7. Lyapunov Orbits in the Earth-Moon System

converged family member, denoted $\bar{X}^*_{i-1}$. From this initial orbit, a unit vector tangent to the family is determined by computing the null vector, denoted $\Delta\bar{X}^*_{i-1}$, of the Jacobian matrix $D\bar{F}\left(\bar{X}^*_{i-1}\right)$. Then, the next member of the family is computed by stepping an amount Δs along the tangent direction. To compute this new family member, an augmented constraint vector, $\bar{G}\left(\bar{X}\right)$ is defined as

$$\bar{G}\left(\bar{X}_i\right) = \begin{bmatrix} \bar{F}\left(\bar{X}_i\right) \\ \left(\bar{X}_i - \bar{X}^*_{i-1}\right)^T \Delta\bar{X}^*_i - \Delta s \end{bmatrix} \tag{3.42}$$

where $\bar{F}\left(\bar{X}_i\right)$ is the existing constraint vector for the targeting scheme. For applications with one more free variable than constraint, such as the algorithm for asymmetric periodic orbits, the number of constraints in the augmented constraint vector is then equal to the number of free variables in the design vector. The augmented constraint vector, $\bar{G}\left(\bar{X}_i\right)$ leads to a new Jacobian matrix, i.e.,

$$D\bar{G}\left(\bar{X}_i\right) = \begin{bmatrix} D\bar{F}\left(\bar{X}_i\right) \\ \Delta\bar{X}^{*T}_i \end{bmatrix} \tag{3.43}$$

which is square for applications with an augmented constraint vector equal in length to the design vector, and therefore yields a unique guess for the next family member, $\bar{X}_i$. The update equation is applied and the iterative process proceeds until the norm of the constraint vector is sufficiently small.

3.5.4 Numerical Example: Families of Periodic Orbits about the L_4 and L_5 Equilibrium Points

To illustrate the effectiveness of the pseudo-arclength continuation method, families of short and long-period orbits about L_4 and L_5 are developed. An initial L_4 or L_5 short-period or long-period orbit is computed via any convenient targeting technique. Then, the pseudo-arclength algorithm is incorporated into the targeting scheme to develop an entire family of periodic orbits, such as the asymmetric families in Figure 3.8. Note that L_4 and L_5 themselves are mirrored across the $\hat{x}$-axis; the periodic

orbits also exhibit the symmetry expected in the CR3BP. Once the periodic orbits about L_4 have been computed, the periodic orbits about L_5 are available by simply mirroring the L_4 orbits across the $\hat{x}$-axis.

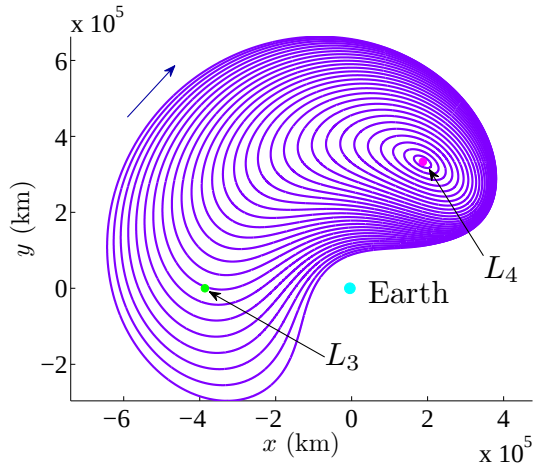

(a) L_4 Short-Period Family

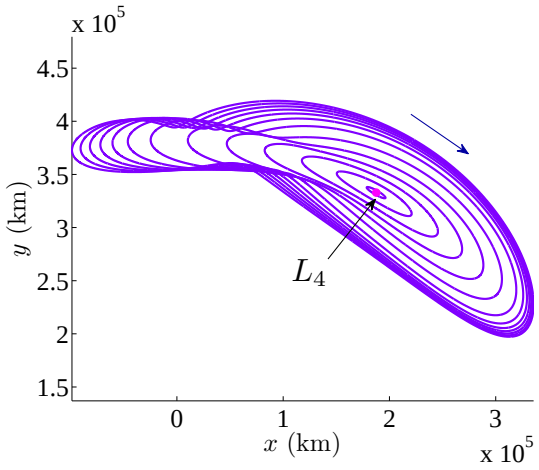

(b) L_4 Long-Period Family

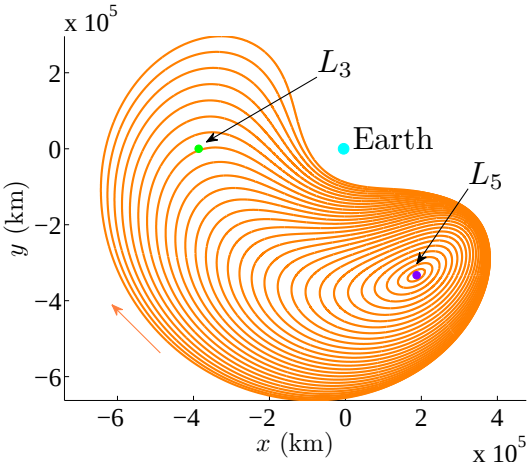

(c) L_5 Short-Period Family

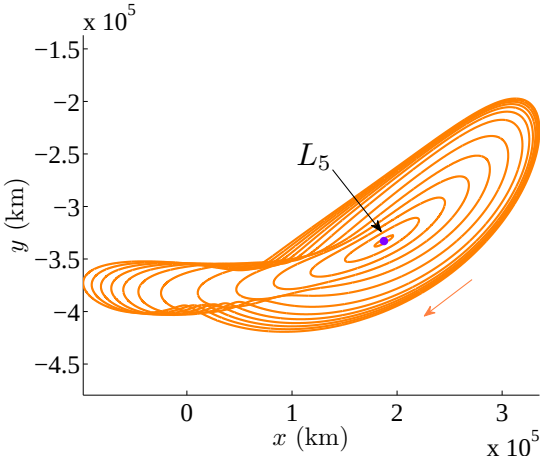

(d) L_5 Long-Period Family

Figure 3.8. Periodic Orbits about L_4 and L_5 in the Earth-Moon System

3.6 Poincaré Maps

Poincaré maps provide a classical technique for analyzing dynamical systems [36]. Poincaré maps replace "the flow of an nth order system with a discrete-time system with the order $(n-1)$ [37]." To better understand this statement, a sample Poincaré map is developed. To construct a Poincaré map, first define a Poincaré section, Σ, as demonstrated in Figure 3.9. This surface of section possesses dimension $(n-1)$, and is located transverse to the flow. Then, the Poincaré map is developed by marking intersections of the propagated flow with the Poincaré section [37]. In the sketch of a Poincaré map in Figure 3.9, the trajectory defined by the point $\bar{x}_1$ on the hyperplane Σ is a periodic orbit, therefore $\bar{x}_1$ is a fixed point and the associated trajectory always returns to the same position on the map. The trajectory represented on the map by $\bar{x}_2$ is not periodic, and its subsequent return to the map is denoted $P(\bar{x}_2)$. The trajectory represented by $\bar{x}_3$ does not return to the Poincaré section within the given time interval.

3.7 The Stability of Periodic Solutions

Periodic solutions are very useful in understanding the dynamics of motion in the vicinity of the Lagrange points. However, in practical terms, it is likely that a spacecraft path is actually slightly perturbed from the periodic trajectory. Therefore, knowledge concerning the stability of the periodic solutions is valuable. Recall that periodic orbits are represented by a fixed point on a Poincaré map. The stability of the periodic orbit and of its associated fixed point are the same [36]. To determine this stability, the fixed point is propagated forward in time by exactly one period, $\boldsymbol{T}$. The STM resulting from this single-period propagation is labeled the monodromy matrix. The eigenvalues of the monodromy matrix are the characteristic multipliers of the system of variational equations, Eqn. (3.1), evaluated on the periodic reference orbit [38]. Since the fixed point represents a six-element state vector, there are six corresponding eigenvalues of the monodromy matrix. Because the CR3BP represents

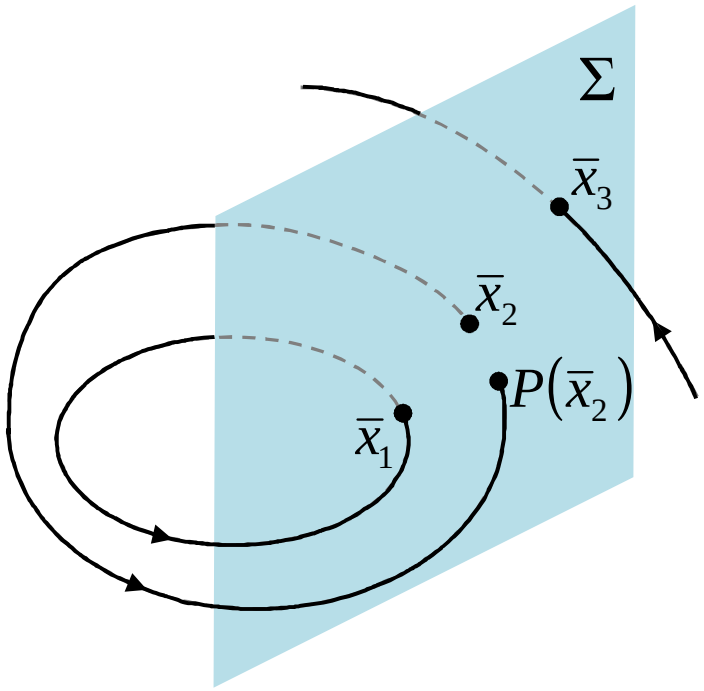

Figure 3.9. Illustration of a Poincaré Map on the Hyperplane Σ

a Hamiltonian system, these eigenvalues occur in reciprocal and complex conjugate pairs. Let some non-zero eigenvalue be denoted λ_i. Then, if λ_i is real, there is another eigenvalue λ_j such that $\lambda_j = \frac{1}{\lambda_i}$, and if λ_i is complex, $\lambda_j = \lambda_i^*$, where λ_i^* denotes the complex conjugate of λ_i [39]. Jordan and Smith demonstrate that there exist periodic solutions whenever there is a characteristic multiplier equal to unity [38]. Therefore, for periodic orbits in this system, two of the six characteristic multipliers are equal to unity.

Given the pair of unity eigenvalues that identify periodicity, the remaining four characteristic multipliers are useful in determining the stability of the periodic orbit. The characteristic multipliers determine the stability of a fixed point on a map as well as the underlying periodic orbit, just as eigenvalues determine the stability of

an equilibrium point. The magnitude of a characteristic multiplier determines the corresponding subspace [40], such that

$$|\lambda_j| < 1 \Rightarrow \text{stable subspace},$$
$$|\lambda_j| > 1 \Rightarrow \text{unstable subspace},$$
$$|\lambda_j| = 1 \Rightarrow \text{center subspace}$$

Using this information, the stability of the periodic orbit is implied. If any characteristic multipliers, corresponding to the monodromy matrix, exist such that $|\lambda_j| > 1$ (which also implies that there are characteristic multipliers satisfying $|\lambda_j| < 1$ since they appear in reciprocal pairs), the orbit is unstable. Therefore, a periodic orbit is marginally stable in a linear sense only if all the characteristic multipliers are of unit magnitude [27].

3.8 Invariant Manifold Theory

A stability analysis naturally leads to the study of the flow to and from an equilibrium point or a periodic orbit. Parker and Chua define the invariant manifolds of any equilibrium point such that if L is a non-chaotic hyperbolic limit set of the flow, then the stable manifold is the set of points whose trajectory approaches L as $t \to \infty$, and the unstable manifold is the set of points whose trajectory approaches L as $t \to -\infty$. The invariant manifolds of a fixed point corresponding to a periodic orbit are defined similarly, except that L is defined as a non-chaotic hyperbolic limit set of a map, P [36]. A detailed analysis of invariant manifold theory is also presented in Perko [41]. If an equilibrium point or periodic orbit possesses an eigenvalue pair corresponding to the unstable and stable subspace, then there exists unstable and stable invariant manifolds for that equilibrium point or periodic orbit. A trajectory arc that naturally flows to or from a periodic orbit is ideal for a preliminary step in the design of a transfer. Locating an arc in the stable or unstable subspace can serve as an initial guess in a transfer trajectory construction process. To determine a state within the appropriate subspace requires a technique to compute a stable or unstable

manifold trajectory. As an initial guess for the manifolds, let W^U_{loc} and W^S_{loc} denote the local unstable and stable manifolds, respectively. For an equilibrium point, the direction for these local manifolds is approximated by evaluating the eigenvectors corresponding to the point. The unstable eigenvector corresponds to the direction of W^U_{loc} while the stable eigenvector supplies the direction for W^S_{loc}. Similarly, for a periodic orbit, the direction for these local manifolds is determined at any particular fixed point along the orbit by evaluating the eigenvectors of the monodromy matrix for the corresponding fixed point.

Since W^U_{loc} and W^S_{loc} only serve as linear approximations to the manifolds very near the equilibrium solution or fixed point, the corresponding nonlinear global manifolds must also be computed. First, for convenience, the stable and unstable eigenvectors are normalized such that the position components of the eigenvectors are of unit length [42]. The initial conditions for computing the global unstable and stable manifolds, denoted W^U and W^S, are determined by stepping off the equilibrium or fixed point by an appropriately small distance, d, onto the normalized unstable and stable eigenvectors, respectively. Integrating the corresponding initial condition forward in time yields the unstable global manifold, while integrating the proper initial condition backward in time yields the stable global manifold. Eigenvectors deliver orientation information but not sense. Thus, all manifolds are approximated to arrive or depart in two directions that are opposite in sense.

The local and global manifolds for an equilibrium point with the associated state vector $\bar{x}$ are illustrated in Figure 3.10. In the figure, the stable and unstable eigenvector directions are plotted and labeled E^S and E^U, respectively. The local stable and unstable manifolds, W^S_{loc} and W^U_{loc}, are plotted along with the corresponding global manifolds, W^S and W^U. The $\pm$ notation indicates a half-manifold, such that W^{S^+} denotes the stable half-manifold computed by stepping a distance d in the positive direction along the stable eigenvector, and W^{S^-} refers to the stable half-manifold determined by stepping the same distance in the negative direction along the eigenvector. Note that, in this figure, the manifolds asymptotically approach or depart

the equilibrium point. However, the stable and unstable manifolds corresponding to a periodic orbit asymptotically approach and depart the orbit, respectively. If the manifolds corresponding to a fixed point on the periodic orbit are recorded on a Poincaré section, the resulting Poincaré map would contain discrete points that, if connected, would look similar to the global manifolds in Figure 3.10.

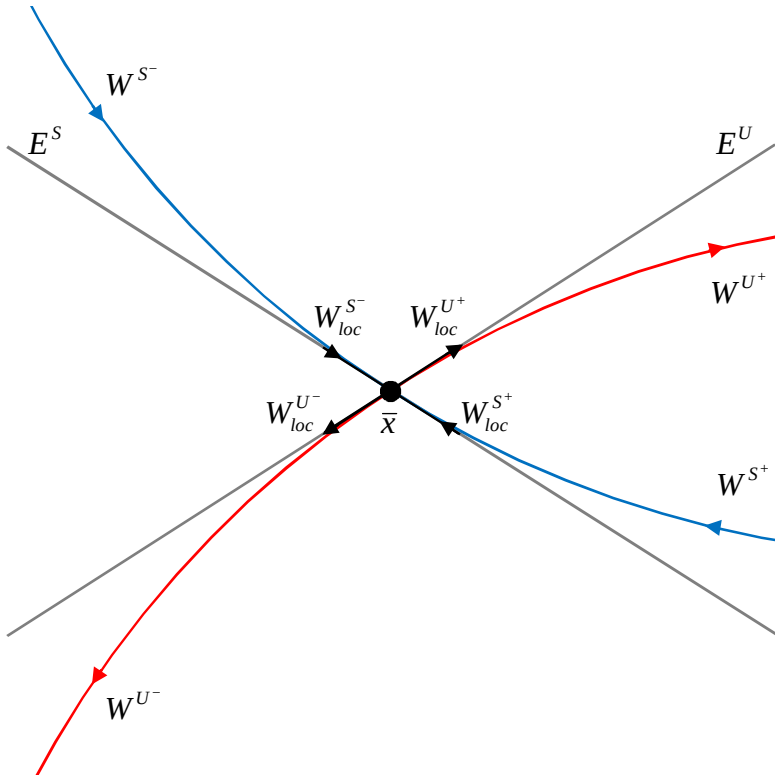

Figure 3.10. Unstable and Stable Manifolds of an Equilibrium Point

4. HORSESHOE ORBITS

Before transfers to horseshoe orbits are investigated, it is important to establish the definition of a horseshoe orbit and strategies for its computation. First, the technique employed for locating planar, periodic horseshoe orbits is detailed. Then, families of periodic horseshoe orbits are developed. The frequencies and resonances associated with the horseshoe orbits are then summarized. Stability information regarding the horseshoes is investigated and reveals valuable information about possible transfer trajectories.

4.1 Computing Periodic Horseshoe Orbits

Let a horseshoe orbit be defined as a periodic solution that encompasses only the L_3, L_4, and L_5 equilibrium points [17]. In this investigation, only planar horseshoe orbits are currently examined. To illustrate the typical appearance of horseshoe orbits, consider the simple horseshoe orbit plotted in both the rotating and inertial frames in Figure 4.1. In the rotating frame, a simple horseshoe orbit includes two perpendicular $\hat{x}$-axis crossings, although there may be additional non-perpendicular $\hat{x}$-axis crossings, depending on the complexity of the horseshoe trajectory. Consistent with Lyapunov orbits, horseshoe orbits exhibit symmetry across the $\hat{x}$-axis because of the mirror theorem [31]. Various methods are employed by researchers to compute periodic horseshoe orbits [14], [15].

4.1.1 Near-Periodic Horseshoe Orbits: Search and Filter Techniques

Numerical approaches to compute horseshoe orbits have been sought in the literature for over four decades. A search and filter technique, similar to that used in 1967

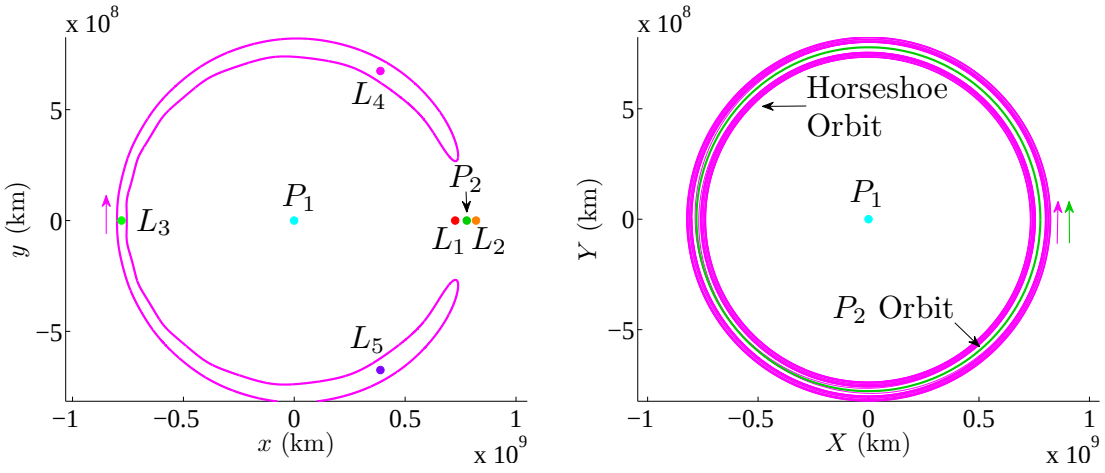

(a) Rotating View

(b) Inertial View

Figure 4.1. Rotating and Inertial Views of a Horseshoe Orbit

by Schanzle [15] is initially explored to compute horseshoe orbits with the potential to be periodic. Historically, the process is initiated by selecting initial conditions that are likely to produce a periodic orbit. Similar to Lyapunov orbits, the initial state vector appears in the form

$$\bar{x}_0 = \begin{bmatrix} x_0 \\ 0 \\ 0 \\ 0 \\ \dot{y}_0 \\ 0 \end{bmatrix} \tag{4.1}$$

This initial state vector, with only two non-zero elements, has the necessary form to produce a periodic orbit with perpendicular $\hat{x}$-axis crossings. Given the general characteristics of a horseshoe orbit as viewed in the rotating frame, these conditions are most likely to succeed. The initial conditions lie on the $\hat{x}$-axis with an initial velocity only in the $\hat{y}$-direction. Such an assumption also exploits the symmetry properties across the $\hat{x}$-axis that is fundamental in the CR3BP. A search process then proceeds. Since the horseshoe orbits encompass L_3, a convenient first step is a sweep

across a range of possible x_0 values, all left of L_3 as illustrated Figure 4.2(a). The second step in this search process is a sweep across a range of $\dot{y}_0$ values for each of the sample values of x_0, as apparent in Figure 4.2(b). The general shape of a simple horseshoe orbit resembles that of a ZVC corresponding to a value of Jacobi constant between that of C_{L_2} and C_{L_3}. Thus, a convenient set of values for $\dot{y}_0$ ranges from zero to the velocity necessary to achieve an energy level equal to that of L_4 at the given x_0 position. This large set of initial conditions is then propagated forward to the next $\hat{x}$-axis crossing. The $\hat{x}$-velocity component of the state at this crossing ($\dot{x}_f$) is recorded, and a plot, represented in Figure 4.2(c), is created to relate the initial $\hat{y}$-velocity to the final $\hat{x}$-velocity. Since a desired periodic horseshoe orbit includes two perpendicular $\hat{x}$-axis crossings, this plot is used to locate an appropriate value of $\dot{y}_0$, that is, a value that results in a zero-valued $\dot{x}_f$. Using (i) the value of $\dot{y}_0$ as interpolated from the plot as well as (ii) the initial location on the $\hat{x}$-axis as a set of initial conditions, this state is propagated for two crossings of the $\hat{x}$-axis. This propagation results in a near-periodic orbit, such as the horseshoe orbit plotted in Figure 4.2(d). Note that this horseshoe orbit is not actually periodic, although this fact is not apparent from the figure. As an additional measure to ensure that the orbit is generally consistent with the horseshoe shape, two conditions are used as a filter. First, the orbit must extend past the $\hat{x}$-coordinate of L_4, as illustrated in Figure 4.2(d). Second, the $\hat{x}$ position of the orbit at the first $\hat{x}$-axis crossing must be less than that of L_4. Using this search and filter method, many potential periodic horseshoe orbits are identified. This scheme for detecting potential horseshoes is implemented in both the Sun-Jupiter and Saturn-Titan systems.

4.1.2 Periodic Horseshoe Orbits

Once a near-periodic, horseshoe-shaped trajectory is identified via the search and filter scheme, it can often be numerically corrected to be precisely periodic. As an example, consider the plot of $\dot{x}_f$ as a function of $\dot{y}_0$ for a nondimensional x_0 value

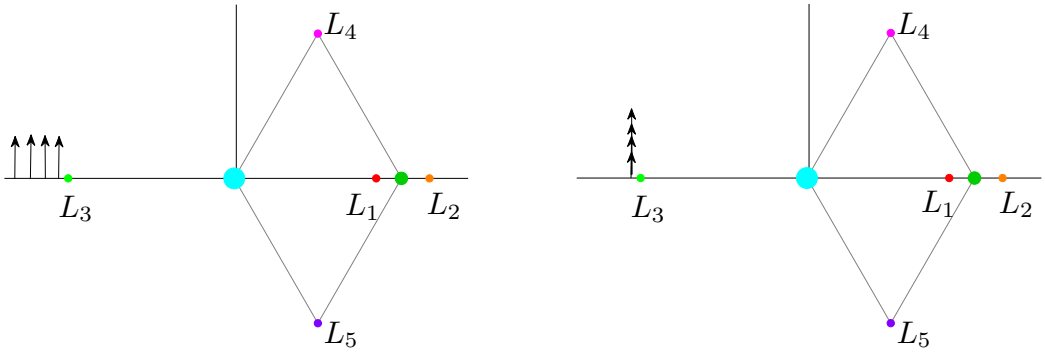

(a) Step 1: Sweep out x_0

(b) Step 2: Sweep out $\dot{y}_0$

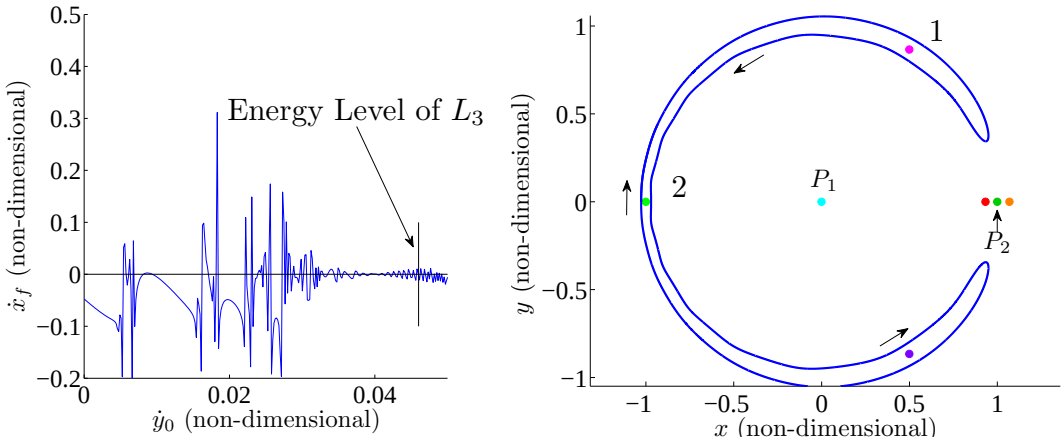

(c) Step 3: Find Perpendicular $\hat{x}$-axis Crossings

(d) Step 4: Filter for Potential Horseshoe Orbits

Figure 4.2. Search and Filter Scheme to Locate Potential Periodic Horseshoe Orbits

of -1.0261 in the Saturn-Titan system that appears in Figure 4.3. The red box in this plot is used to identify an initial condition that will result in a near-periodic horseshoe orbit. The first half of this near-periodic horseshoe orbit is depicted in Figure 4.4. This orbit is corrected to be periodic through the use of multiple shooting techniques. The constraints are similar to those defined for Lyapunov orbits, that is, due to symmetry, there must be two perpendicular $\hat{x}$-axis crossings. Also consistent with Lyapunov orbits, the horseshoe orbits exhibit symmetry across the $\hat{x}$-axis, thus,

only the first half of the periodic horseshoe orbit is generally computed. The second half of the orbit is then determined by simply mirroring the first half of the orbit across the $\hat{x}$-axis. This corrected periodic horseshoe orbit is plotted in Figure 4.5.

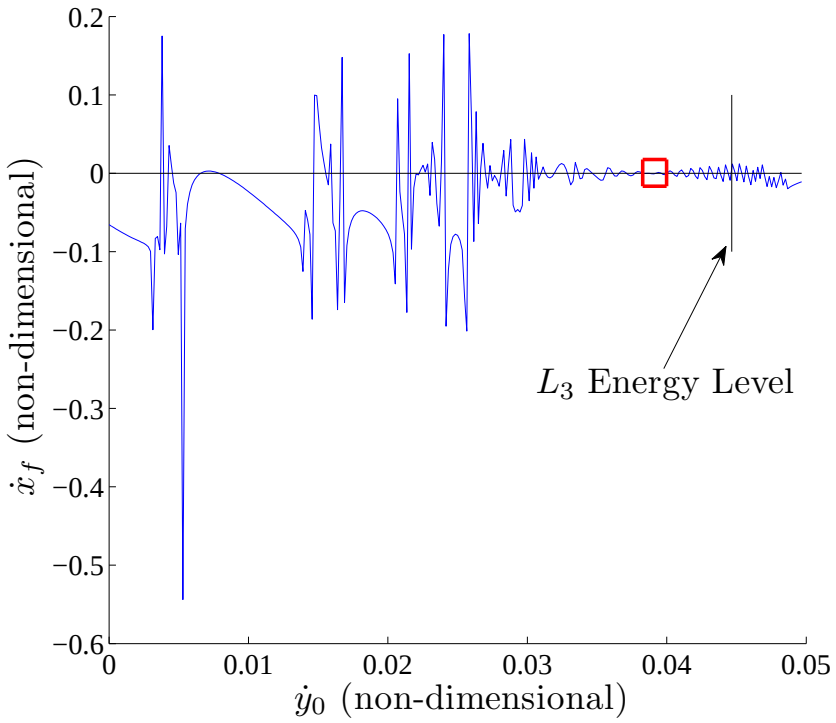

Figure 4.3. Given a Location at $x_0 = -1.0261$ in Saturn-Titan System; Initial Speed $\dot{y}_0$ (Red Box) Likely to Yield Horseshoe Orbit

4.1.3 Families of Periodic Horseshoe Orbits

Computing families of periodic horseshoe orbits is an excellent approach to discover the various forms that exist for horseshoe orbits. Horseshoe orbits tend to evolve in a less intuitive direction than some other periodic trajectories such as Lyapunov orbits; therefore, a suitable method for computing such families is a pseudo-arclength continuation scheme. The evolution of a family of periodic horseshoe orbits in the Saturn-Titan system is plotted in Figure 4.6. Let this family be labeled Family A.

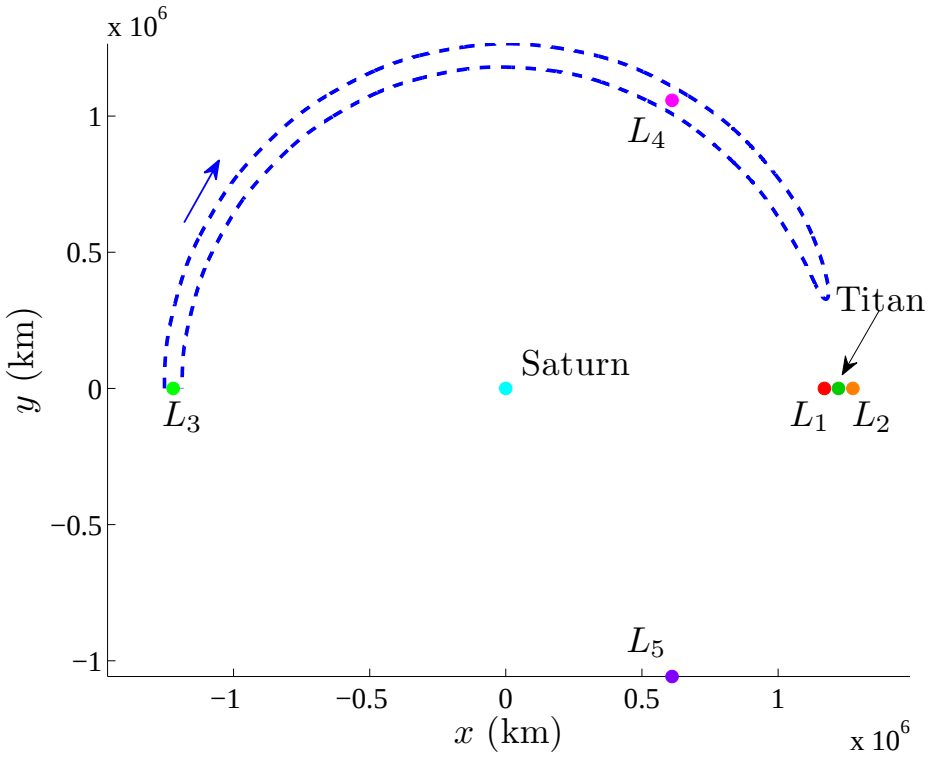

Figure 4.4. Top Half of a Near-Periodic Horseshoe Orbit

Figures 4.6(a)-4.6(d) each include the same subset of 97 computed trajectories (plotted in blue) that are members of the same family. In black, a particular family member is highlighted in each figure to demonstrate the evolution of the family. In Figure 4.6(a), the first member of the family is plotted in black. This initial periodic horseshoe is the same as the original horseshoe orbit first computed in Figure 4.5. In Figure 4.6(b), the 30^{th} family member computed via continuation is highlighted. Notice that between the first computed family member and member 30, little difference in the general characteristics is apparent. The 85^{th} family member is plotted in black in Figure 4.6(c). This particular trajectory reveals that the general shape of this horseshoe orbit family is evolving to incorporate more loops. The final orbit that is computed in this family is apparent in Figure 4.6(d). This orbit possesses the largest, most defined loops of any in the family. From the first simple, smooth

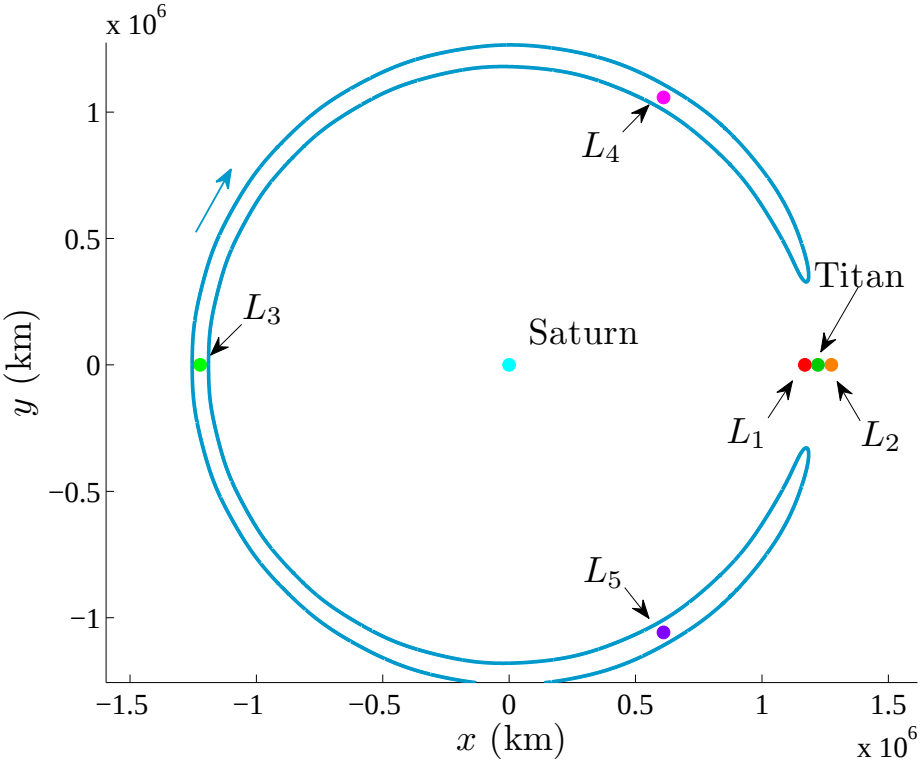

Figure 4.5. Periodic Horseshoe Orbit

horseshoe, it is evident that as the family evolves, the horseshoes are characterized by more and more looping behavior. This looping behavior in the rotating frame signifies additional revolutions about the primary in the inertial frame.

It is possible to compute countless other families of periodic horseshoe orbits. Another example of a family of periodic horseshoe orbits in the Saturn-Titan system, labeled Family B, appears in Figure 4.7. This family is characterized by the same general type of increasing complexity as the family evolves. Notice that this particular Family B in Figure 4.7 evolves slightly differently than Family A in Figure 4.6. The first orbit computed for this new family is not a smooth horseshoe that is apparent as the generating orbit in the previous Saturn-Titan horseshoe Family A. Additionally, although the initial condition for this family is on the left side of L_3, as the family evolves, the initial condition corresponding to the next individual member shifts to

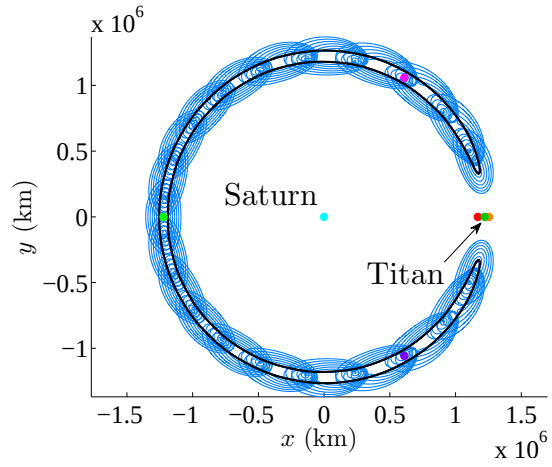

(a) Computed Orbit #1 Highlighted

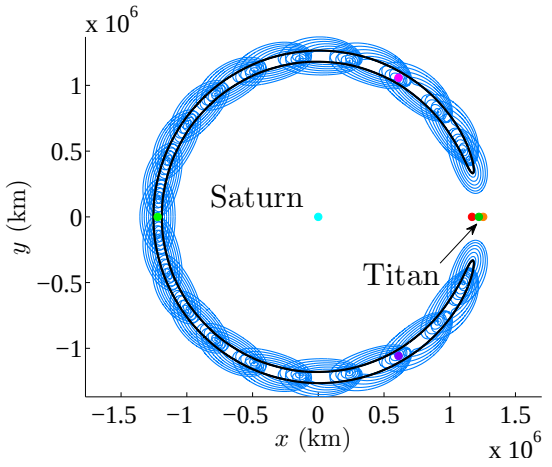

(b) Computed Orbit #30 Highlighted

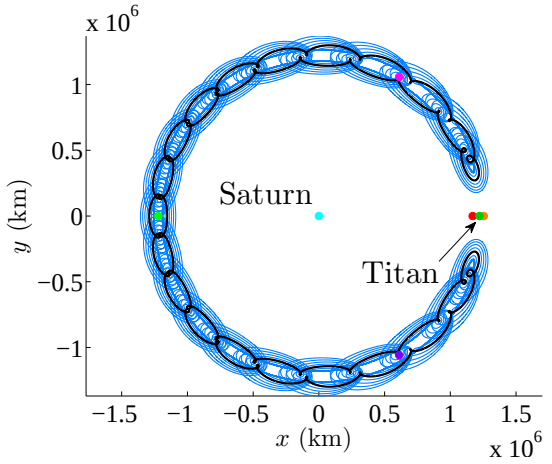

(c) Computed Orbit #85 Highlighted

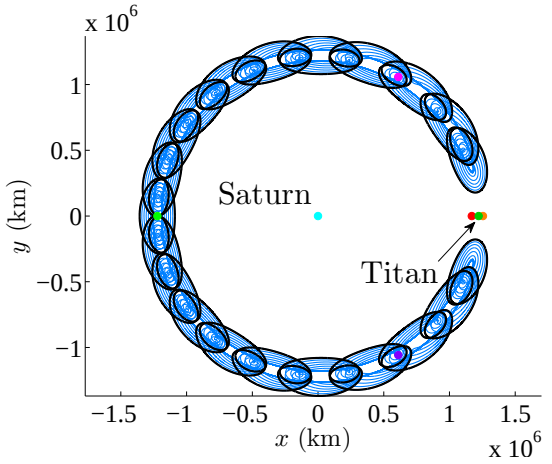

(d) Computed Orbit #97 Highlighted

Figure 4.6. Family A: Periodic Horseshoe Orbits in the Saturn-Titan System

the right of L_3 and, as a consequence, possesses an initial velocity such that $\dot{y}_0$ is negative. Thus, the computed trajectories in the family terminate with the orbit in Figure 4.7(d). Although the search and filter method does not explicitly seek initial conditions of this form, the numerical processes to correct periodic orbits and compute families allows the initial conditions to evolve in a wide variety of different directions. A third family of periodic horseshoe orbits, labeled Family C, is plotted in Figure 4.8;

this set of trajectories is computed in the Sun-Jupiter system, however. Similar to the first Saturn-Titan Family A in Figure 4.6, the first computed member of the Sun-Jupiter Family C is smooth, and as the family evolves, larger and larger loops emerge in each horseshoe trajectory. Note that in this investigation, only subsets of entire horseshoe families are computed, and no attempt is made to mathematically discover the origin or natural termination of the families.

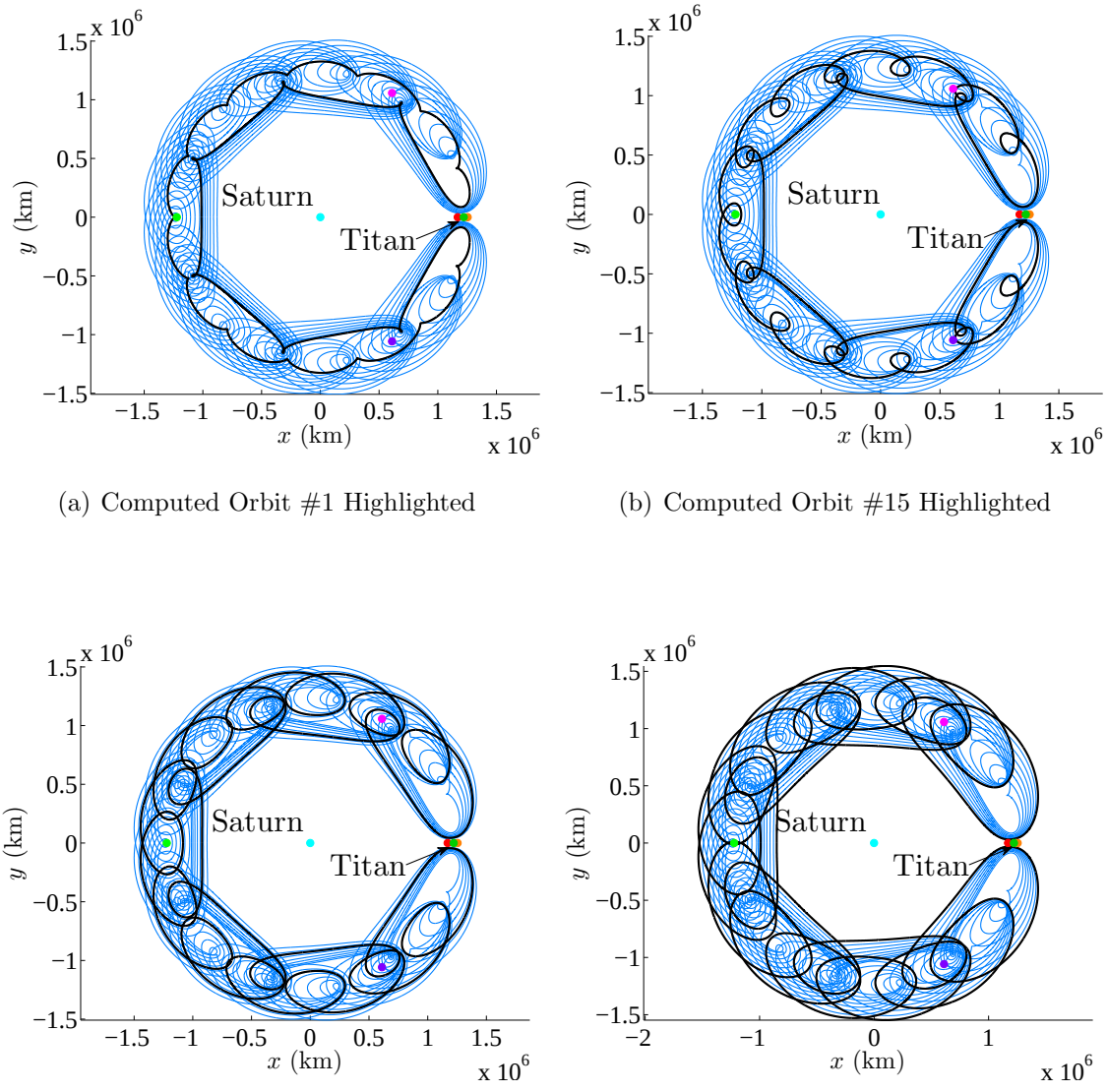

(a) Computed Orbit #1 Highlighted

(b) Computed Orbit #15 Highlighted

(c) Computed Orbit #33 Highlighted

(d) Computed Orbit #49 Highlighted

Figure 4.7. Family B: Periodic Horseshoe Orbits in the Saturn-Titan System

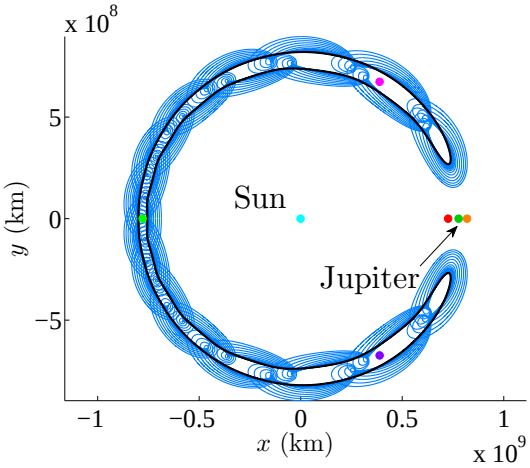

(a) Computed Orbit #1 Highlighted

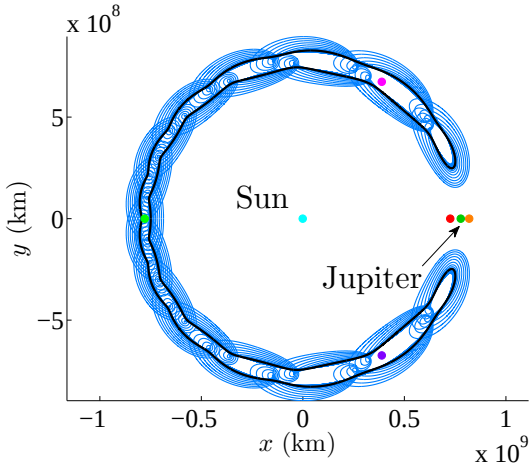

(b) Computed Orbit #90 Highlighted

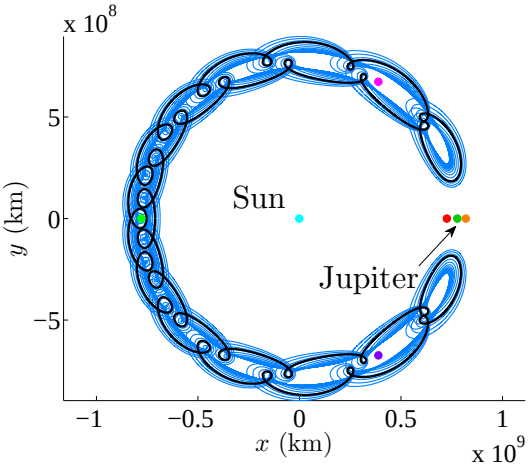

(c) Computed Orbit #110 Highlighted

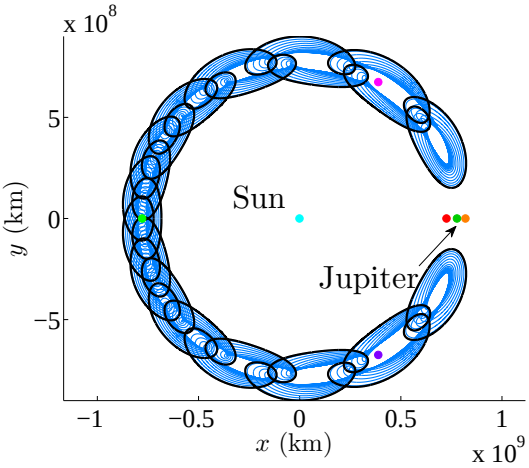

(d) Computed Orbit #119 Highlighted

Figure 4.8. Family C: Periodic Horseshoe Orbits in the Sun-Jupiter System

To explore the characteristics of the families of periodic horseshoe orbits, several orbital characteristics are investigated. Specifically, the period and Jacobi constant along each family is evaluated. As a reference for comparison, refer to Table 4.1 for information about the periods and the reference Jacobi constants associated with the two systems of interest. Plots of the orbital period along each of the three families of horseshoe orbits appear in Figure 4.9. Figure 4.9(a) reveals that the periods of the orbits in Family A are much larger than the period of a single revolution of Titan about Saturn (approximately 16 days). As the family evolves, and larger loops appear, the period increases. The periods of the members of Family B in Figure 4.9(b) decrease, however, as the complexity of the path increases. Also notable, the periods in this family are significantly shorter than the periods in Family A. Figure 4.9(c) reveals that the orbital periods in Family C are quite long, even when compared to the period of Jupiter around the Sun (approximately 12 years). Similar to Family B, the period in the Sun-Jupiter family decreases as the family develops. In Figure 4.10, the Jacobi constant along each of the three families is plotted in magenta. For comparison, the Jacobi constant values corresponding to L_3 and L_4/L_5 are indicated on the plots. All three of the families exhibit similar behavior in Jacobi constant. The value of Jacobi constant corresponding to the first orbit computed in all three families is greater than that of L_3. As the families evolve, the Jacobi constants decrease and fall below that of L_4, L_5. The orbits continue to gain energy as the family develops. Observe that the plots of period and Jacobi constant have inflection points in the curves representing all three of the families. At the orbit indices corresponding to these points, a change in the appearance of the horseshoes is observed. In Family A, the orbits transition from being smooth to "wavy" at this point, and eventually develop loops. The inflection point in the plots for Family B occurs when the initial condition for the horseshoe orbit switches from the left of L_3 to the right of L_3. This same switch also corresponds to the inflection in the period and Jacobi constant plots for Family C.

Notice that the general shape of the horseshoe orbits frequently resemble a ZVC. To illustrate, the first orbit in Family B is plotted in Figure 4.11 along with the ZVC

that corresponds to the same value of Jacobi constant. The horseshoe orbit, plotted in blue, "hugs" the ZVC boundary. This is typical behavior for horseshoe orbits with a Jacobi constant value between that of L_2 and L_3. Once the value of Jacobi constant falls below that of L_3, as in orbit six of Family B plotted with the corresponding ZVCs in Figure 4.12, the horseshoe orbits are no longer as restricted by the ZVC, and the loops may expand (though it is not apparent in this example). Once Jacobi constants falls below a value of $JC_{L_{4,5}}$, the ZVC no longer exists in the plane of motion, and does not constrain the motion of the horseshoe orbit. This is illustrated by the plot of orbit 30 in Family B in Figure 4.13.

Table 4.1 Period and Jacobi Constants Associated with Systems of Interest

System	2-Body Period (years)	JC_{L_1}	JC_{L_2}	JC_{L_3}	JC_{L_4,L_5}
Saturn-Titan	0.0437	3.0158	3.0155	3.0002	2.9998
Sun-Jupiter	11.8720	3.0388	3.0375	3.0010	2.9990

4.2 The Stability of Horseshoe Orbits

Investigating the stability of the periodic horseshoe orbits is an important precursor to developing transfer trajectories. To evaluate the stability of the various members of the three horseshoe families, the eigenvalues associated with each horseshoe are computed numerically. The method for evaluating the eigenvalues is presented in Section 3.7. Essentially, the monodromy matrix is determined for each periodic horseshoe orbit, and the eigenvalues are computed. If there is an eigenvalue pair corresponding to the unstable/stable subspace, that is, if there exists a $|\lambda_i| > 1$ and $|\lambda_j| < 1$, then the orbit is considered unstable. An unstable orbit yields unstable and stable invariant manifolds that can offer significant insight into the natural trajectories that approach and depart the periodic orbit. Note that in some of the horseshoe

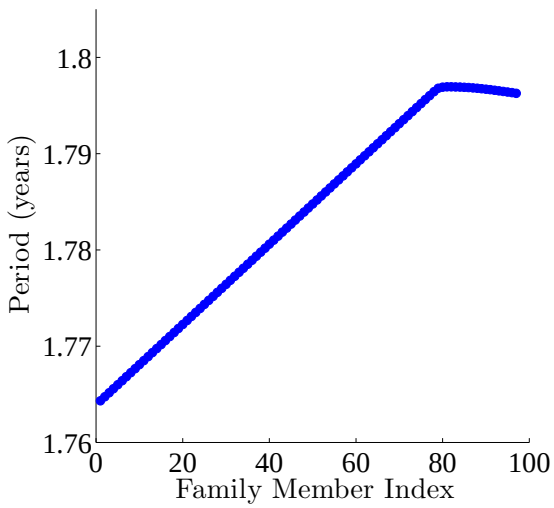

(a) Period Along Family A

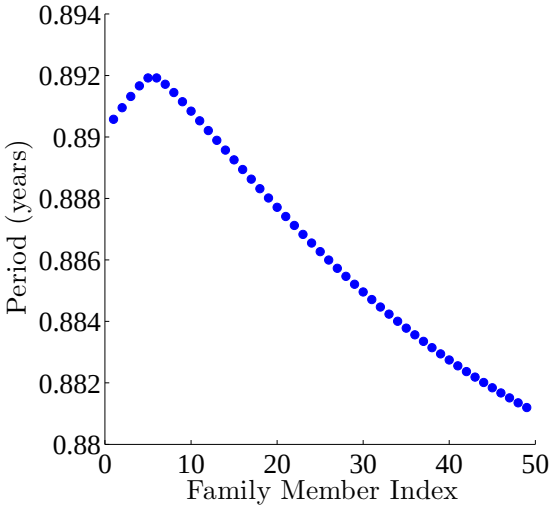

(b) Period Along Family B

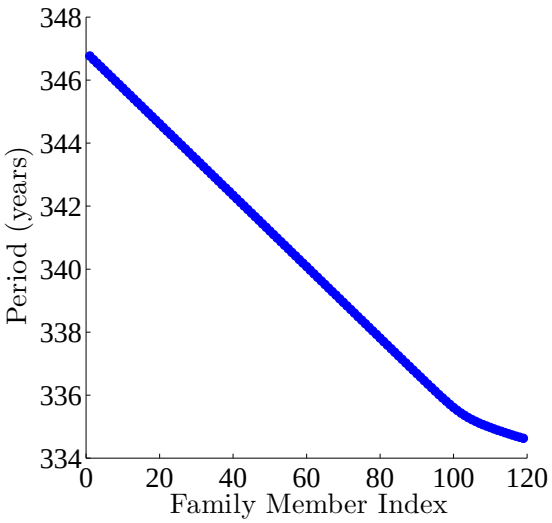

(c) Period Along Family C

Figure 4.9. Orbital Periods of Horseshoes as Three Families Evolve

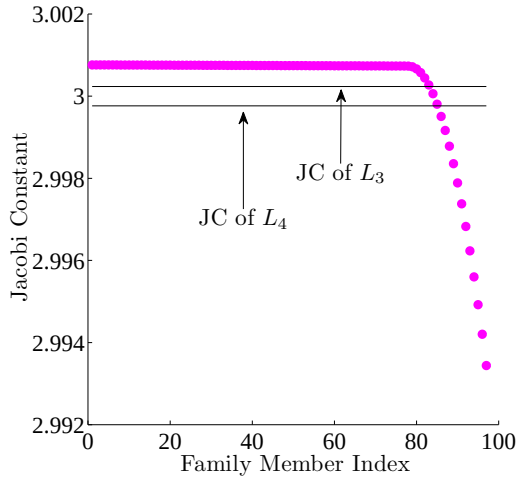

(a) Jacobi Constant Along Family A

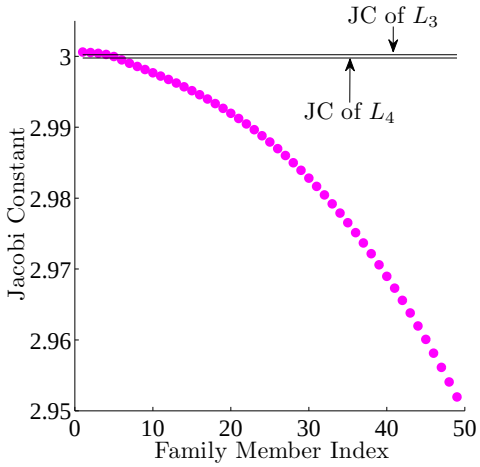

(b) Jacobi Constant Along Family B

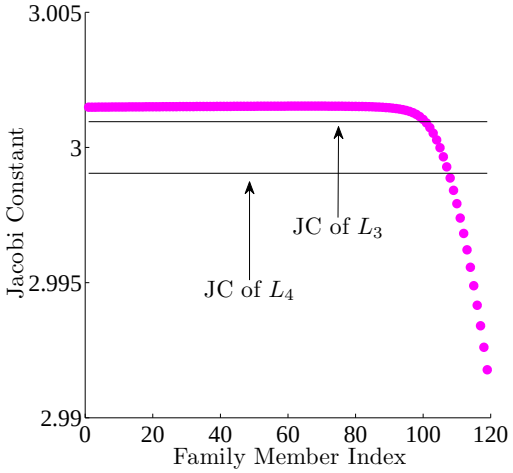

(c) Jacobi Constant Along Family C

Figure 4.10. Jacobi Constant along the Three Families of Horseshoes Orbits

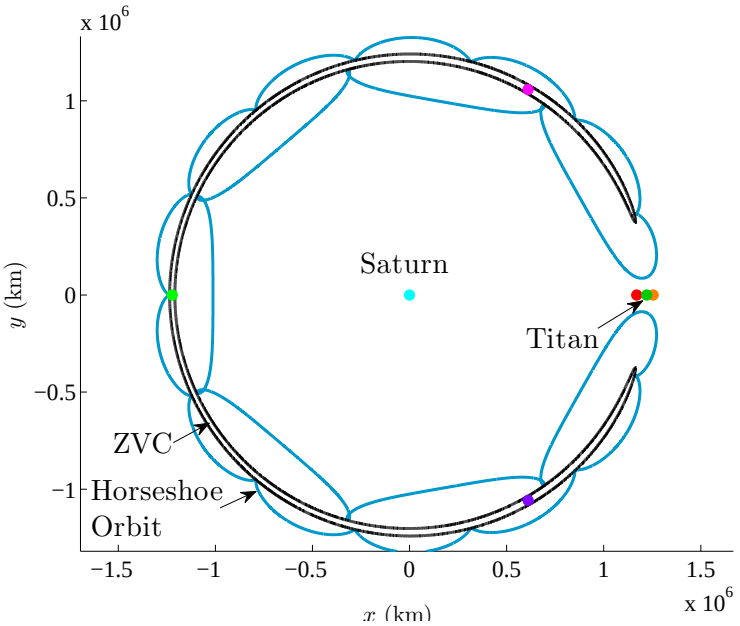

Figure 4.11. Sample Horseshoe Orbit (Family B, Orbit # 1) Plotted with Associated ZVC

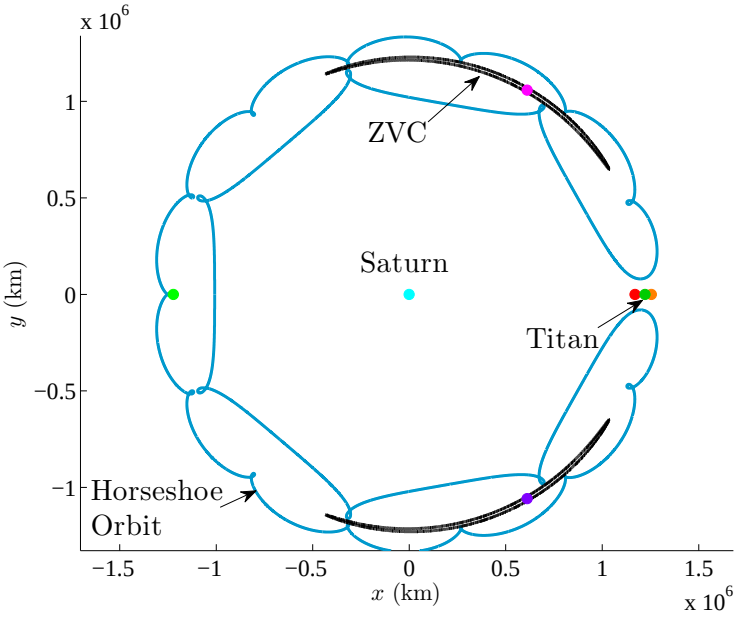

Figure 4.12. Sample Horseshoe Orbit (Family B, Orbit # 6) Plotted with Associated ZVC

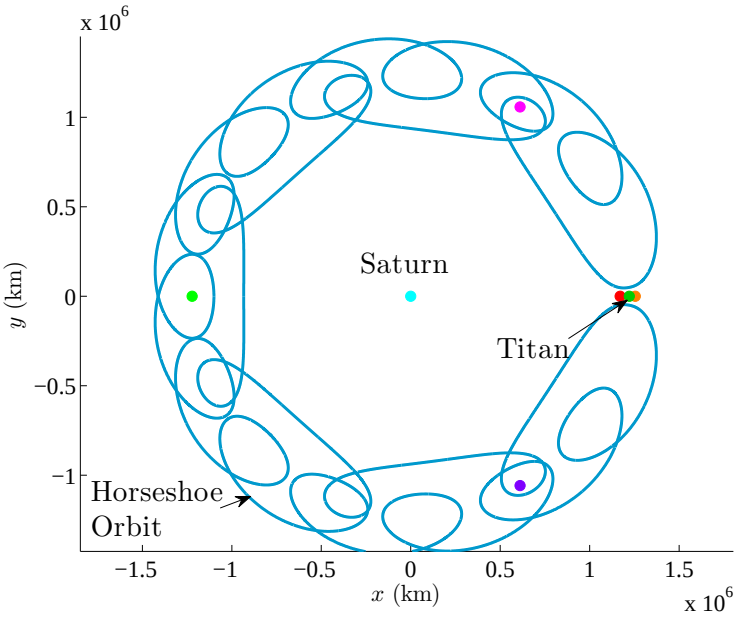

Figure 4.13. Sample Horseshoe Orbit (Family B, Orbit # 30); ZVS No Longer Intersects the $\hat{x}$-$\hat{y}$ Plane

trajectories, there are instances where there are two pairs of unstable/stable eigenvalues. In these cases, the "most unstable/stable" pair is selected for computation of invariant manifolds. In Figure 4.14, the unstable eigenvalue across the three horseshoe families is plotted. In these figures, the most unstable eigenvalue is plotted in terms of the family member index. In Figure 4.14(a), note that the index that identifies member orbits along the family begins at 80. The previous members computed in this family as the family evolves from the generating orbit do not possess an unstable eigenvalue and, therefore, are linearly stable. It is clear that, as the family evolves and is characterized by larger loops, the unstable eigenvalue continues to increase in size. A similar eigenvalue plot for the second Saturn-Titan horseshoe Family B appears in Figure 4.14(b). The eigenvalues are unstable throughout the family. Notice that the magnitude of the unstable eigenvalues is generally much greater in Figure 4.14(b) than those from the Family A in Figure 4.14(a). The unstable eigenvalues for the orbits in the Sun-Jupiter family C are plotted in Figure 4.14(c). With the exception

of the first member of the family, which is only slightly unstable, the members of this family are linearly stable until approximately the 67^{th} member, when the eigenvalue begins to steadily increase. The magnitude of the unstable eigenvalues corresponding to this Sun-Jupiter family is between the values from horseshoe Families A and B in the Saturn-Titan system.

4.3 Frequencies and Resonances in Horseshoe Orbits

The appearance of the loops in the horseshoe orbits when viewed in the rotating frame leads to the investigation of orbital frequencies associated with the orbit and, therefore, also possible resonances within the horseshoe. To study the frequencies within a horseshoe orbit, it is useful to consider the motion in an inertial frame. In the time required to complete one horseshoe orbit in the rotating frame, many revolutions about the primary are completed in the inertial frame. A loop in the orbit in the rotating frame indicates a revolution about P_1 in the inertial frame. To illustrate, Figure 4.15 includes two different views of the first horseshoe orbit in Family B; the orbit is plotted in both the rotating and inertial frames. The plot of the horseshoe in the rotating frame in Figure 4.15(a) includes a single color from inertial periapsis to inertial periapsis. Thus, for one particular arc, i.e., one colored segment, one revolution about the Saturn has been completed in the inertial frame. In the inertial view in Figure 4.15(b), the path that is comprised of just one period of the horseshoe actually includes many revolutions about Saturn in an inertial frame. For reference, the orbit of Titan about Saturn is plotted in green. Notice that the inertial path of the horseshoe orbit, plotted in orange, is generally outside the orbit of Titan for a portion of the path, and generally inside the orbit of Titan on another segment of the path. The revolutions that are closer to Saturn correspond to the inner segments of the horseshoe in the rotating frame, while the revolutions of the inertial path that are farther from Saturn correspond to the outer segments of the horseshoe. To illustrate the frequencies, the period of each inertial revolution is plotted in Figure 4.16 versus

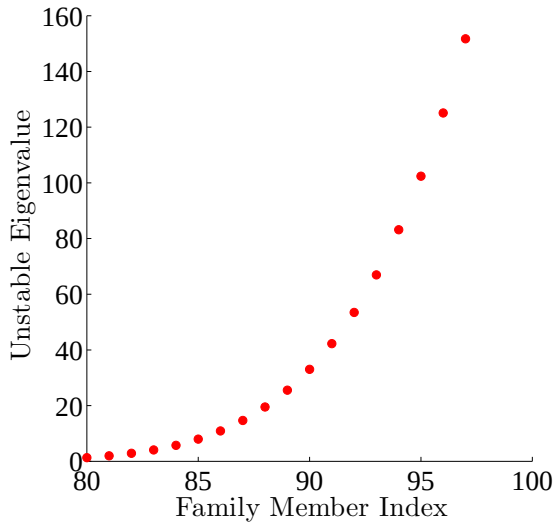

(a) Unstable Eigenvalue Along Family A

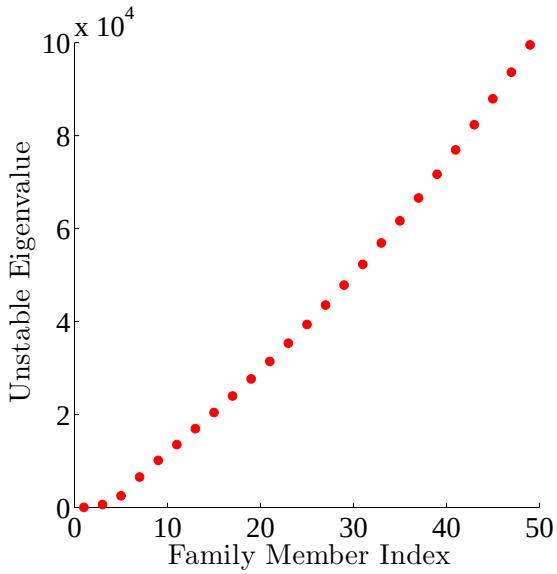

(b) Unstable Eigenvalue Along Family B

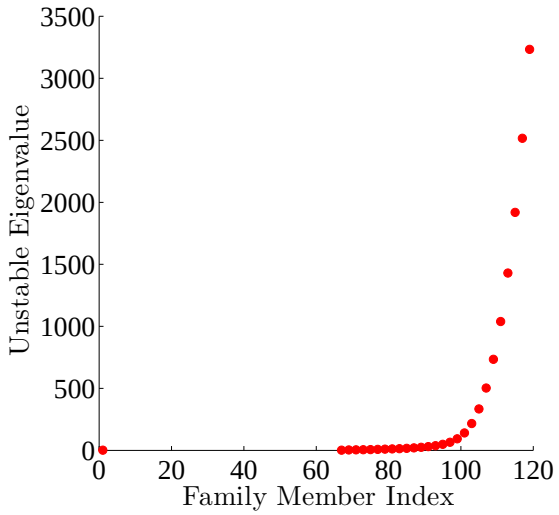

(c) Unstable Eigenvalue Along Family C

Figure 4.14. Unstable Eigenvalues of Individual Horseshoe Orbits Along Three Families

the revolution index. Revolution index number one corresponds to the revolution that originates with the initial condition of the horseshoe orbit on the $\hat{x}$ axis and ends with the next periapsis. The final revolution completes the horseshoe. It is clear from this figure that, in general, there are multiple frequencies involved in a horseshoe orbit, each corresponding to the different types of loops apparent in the rotating view of the horseshoe orbit. In this example, the period along each inertial revolution is longer along the outside of the horseshoe orbit than the period along the inner segments of the horseshoe, which corresponds to revolutions eight through thirteen in Figure 4.16.

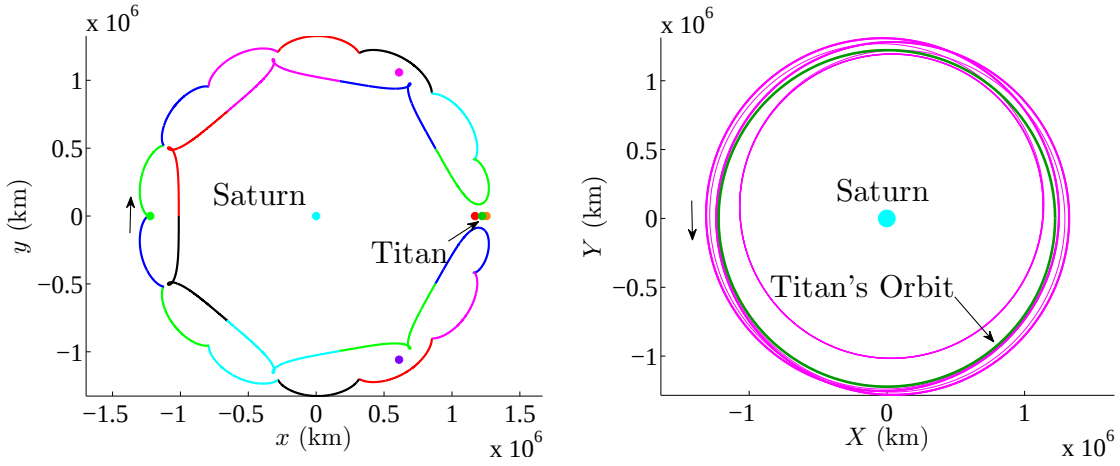

(a) Rotating View

(b) Inertial View

Figure 4.15. Rotating and Inertial Views of a Horseshoe Orbit in the Saturn-Titan System

This information regarding frequencies within horseshoe orbits suggests a potential resonance. A resonance generally refers to a dynamical phenomenon that arises "when there is a simple numerical relationship between frequencies or periods" [43]. Although many types of resonances are possible, these frequencies represent orbit-orbit coupling, where the orbital periods of two bodies are involved [43]. In an investigation of resonant orbits in the CR3BP, Vaquero [44] details a method for determining an orbit-orbit resonance ratio. This type of resonance is described by a $p : q$ ratio of periods, in which p represents the period of body B and q denotes the pe-

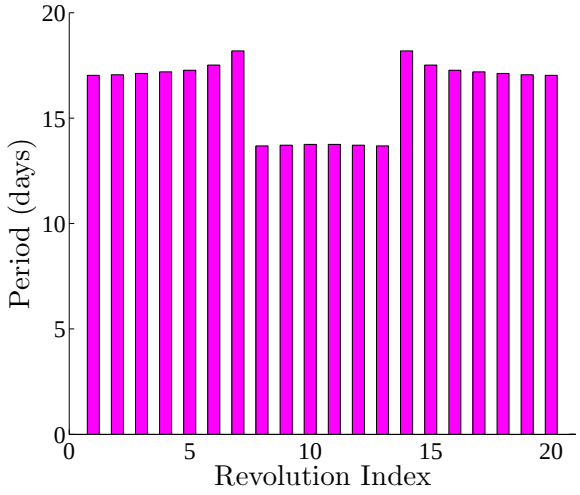

Figure 4.16. Frequencies Within a Horseshoe Orbit

riod of another body A. This ratio is not necessarily precisely rational in the CR3BP because of the additional gravity effects, but it is approximately correct. For application to horseshoe orbits, let body A be a massless body traveling along a horseshoe orbit, and let body B be P_2 in the system of interest. For example, if there exists a spacecraft (particle P_3) moving along a horseshoe orbit in a $2:1$ resonance with Titan, then it completes two revolutions about Saturn in the same interval required by Titan to complete one revolution about Saturn.

To determine if any of the computed horseshoes are in resonance, then, this $p:q$ ratio is evaluated. The number of revolutions the horseshoe orbit completes about the primary, that is p, is determined from the inertial periapses. For horseshoe orbits with loops, this also corresponds to the number of loops along the path. A simple calculation determines q, the number of times body B travels about the primary in that same interval of time. The relationship $q = T/2\pi$, where T is the non-dimensional period of the horseshoe, yields a value for q. If this value of q is sufficiently close to an integer number, then the horseshoe orbit is deemed resonant with body B. Most of the computed horseshoe trajectories are not exactly resonant, but in loose terms,

many are close. A summary of the approximate resonances from a subset of the computed horseshoe orbits is listed in Table 4.2

Table 4.2 Approximate Resonances of Several Horseshoe Orbits

Horseshoe Family	Orbit Index	p	q	$p:q$ Ratio
Family A	1	32	40.39	32:40
Family A	97	42	41.12	42:41
Family B	1	20	20.39	20:20
Family B	49	20	20.17	20:20
Family C	1	16	29.21	16:29
Family C	119	28	28.19	28:28

4.4 Invariant Manifolds Associated with Horseshoe Orbits

As a first step in considering possible transfer trajectories, an investigation of invariant manifolds associated with horseshoe orbits is useful. Because the stable and unstable manifolds represent the natural flow into and out of an orbit, manifolds supply a convenient first guess for a cost-free transfer to or from the orbit. Recall that the method for computing invariant manifolds is discussed in Section 3.8. To numerically approximate a state on a stable or unstable manifold associated with a periodic horseshoe orbit, the orbit must possess an unstable/stable eigenvalue pair. In the discussion of horseshoe orbit stability, it is noted that not every horseshoe is characterized by eigenvalues of this form, and are therefore linearly stable. Such orbits, then, are not employed in the computation of invariant manifolds. Since a relatively low-valued unstable/stable eigenvalue implies a longer time to wind off or to wind onto a periodic orbit, from experience it is apparent that an unstable eigenvalue of magnitude on the order of 1×10^3 is most useful. An eigenvalue of this

magnitude is low enough that the flow does not immediately depart the orbit, yet also of a size that is sufficient for the flow to depart the orbit reasonable quickly. Since the horseshoe orbits in Family A do not reach this level of instability, as is apparent in Section 4.2, invariant manifolds are not employed for this family. The remaining two horseshoe families do include members with the desired level of stability.

Invariant manifolds are computed for selected periodic horseshoe orbits from both Family B and Family C. Several orbital characteristics corresponding to these particular orbits, including the value of their unstable eigenvalues, are summarized in Table 4.3. To compute the invariant manifolds, a suitable offset value, d, is determined for each orbit, and each orbit is discretized into 50 fixed points. The invariant manifolds in Figure 4.17 reflect the arrival toward and departure from the 5^{th} orbit in the Saturn-Titan Family B of horseshoe orbits. The trajectories that comprise the invariant manifolds are propagated for two years for each fixed point along the orbit. The stable manifold asymptotically approaching the horseshoe is plotted in magenta, while the unstable manifold is plotted in green. The horseshoe orbit itself is blue. Although it is unclear from the figure, the stable manifold requires a long "wind off" time when the path follows the general shape of the horseshoe before beginning to depart. The unstable manifold approaches from afar and then follows the path of the horseshoe consistent with an asymptotic approach. A similar plot appears in Figure 4.18 for the 115^{th} orbit in the Sun-Jupiter Family C of horseshoe orbits. Again, the orbit is discretized into 50 fixed points, and the manifolds are propagated for 700 years. These manifolds exhibit the same general shape and characteristics as those for the Saturn-Titan manifolds. It is clear from both figures that the invariant manifolds are very complex and yield little visual insight due to the overlapping paths. A solution to this visualization challenge is addressed in the following chapter.

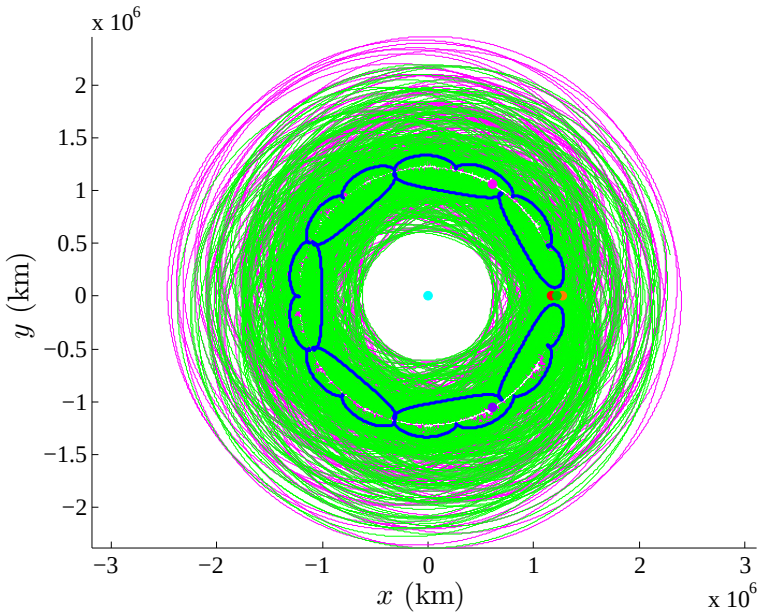

Figure 4.17. Unstable (Green) and Stable (Magenta) Invariant Manifolds Associated with a Horseshoe Orbit in the Saturn-Titan System

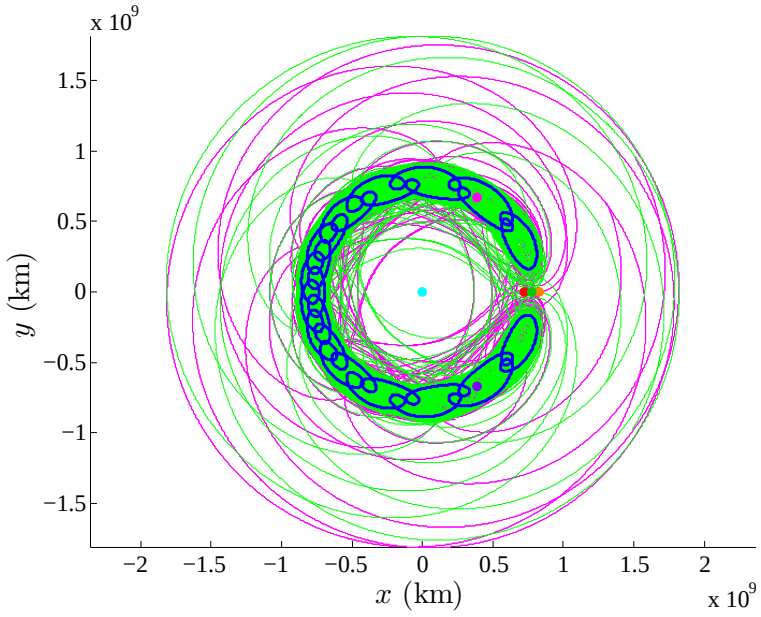

Figure 4.18. Unstable (Green) and Stable (Magenta) Invariant Manifolds Associatied with a Horseshoe Orbit in the Sun-Jupiter System

Table 4.3 Characteristics of Orbits Selected for Invariant Manifold Computation

Horseshoe Family	Orbit Index	Unstable λ	Period (years)	JC
Family B	5	2522.6	0.8919	3.0000
Family C	115	1918.7	334.77	2.9949

5. COMPUTATION OF TRANSFERS TO PERIODIC HORSESHOE ORBITS

Once the method for computing horseshoe orbits is established, the primary task, that is, investigating transfers to horseshoe orbits is initiated. The specific goal is a preliminary analysis of Δv costs that are required to enter into a horseshoe orbit from a libration point orbit. Several approaches to discover transfers are investigated, each with a different balance between transfer cost and transfer time. A Hohmann transfer approximation is initially constructed originating from a Lyapunov orbit and delivering a vehicle into a horseshoe orbit in the CR3BP as a preliminary estimate of transfer costs. Then, an instantaneous single-impulse transfer between a libration point orbit and a horseshoe orbit that intersect in position space is investigated. Transfers are then computed using the unstable manifold associated with a Lyapunov orbit that intersects a horseshoe orbit. Finally, a more sophisticated method of locating transfers using Poincaré maps to identify an intersection of Lyapunov unstable manifolds and horseshoe stable manifolds is developed.

5.1 Preliminary Analysis: Approximation of a Hohmann Transfer From a Lyapunov Orbit to a Horseshoe Orbit in the Inertial Frame

The Hohmann transfer orbit, first described by Walter Hohmann in 1925 [45], is a classical method for computing transfers between two circular, planar, orbits in a two-body problem. The Hohmann transfer is comprised of two impulsive maneuvers used to connect two coplanar circular orbits via a transfer ellipse. The equations required to compute a Hohmann transfer are summarized, then applied to approximate a transfer to a horseshoe orbit in the CR3BP.

5.1.1 Hohmann Transfer

The concept that is fundamental to a Hohmann transfer is represented in Figure 5.1. To construct a circle-to-circle planar Hohmann transfer, the velocity on both the initial and final circular orbits, plotted in blue and red, respectively, is computed using the familiar two-body equation for circular velocity [46]

$$v_c = \sqrt{\frac{GM}{r}} \tag{5.1}$$

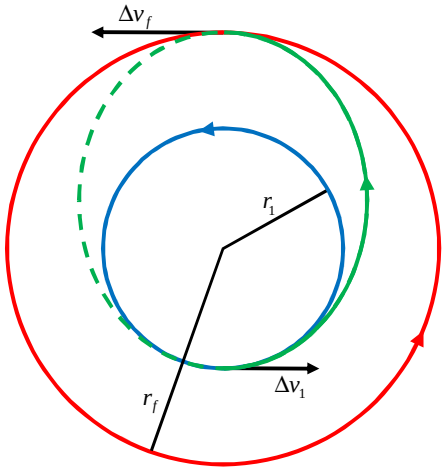

Figure 5.1. Sketch of Hohmann Transfer in a Two-Body Problem

where GM is the product of the gravitational constant, G, and the mass of the primary body in the problem, M. The transfer ellipse is oriented such that the first impulsive maneuver is located at perigee on the ellipse, and the final impulsive maneuver is implemented at apogee. The velocity at perigee on the transfer ellipse, denoted v_1, is given by

$$v_1^2 = GM\left[\frac{2}{r_1} - \frac{2}{r_1 + r_f}\right] \tag{5.2}$$

where r_1 and r_f are the radii of the initial and final circular orbits, respectively [46]. The velocity on the transfer ellipse at apogee, denoted v_f, is calculated using

$$v_f^2 = GM\left[\frac{2}{r_f} - \frac{2}{r_1 + r_f}\right] \tag{5.3}$$

The first impulsive maneuver, Δv_1, is simply a tangential burn applied on the initial circular orbit with magnitude given by

$$\Delta v_1 = v_1 - v_{c_1} \tag{5.4}$$

where v_{c_1} is the velocity the circular orbit. The final maneuver is a tangential burn at apogee on the transfer ellipse with magnitude

$$\Delta v_f = v_{c_f} - v_f \tag{5.5}$$

where v_{c_f} is the velocity on the final circular orbit. The total cost of the Hohmann transfer is, then, $\Delta v_T = \Delta v_1 + \Delta v_f$. The TOF for the Hohmann transfer is computed by

$$\text{TOF}_{\text{Hohmann}} = \pi\sqrt{\frac{\left[1/2\left(r_1 + r_f\right)\right]^3}{GM}} \tag{5.6}$$

which is equal to half of the period of the transfer ellipse [46].

5.1.2 Hohmann Transfer Approxmation From a Lyapunov Orbit to a Horseshoe Orbit in the Saturn-Titan System

Although the Hohmann transfer is constructed in a two-body system, an approximation from a Hohmann transfer is used to estimate the initial and final states to construct a transfer in the Saturn-Titan three-body system. The transfer of interest originates from an L_1 Lyapunov and terminates at a horseshoe orbit, both with the same Jacobi constant. When viewed in the inertial frame, as is apparent in Figure 5.2(a), the orbits both appear near-circular. The Lyapunov is plotted in purple and is initiated from the black point marked on the right side of Saturn. The horseshoe orbit is plotted in blue. Because of its initial conditions, the horseshoe orbit is

defined from the initial black point marked on the left side of Saturn. Note that one period of the Lyapunov is plotted, however it does not complete a full revolution about Saturn. In contrast, one period of the horseshoe is comprised of several revolutions about Saturn. A Hohmann transfer approximation is computed by first identifying a location on the inertial Lyapunov orbit where the velocity is almost entirely in the positive X direction, marked by the lower red asterisk. A point on the inertial horseshoe is then isolated such that the inertial velocity is almost entirely in the negative X direction, identified by the upper red asterisk. Using these locations, the "Hohmann" transfer ellipse is determined, and its velocity at perigee and apogee are computed with Eqns. (5.2)-(5.3). Then, Eqns. (5.4)-(5.6) produce an approximate transfer cost and TOF. These values are listed in Table 5.1. The locations corresponding to the two maneuvers are also marked in Figure 5.2(b), a plot of the Lyapunov orbit and the horseshoe trajectory in the rotating frame. Using the Δv information computed from the conic analysis as an initial guess, a transfer trajectory between the two identified points is computed with a simple fixed-time multiple shooting position targeter in the CR3BP. The transfer time is constrained since the initial and final locations on the transfer arc are specified. The numerically corrected transfer is plotted in the inertial and rotating frames in Figure 5.3. The Δv values and TOF for the corrected transfer differ significantly from the conic approximation, as listed in Table 5.1. The Δv for the targeted transfer is very large because the converged trajectory does not possess tangential maneuvers. As is apparent in Figure 5.3, the Hohmann TOF that is estimated appears to be too long to serve as an initial guess and produce a reasonable transfer. Since the Lyapunov orbit as well as the horseshoe orbit and the transfer path all exist near the surface of the Hill sphere, multiple gravitational fields significantly influence the motion throughout the transfer.

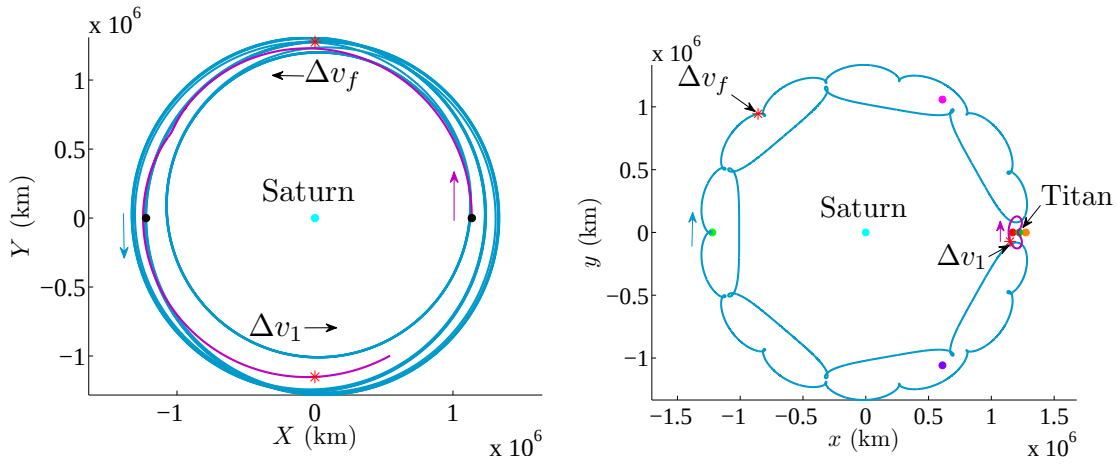

(a) Inertial View (b) Rotating View

Figure 5.2. Orbits Used to Find an Approximation of a Hohmann Transfer Between an L_1 Lyapunov and a Horseshoe in the Saturn-Titan System

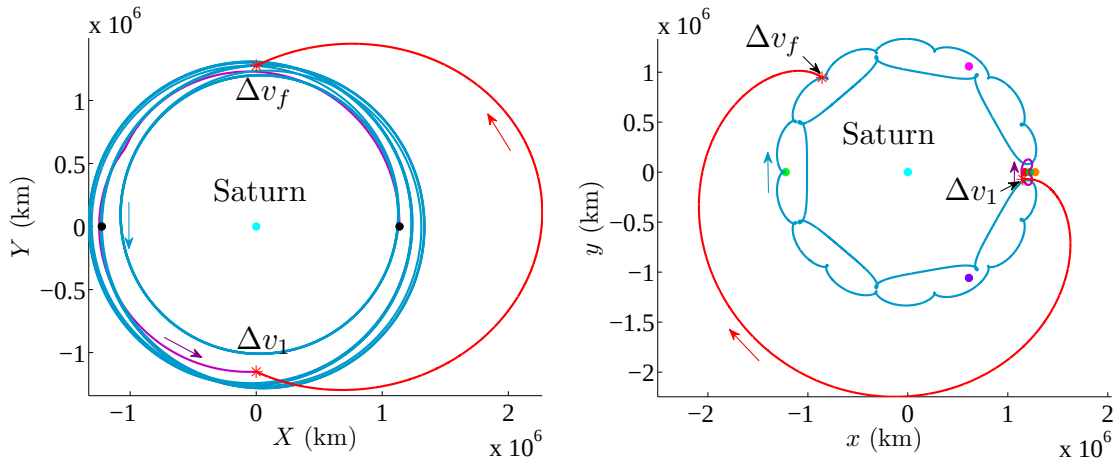

(a) Inertial View (b) Rotating View

Figure 5.3. Targeted Transfer Between an L_1 Lyapunov and a Horseshoe in the Saturn-Titan System

Table 5.1 Approximation of a Hohmann Transfer Between an L_1 Lyapunov and a Horseshoe in the Saturn-Titan System

	$\lvert\Delta v_1\rvert$ (m/s)	$\lvert\Delta v_f\rvert$ (m/s)	$\lvert\Delta v_T\rvert$ (m/s)	TOF (days)
Conic Approx:	277.1353	258.8119	535.9472	7.8937
Targeted:	2645.4519	2384.3367	5029.7886	17.9021

5.1.3 Hohmann Transfer Approxmation From a Lyapunov Orbit to a Horseshoe Orbit in the Sun-Jupiter System

An approximation of a Hohmann transfer is also computed for the Sun-Jupiter system. An L_1 Lyapunov orbit and a horseshoe trajectory are selected such that they possess the same Jacobi constant. Both orbits are plotted in the inertial and rotating frames in Figure 5.4. The procedure is consistent with the Saturn-Titan example and again used to approximate the Hohmann transfer costs. The locations of the two Δv maneuvers are marked on both the inertial and rotating frames in the figure. The costs and TOF for this approximation are listed in Table 5.2. The conic approximation is again employed as an initial guess to compute a converged trajectory in the CR3BP. The resulting trajectory is plotted in the inertial and rotating frames in Figure 5.5. Again, the actual targeted Δv values, listed in Table 5.2, are much higher than predicted by the conic approximation, largely due to the actual non-tangential maneuvers. In this example, the transfer arcs in Figure 5.5 suggest that the approximated TOF is too short. Again, the estimated TOF from a Hohmann transfer approximation is poor. Although another example may offer some insight into the approximation for TOF, alternative approaches to determine an initial guess for a transfer to a horseshoe orbit are explored.

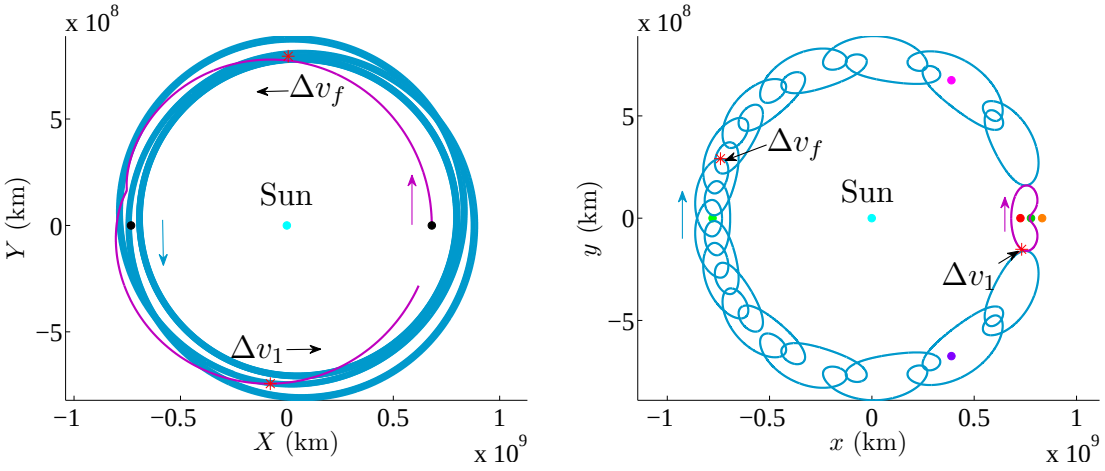

(a) Inertial View (b) Rotating View

Figure 5.4. Orbits Used to Find an Approximation to a Hohmann Transfer Between an L_1 Lyapunov and a Horseshoe in the Sun-Jupiter System

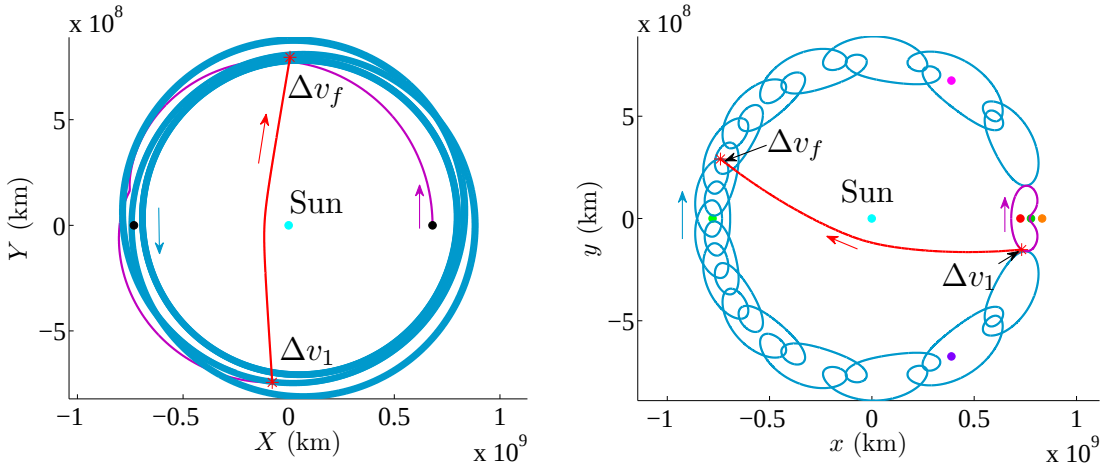

(a) Inertial View (b) Rotating View

Figure 5.5. Targeted Transfer to a Hohmann Transfer Between an L_1 Lyapunov and a Horseshoe in the Sun-Jupiter System

Table 5.2 Approximation of a Hohmann Transfer Between a Lyapunov and Horseshoe in the Sun-Jupiter System

	$\lvert\Delta v_1\rvert$ (m/s)	$\lvert\Delta v_f\rvert$ (m/s)	$\lvert\Delta v_T\rvert$ (m/s)	TOF (years)
Conic Approx:	284.8372	1013.9432	1298.7803	5.8597
Targeted:	96849.7189	98843.3632	195693.0821	0.5025

5.2 Method: Instantaneous Transfers Between Intersecting Orbits

One of the simplest and most fundamental concepts for computing transfers between orbits in the vicinity of libration points and horseshoe orbits involves directly intersecting orbits. To compute the Δv necessary to instantaneously shift from a libration point orbit to the horseshoe trajectory at a point of intersection in position space, the intersection must be computed as accurately as possible. Once an approximate intersection is located, an exact intersection must be ensured. To accomplish the computation of an overlap in position, both the horseshoe and the Lyapunov orbits are propagated from their initial conditions to the same x- or y-position, depending on the coordinate with the faster rate of change, as the approximate intersection point. Then, using the position coordinates along the horseshoe orbit at this end point, and the velocity of the libration point orbit at its end point, a new libration point orbit is targeted. A position targeter is employed such that the libration point orbit is guaranteed to possess the exact same position as a particle on the horseshoe orbit at the same instant in time, to the appropriate level of accuracy. This newly computed libration point orbit is defined by only a slightly different value of Jacobi constant as compared to the original libration point trajectory. Now there exists a horseshoe trajectory and a libration point orbit with a precise intersection, and the Δv is computed simply by evaluating the difference in velocities at the intersection point.

5.2.1 Examples: Libration Point Orbit-to-Horseshoe Transfers in the Saturn-Titan Three-Body System

Countless examples exist of horseshoe orbits and libration point trajectories that intersect in position space. For example, consider the orbits in Figure 5.6. The horseshoe from the Saturn-Titan Family B of periodic horseshoe orbits, and the L_1 Lyapunov are initially selected such that they possess the same value of Jacobi constant, although a common value of Jacobi constant is not a necessary condition. Note that in the corrections process to ensure an exact intersection, the Jacobi constant corresponding to the Lyapunov orbit is very slightly modified. With essentially the same value of Jacobi constant, the velocity discontinuity at the intersection point is due solely to a change in velocity direction. The pair of orbits in Figure 5.6 include four intersections, two of which are examined more closely in Figures 5.7(a) and 5.7(b). Note that the remaining two intersections are characterized by similar values of Δv due to symmetry. Refer to Examples 1 and 2 in Table 5.3 for a list of the Δv values that represent these two intersections.

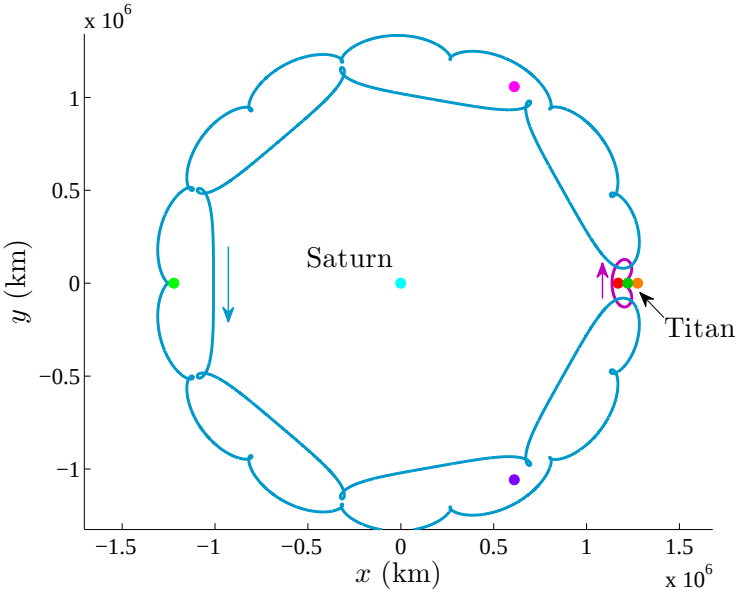

Figure 5.6. Intersecting Horseshoe Orbit and L_1 Lyapunov in the Saturn-Titan System

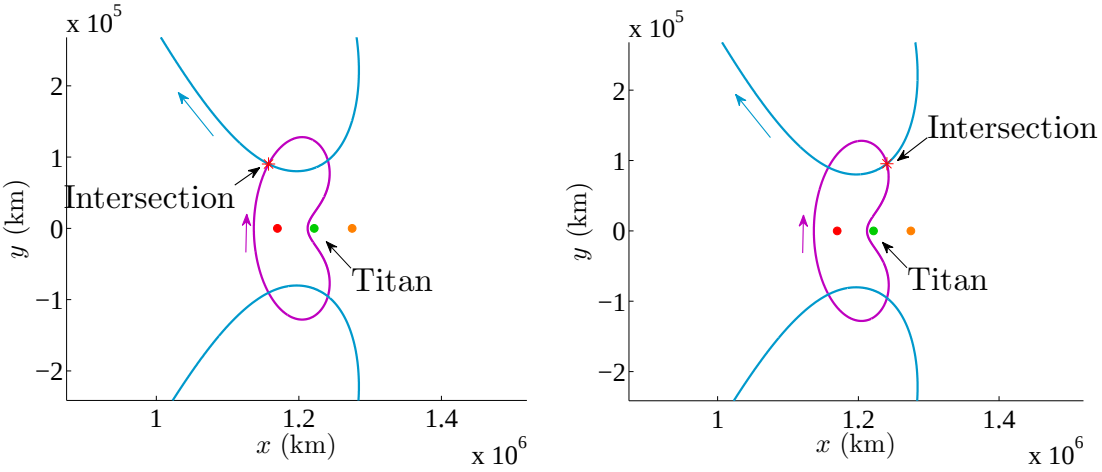

(a) Example 1, Zoom-In

(b) Example 2, Zoom-In

Figure 5.7. Zoom-In of L_1 Lyapunov-to-Horseshoe Intersections in Figure 5.6

Many examples of transfers between intersecting horseshoe orbits and libration point orbits exist, including those in the vicinity of the collinear libration point L_3. To demonstrate the construction of a direct shift between a horseshoe orbit and an L_3 Lyapunov orbit, see Figure 5.8. In this example, the Lyapunov orbit is not selected to ensure the same value of Jacobi constant; instead, it is selected such that the L_3 orbit lies nearly tangent to the horseshoe near the $\hat{x}$-axis. A smooth horseshoe orbit in the Saturn-Titan system is selected for this example. Again, a corrections process ensures a precise intersection. Two of the four possible intersection transfers appear in Figure 5.9. The Δv values corresponding to these intersections, labeled Examples 3 and 4, are listed in Table 5.3.

As a final example of "transfers" designed as direct shifts between intersecting libration point orbits and horseshoe orbits, consider a short-period orbit about L_4 that intersects a smooth horseshoe trajectory. Again, the libration point orbit is selected such that the path is nearly tangent to the horseshoe trajectory, and the path is corrected to produce a precise intersection. The short-period orbit about L_4 and the horseshoe trajectory are plotted in Figure 5.10. All four possible intersections are highlighted in Figure 5.11 since there is a lack of symmetry in the orbit about

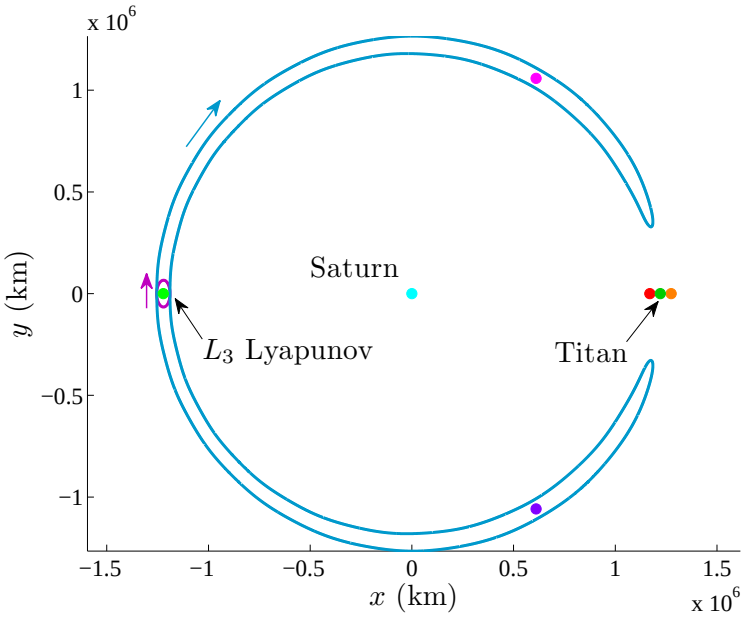

Figure 5.8. Intersecting Horseshoe Orbit and L_3 Lyapunov in the Saturn-Titan System

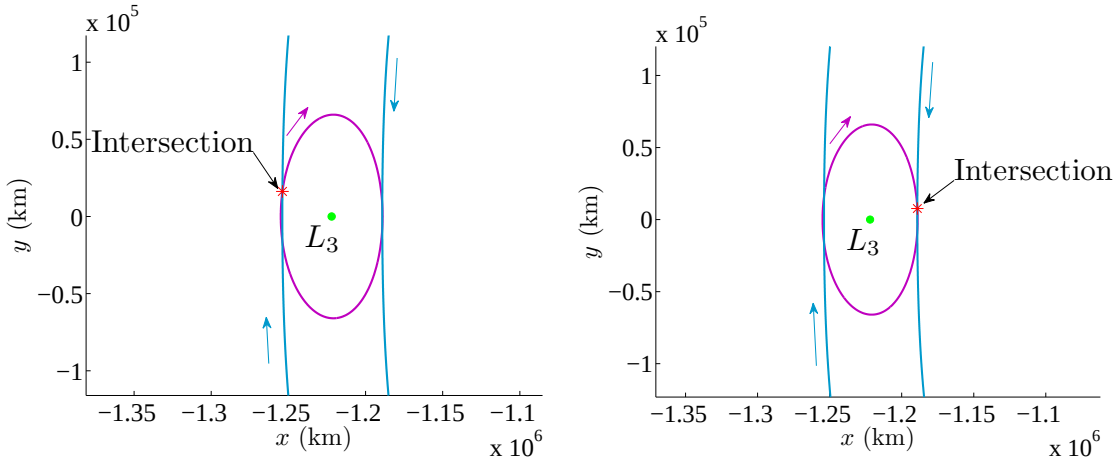

(a) Example 3, Zoom-In

(b) Example 4, Zoom-In

Figure 5.9. Zoom-In of L_3 Lyapunov-to-Horseshoe Intersections in Figure 5.8

L_4. The Δv values corresponding to these single-impulse adjustments are listed in Table 5.3 and identified as Examples 5 through 8.

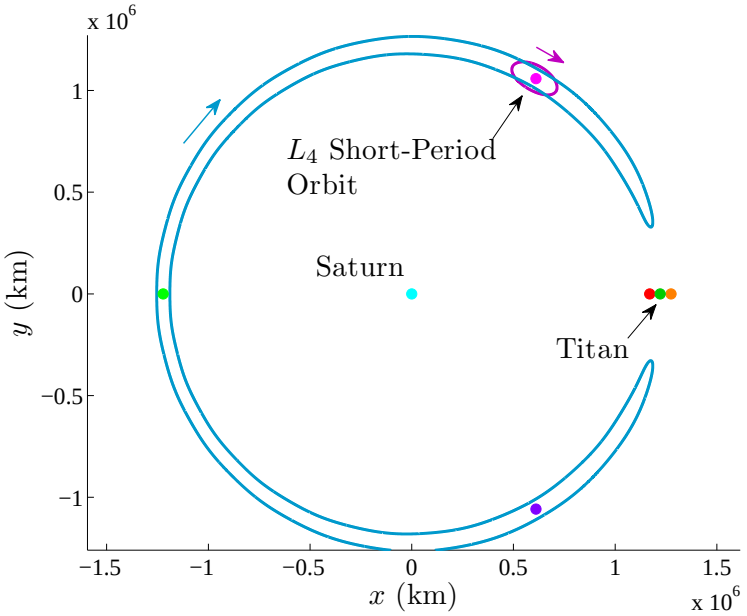

Figure 5.10. Intersecting Horseshoe Orbit and L_4 Short-Period Orbit in the Saturn-Titan System

Although only eight specific examples of instantaneous transfers between intersecting horseshoe and libration point orbits are examined here, an infinite number of other examples exist. A summary of the Δv costs for these eight sample transfers are listed in Table 5.3. Examples 1 and 2 clearly require the highest cost of the subset of transfers that are generated. A severe direction change is required to insert from the L_1 Lyapunov into the horseshoe orbit in this scenario, which results in the high cost. Examples 3 and 4 largely eliminate the direction change when shifting from an L_3 Lyapunov orbit to a horseshoe; however, reaching the original L_3 orbit is not necessarily trivial and such a requirement is not incorporated in this analysis. Insertion into a horseshoe orbit from a short period L_4 orbit is summarized in Examples 5 through 8 but also requires prior delivery into an L_4 periodic orbit. Nevertheless, the transfers from the L_3 Lyapunov are significantly lower in Δv cost as compared

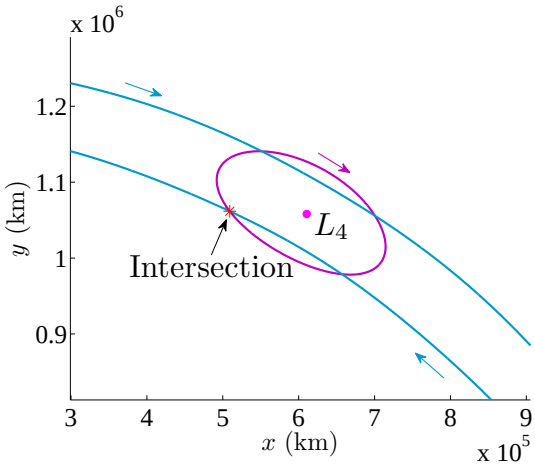

(a) Example 5, Zoom-In

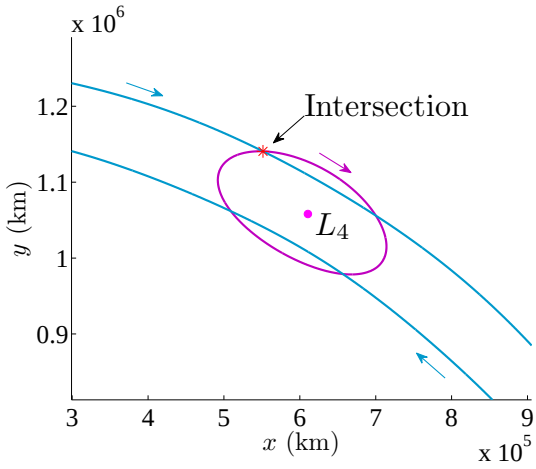

(b) Example 6, Zoom-In

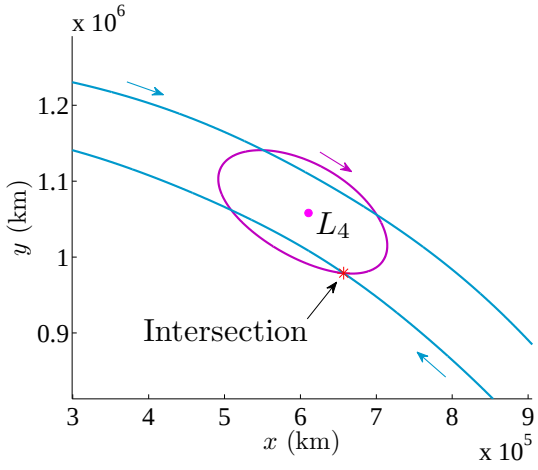

(c) Example 7, Zoom-In

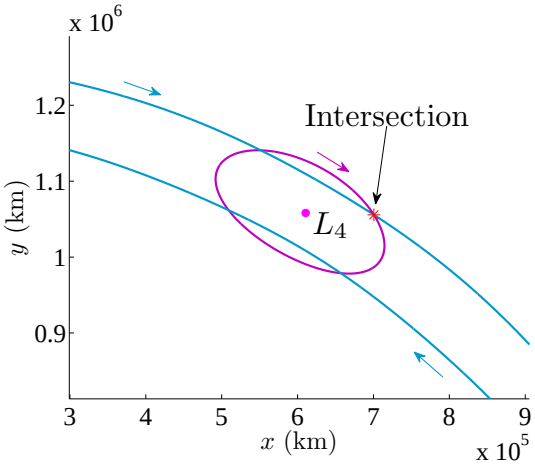

(d) Example 8, Zoom-In

Figure 5.11. Zoom-In of L_4 Short-Period-to-Horseshoe Intersections in Figure 5.10

to the transfers from the short-period L_4 orbit. This difference is partly explained by the larger energy difference in terms of Jacobi constant between the departure orbit and the arrival horseshoe orbit when originating in an L_4 orbit. Overall, it is apparent that a wide range of options are available. Given such reference solutions, an optimization scheme is suggested for further investigations.

Table 5.3 Transfers Between Intersecting Libration Point Orbits and Horseshoe Orbits

Case	$JC_{\text{L orbit}}$	JC_{HS}	Δv_x (m/s)	Δv_y (m/s)	$\lvert\Delta v_T\rvert$ (m/s)
Example 1	3.0000	3.0000	-831.6827	-262.3895	872.0919
Example 2	3.0000	3.0000	-458.4551	146.2057	481.2039
Example 3	2.9995	3.0008	-37.5967	-74.0718	83.0671
Example 4	2.9995	3.0008	-17.2138	73.2164	75.2128
Example 5	2.9972	3.0008	-2.0324	-227.5102	227.5192
Example 6	2.9972	3.0008	-176.2069	-121.4723	214.0196
Example 7	2.9972	3.0008	197.6930	121.4202	232.0030
Example 8	2.9972	3.0008	15.0854	214.0108	214.5418

5.3 Method: Orbital Transfers Using Unstable Invariant Manifolds

Another approach for computing transfers incorporates insight into the natural flow as it departs from the original orbit. In this strategy, an unstable L_1 or L_2 Lypunov orbit is selected as the departure orbit, and any horseshoe trajectory can be specified as the arrival orbit. Unstable manifolds associated with the departure orbit are computed first. Then, intersections between these unstable manifolds departing the Lyapunov orbit and the desired horseshoe orbit are isolated. Again, any technique that relies on intersecting orbits requires some numerical targeting to ensure that

the exact intersection position is available. To accomplish the targeting, both the horseshoe orbit and the unstable manifold of interest are propagated given their respective initial states until both reach the same x- or y-location, depending on the coordinate with the faster rate of change, as the approximate intersection. Then, the position coordinates corresponding to the unstable manifold and the velocity state on the horseshoe orbit at this end time are used as initial conditions to target a new horseshoe orbit. This new horseshoe orbit differs only slightly from the original, but ensures an exact known intersection with the unstable manifold departing the Lyapunov orbit. Since the maneuver cost to depart from the Lyapunov to the unstable manifold is theoretically zero, the only transfer cost for this type of strategy is the difference in velocity between the unstable manifold and the horseshoe orbit at this point of intersection.

5.3.1 Examples: Lyapunov-to-Horseshoe Transfers via an Unstable Manifold in the Saturn-Titan Three-Body System

To illustrate this approach for computing transfers, consider an example involving an L_1 Lyapunov orbit in the Saturn-Titan system, plotted in Figure 5.12(a). An unstable L_1 Lyapunov and a horseshoe orbit are selected such that both orbits are computed with the same value of Jacobi constant, but as observed in the figure, the two orbits do not intersect so a single impulse adjustment is not possible. Note that the unstable eigenvalue from the monodromy matrix corresponding to this Lyapunov orbit is $\lambda_1 = 200.0450$. The Lyapunov orbit is discretized into 30 points, and unstable manifolds are propagated for 0.3 years from each of these fixed points. The unstable manifolds are plotted in green in Figure 5.12(b). Hundreds of intersections between these 30 manifolds and the horseshoe are determined numerically, and a sample from this set of intersections is corrected to determine an exact intersection and the corresponding Δv. Although the newly corrected horseshoe orbits do not precisely retain the same value of Jacobi constant as the Lyapunov orbit and its manifolds, it is still

very close so, again, the Δv cost is primarily due to a change in direction. An example of a transfer from the L_1 Lyapunov to the horseshoe at one of the 539 identified intersections between the unstable manifolds and the horseshoe orbit is illustrated in Figure 5.13. Relevant cost and TOF information on this example transfer, labeled Example 1, is listed in Table 5.4. The transfer originates in the Lyapunov orbit, then moves along the unstable manifold, plotted in green, and naturally flows away from the Lyapunov. A Δv of magnitude 241.6889 m/s is then required to shift from the unstable manifold to the horseshoe orbit at their point of intersection. The time-of-flight is the length of time the unstable manifold is propagated, although TOFs along manifolds are generally difficult to directly compare to TOFs along two-impulse transfers. In this example, the TOF is 85.4213 days. There is a great variety of Δv costs and transfer times that exist in the subset of transfer trajectories that are highlighted in this example. Information on a sample set of the transfers, labeled Examples 2 through 7, for this particular scenario is listed in Table 5.4. Even greater variety is possible by selection of alternate departure and arrival orbits; the number of fixed points that are used to discretize the departure orbit may also yield an expanded set of options.

A similar investigation of transfers from a libration point orbit to a horseshoe orbit utilizing unstable manifolds is conducted by incorporating a Lyapunov orbit about L_2. Using the same original horseshoe trajectory as that identified in the previous example in Figure 5.13, an L_2 orbit is computed with the same value of Jacobi constant. This orbit and the corresponding unstable manifolds appear in Figure 5.14. Note that the unstable eigenvalue corresponding to this Lyapunov orbit is $\lambda_1 = 187.0099$. Again, the Lyapunov orbit is discretized into 30 points and the unstable manifolds are propagated for 0.3 years. Transfers between the Lyapunov and the horseshoe orbit are determined by utilizing intersections of the unstable manifolds and the horseshoe. An example of one of the hundreds of possible transfers found is illustrated in Figure 5.15. Relevant information on the cost and TOF of this transfer, labeled Example 1, is listed in Table 5.5. The Δv required to produce this transfer

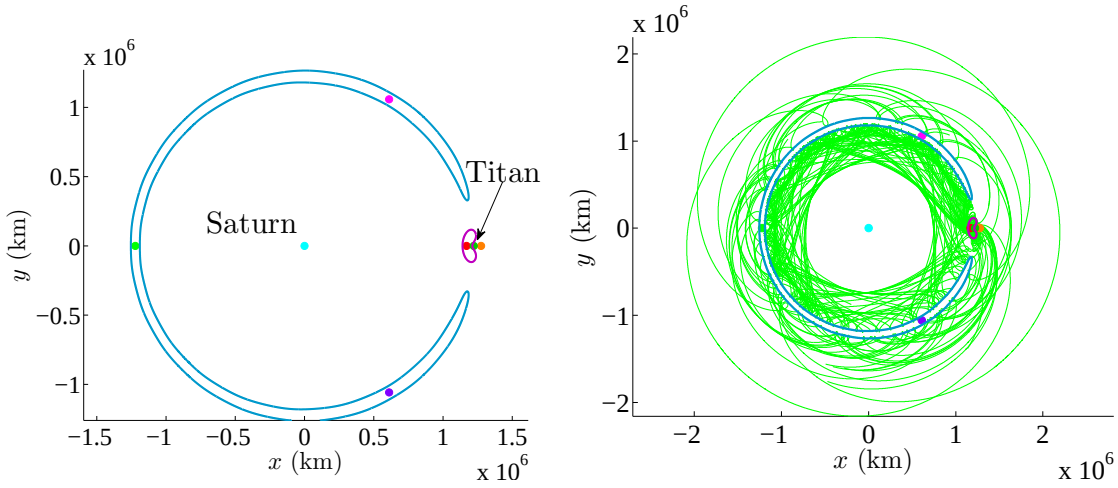

(a) L_1 Lyapunov and Horseshoe Orbit of Interest (b) Unstable Manifolds

Figure 5.12. L_1 Lyapunov and Associated Unstable Manifolds Used to Transfer to a Horseshoe Orbit in the Saturn-Titan System

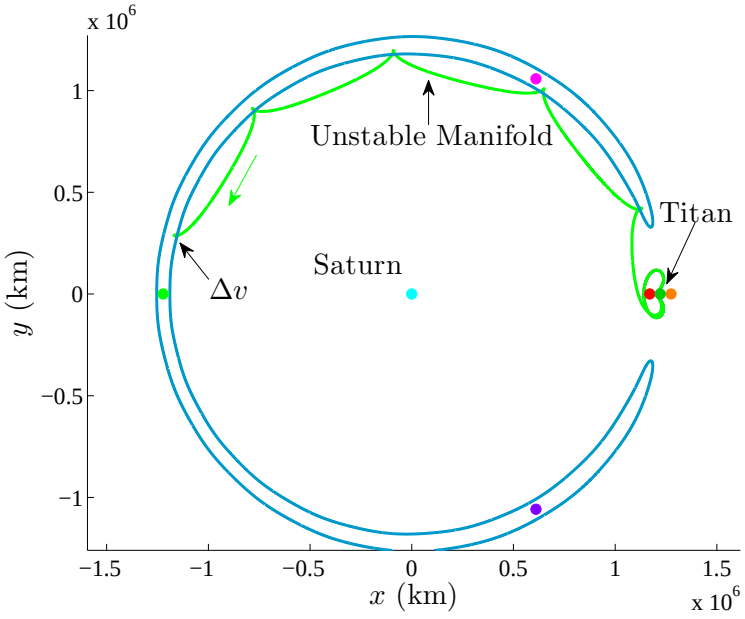

Figure 5.13. Example 1: Transfer Between an L_1 Lyapunov and Horseshoe Orbit Using an Unstable Manifold in the Saturn-Titan System

Table 5.4 Transfers to Horseshoe Orbits Using Unstable L_1 Lyapunov Manifolds in the Saturn-Titan System

Case	$\lvert\Delta JC\rvert$	Δv_x (m/s)	Δv_y (m/s)	$\lvert\Delta v_T\rvert$ (m/s)	TOF (days)
Example 1	1.3628×10^{-8}	-230.4311	-72.9044	241.6889	85.4213
Example 2	1.1533×10^{-4}	-578.8674	56.8852	581.6557	108.9142
Example 3	9.4122×10^{-9}	-535.3037	230.5698	582.8486	109.2840
Example 4	1.3257×10^{-8}	-15.1179	365.9036	366.2158	93.8459
Example 5	1.2118×10^{-8}	-61.2668	408.0116	412.5859	99.1236
Example 6	8.9995×10^{-9}	35.8699	404.0417	405.6308	87.8984
Example 7	9.2200×10^{-11}	97.7748	479.3993	489.2685	64.6554

is 207.2280 m/s, and the TOF along the transfer is 103.0070 days. These values are comparable to the results in the previous example. Many more transfers from this L_2 Lyapunov can be computed with this method, and a sample of these transfers, labeled Examples 2 through 7, are listed in Table 5.5.

5.3.2 Examples: Lyapunov-to-Horseshoe Transfers via an Unstable Manifold in the Sun-Jupiter Three-Body System

The previous two examples of transfers to horseshoe orbits using unstable Lyapunov manifolds are computed for the Saturn-Titan system, but similar transfers can also be computed for other systems, including the Sun-Jupiter system. A smooth horseshoe orbit and an unstable L_1 Lyapunov orbit are selected in the Sun-Jupiter system such that they share the same value of Jacobi constant. The instability in the Lyapunov orbit is comparable to the Saturn-Titan Lyapunovs, i.e., an unstable eigenvalue of $\lambda_1 = 216.8191$. These orbits are plotted in Figure 5.16(a). The Lyapunov is again discretized into 30 points, and unstable manifolds are propagated for

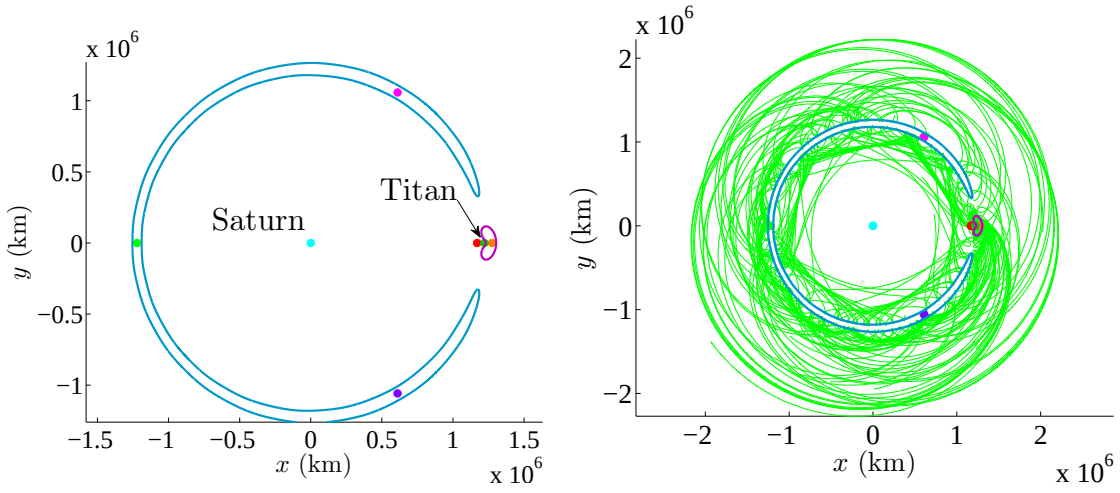

(a) L_2 Lyapunov Orbit and Horseshoe Trajectory of Interest

(b) Unstable Manifolds

Figure 5.14. L_2 Lyapunov and Associated Unstable Manifolds Used to Transfer to a Horseshoe Orbit in the Saturn-Titan System

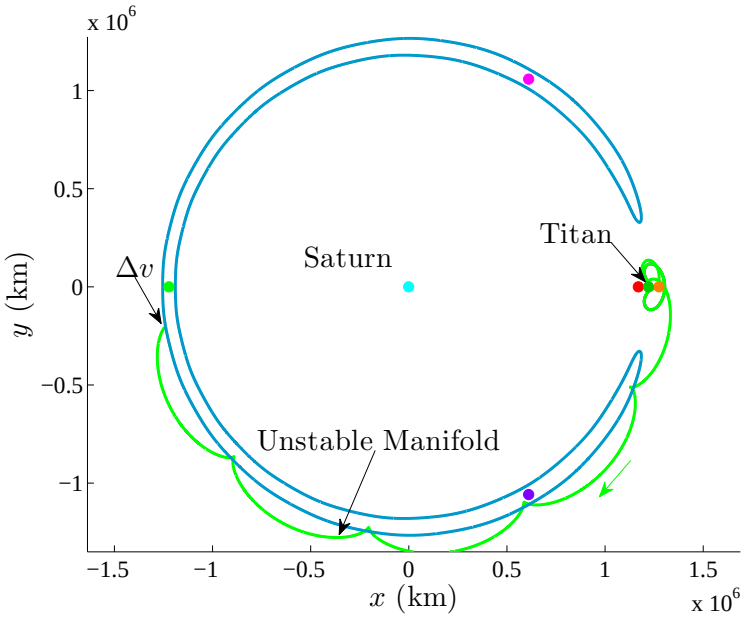

Figure 5.15. Example 1: Transfer Between an L_2 Lyapunov and Horseshoe Orbit Using an Unstable Manifold in the Saturn-Titan System

Table 5.5 Transfers to Horseshoe Orbits Using Unstable L_2 Lyapunov Manifolds in the Saturn-Titan System

Case	$\lvert\Delta JC\rvert$	Δv_x (m/s)	Δv_y (m/s)	$\lvert\Delta v_T\rvert$ (m/s)	TOF (days)
Example 1	9.9634×10^{-9}	-198.1467	60.6742	207.2280	103.0070
Example 2	2.0185×10^{-8}	-452.7821	35.2950	454.1557	51.5060
Example 3	1.3970×10^{-8}	-186.5212	104.5734	213.8358	97.0893
Example 4	1.1868×10^{-8}	-247.0759	71.7039	257.2702	78.3247
Example 5	5.6914×10^{-9}	-310.0780	-89.0464	322.6106	65.0567
Example 6	1.4761×10^{-8}	-191.3523	123.5054	227.7483	96.6521
Example 7	7.3803×10^{-9}	-51.0451	-399.4955	402.7435	48.0805

50 years. The manifolds appear in green in Figure 5.16(b). Maneuvers are then computed from the intersections of the unstable manifolds with the horseshoe orbit as previously described. An example of one of these transfers is plotted in Figure 5.17. Relevant information on this example transfer, labeled Example 1, is found in Table 5.6. The Δv required at the intersection of the manifold and the horseshoe to produce this transfer is 1109.6112 m/s, and the TOF is 40.9022 years. Clearly, both the Δv cost and the TOF are much higher in this example than in the examples from the Saturn-Titan system. Such a result is not surprising in a Sun-planet system. A 40-year TOF actually produces a smaller ratio when compared to the system period than in the Saturn-Titan examples. Several other examples of transfers from this L_1 Lyapunov, labeled Examples 2 through 7, are also summarized in Table 5.6.

Similar transfers are also generated by introducing a different departure orbit. If an L_2 Lyaupnov orbit is incorporated, the unstable manifolds are computed in the same manner done previously. The selected L_2 Lyapunov and the horseshoe orbit, both defined with the same Jacobi constant, are plotted in Figure 5.18(a). Again, the departure and arrival orbits do not intersect. The unstable manifolds corresponding

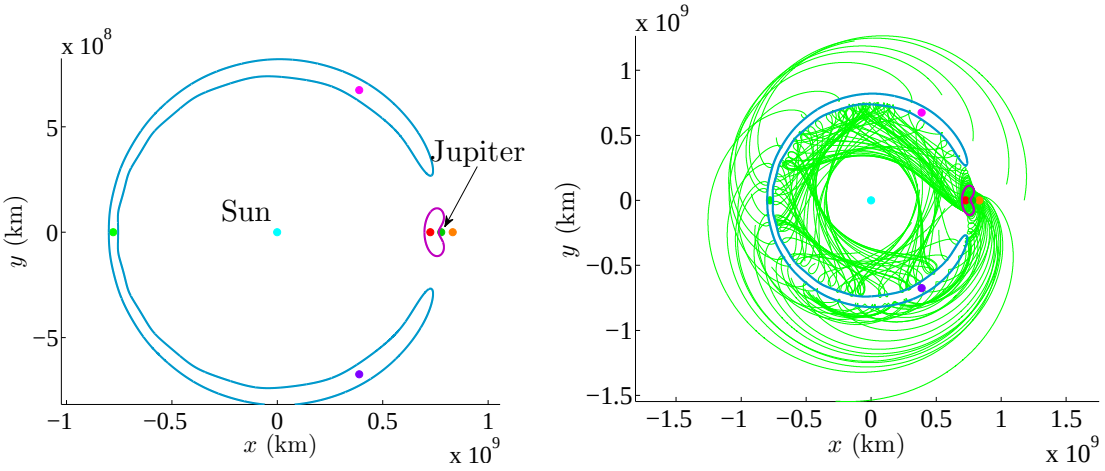

(a) L_1 Lyapunov Orbit and Horseshoe Trajectory of Interest

(b) Unstable Manifolds

Figure 5.16. L_1 Lyapunov and Associated Unstable Manifolds Used to Transfer to a Horseshoe Orbit in the Sun-Jupiter System

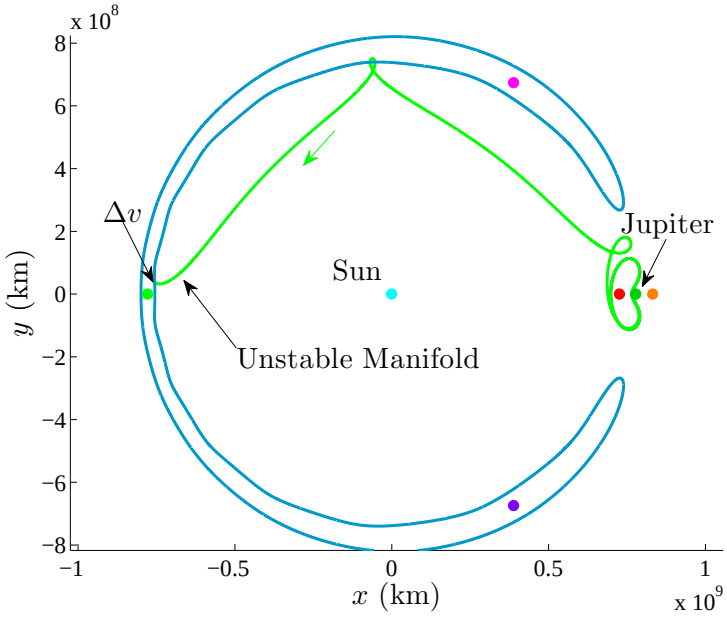

Figure 5.17. Example 1: Transfer Between an L_1 Lyapunov and Horseshoe Orbit Using an Unstable Manifold in the Sun-Jupiter System

Table 5.6 Transfers to Horseshoe Orbits Using Unstable L_1 Lyapunov Manifolds in the Sun-Jupiter System

Case	$\lvert\Delta JC\rvert$	Δv_x (m/s)	Δv_y (m/s)	$\lvert\Delta v_T\rvert$ (m/s)	TOF (years)
Example 1	2.1884×10^{-8}	251.3300	-1080.7730	1109.6112	40.9022
Example 2	4.3152×10^{-9}	-192.3808	-1055.0868	1072.4824	41.2919
Example 3	3.0936×10^{-8}	-57.4213	-1111.8640	1113.3457	46.3237
Example 4	2.7047×10^{-9}	-138.1076	640.3903	655.1133	43.8828
Example 5	2.4814×10^{-9}	-1157.0376	-3.8287	1157.0439	32.4032
Example 6	6.1801×10^{-8}	-756.1866	-817.8762	1113.8849	42.3354
Example 7	3.6286×10^{-8}	108.8729	-790.2341	797.6987	44.2297

to 30 fixed points along the L_2 Lyapunov are propagated for 50 years as seen in Figure 5.18(b). In this example, the unstable eigenvalue is $\lambda_1 = 193.6753$. An example of one of the resulting transfers is illustrated in Figure 5.19 and is listed as Example 1 in Table 5.7. A Δv to insert into the horseshoe from the unstable manifold is equal to 761.2357 m/s, and the corresponding flight time along the manifold arc is 46.3523 years. A variety of costs and times-of-flight are also summarized as Examples 2 through 7 in Table 5.7.

5.4 Method: Orbital Transfers Using Poincaré Maps with Unstable and Stable Manifolds

Although the strategies described thus far yield successful transfers, a useful technique to produce low Δv costs in the first guess is not apparent; therefore, an alternate approach is investigated. This approach attempts to incorporate both the unstable manifolds departing a Lyapunov orbit as well as the stable manifolds that asymptotically approach a horseshoe orbit. A low-Δv intersection between these two manifolds

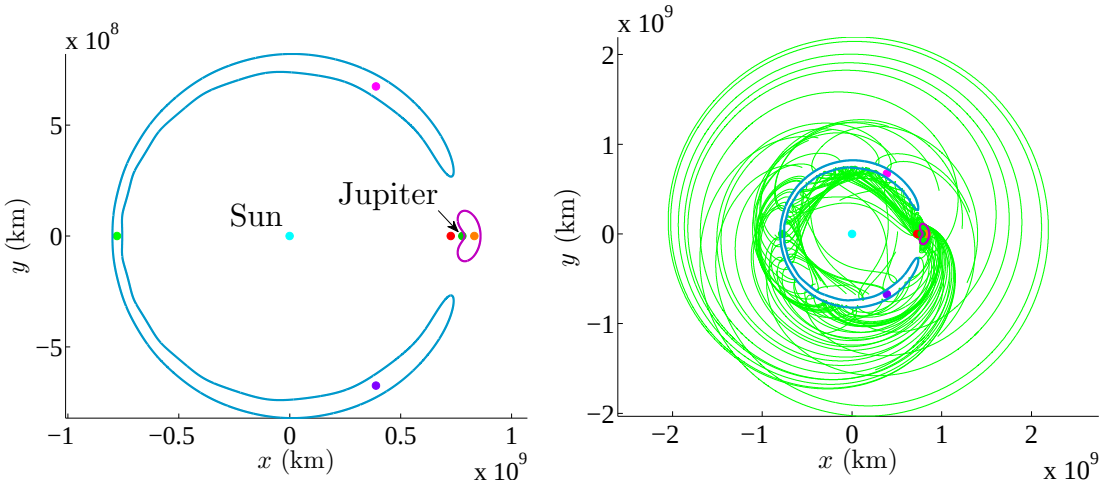

(a) L_2 Lyapunov and Horseshoe Orbit of Interest (b) Unstable Manifolds

Figure 5.18. L_2 Lyapunov and Associated Unstable Manifolds Used to Transfer to a Horseshoe Orbit in the Sun-Jupiter System

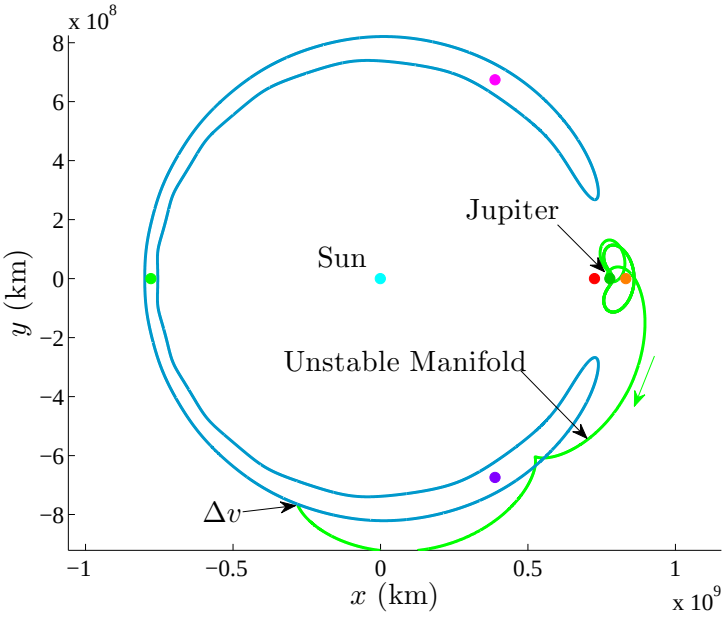

Figure 5.19. Example 1: Transfer Between an L_2 Lyapunov and Horseshoe Orbit Using an Unstable Manifold in the Sun-Jupiter System

Table 5.7 Transfers to Horseshoe Orbits Using Unstable L_2 Lyapunov Manifolds in the Sun-Jupiter System

Case	$\lvert\Delta JC\rvert$	Δv_x (m/s)	Δv_y (m/s)	$\lvert\Delta v_T\rvert$ (m/s)	TOF (years)
Example 1	3.1262×10^{-9}	-544.3541	-532.1263	761.2357	46.3523
Example 2	2.5271×10^{-7}	-293.1049	-1149.1737	1185.9641	43.3797
Example 3	6.3410×10^{-9}	-95.2863	-906.5413	911.5353	46.9751
Example 4	1.8814×10^{-8}	228.4628	-1248.6613	1269.3898	42.8345
Example 5	2.8950×10^{-8}	-77.9061	-937.4002	940.6320	36.0374
Example 6	1.4635×10^{-9}	-1186.7927	701.8848	1378.8108	34.7784
Example 7	1.1442×10^{-7}	-1216.0485	900.4491	1513.1367	28.3326

theoretically produces a low total transfer cost; however, a more sophisticated technique is required to determine potential intersections. Recall from Section 4.4 that the manifolds associated with the horseshoe orbits are quite complex. Manifolds of large Lyapunov orbits can also be difficult to visualize during longer time intervals and multiple close passages of the primaries. To gain insight into this problem, Poincaré maps are utilized.

5.4.1 Computing Transfers Using Poincaré Maps

Poincaré maps have proven to be very useful tools in locating connecting arcs between periodic orbits [42], [44], [47]. Poincaré maps offer a convenient framework to search for low-Δv transfers between various types of periodic orbits, in particular. Consider a departure orbit and an arrival orbit with the same value of Jacobi constant, and let both orbits be planar. If the unstable manifolds from the departure orbit are mapped onto a surface of section along with the stable manifolds of the arrival orbit, then isolating a pair of these points that intersect on the map should be relatively

straightforward. A potentially cost-free transfer trajectory is then available, provided the manifolds arrive at the surface of section at the same time. If an intersection of the two types of manifolds, with a common value of Jacobi constant, occurs on the map, the unstable and stable manifolds intersect in all four planar dimensions (x, y position and velocity states). Theoretically, no cost is required to transition from an orbit to its unstable manifold and, similarly, no maneuver is required to approach an orbit along its stable manifold. Therefore, if an unstable manifold associated with one orbit intersects a stable manifold associated with another orbit on a Poincaré map at the same time, the transfer between the two orbits is free. This type of transfer that joins two different orbits by their respective unstable and stable manifolds is frequently labeled a heteroclinic connection [37], [48]. The existence of this type of connection in periodic orbits was demonstrated by Koon et al. for applications in astrodynamics [47]. Even if a precise four-state intersection is not identified, the Poincaré map supplies useful information for the location of unstable and stable manifolds that nearly intersect. A pair of unstable and stable manifolds that nearly intersect could be numerically corrected to intersect in position but not necessarily in velocity, and yet allow a relatively low Δv maneuver cost.

Three specific strategies are used to sequentially compute transfers using Poincaré maps in this investigation. Ideally, these three steps can proceed in a series to produce very low-cost or free transfers. The first two strategies yield transfers that involve a cost, and the third represents the ideal heteroclinic connection. Simple sketches reflecting these three types of transfers for generic departure and arrival orbits are illustrated in Figure 5.20. The first type, i.e., Type 1, in Figure 5.20(a) incorporates three maneuvers to complete a transfer from a departure orbit to a final arrival orbit. Such a transfer departs at a specified position on the starting orbit, and requires a small Δv to initiate the transfer and deliver the vehicle to the appropriate intersection point. The second Δv connects the first segment of the transfer arc that originates with the unstable manifold of the departure orbit (in green) to the second segment along the transfer arc that is computed from the stable manifold of the arrival orbit

(in pink). These two manifolds must be continuous in position, but not velocity. The third maneuver is required at arrival to ensure insertion at a specified position at the correct time. Note that, although the reference trajectories for this transfer are developed from invariant manifolds, a numerical corrections process is employed and the final transfer arc may not be comprised of precise manifold trajectories. The second type (Type 2) of transfer is then generated from the Poincaré map. This type involves only two Δv corrections and is represented in Figure 5.20(b). This new transfer is identical to the first type with the exception that the Δv maneuver to connect the two segments of the transfer arc has been eliminated. In many examples, a Type 1 transfer includes only a small Δv maneuver at the interior location along the transfer arc that can often be removed. This maneuver is eliminated simply by introducing a change in the constraints in a multiple shooting scheme. A Type 3 transfer is illustrated in Figure 5.20(c), and is cost-free. From the Poincaré map, a heteroclinic connection sometimes emerges. An exact or nearly exact intersection is required by the differential corrections process to produce a heteroclinic connection. Similar to the previous two types, the third approach is constructed from both an unstable and a stable manifold; however, in this case, the transfer arcs do not enter the departure and arrival arcs at specified locations. Instead, the manifold arcs are allowed to asymptotically depart or approach the orbits as necessary to remove the Δv. A Type 3 transfer can frequently be produced from a multiple shooting algorithm that is initiated with a Type 2 transfer as the initial guess.

5.4.2 Examples: Lyapunov-to-Horseshoe Transfers in the Saturn-Titan Three-Body System

The first set of sample transfers computed using Poincaré maps are based on an L_1 Lyapunov orbit and a horseshoe trajectory with the same value of Jacobi constant. Both are unstable, as necessary to produce useful invariant manifolds. To compute the unstable manifolds, the Lyapunov is discretized into 300 points, and each

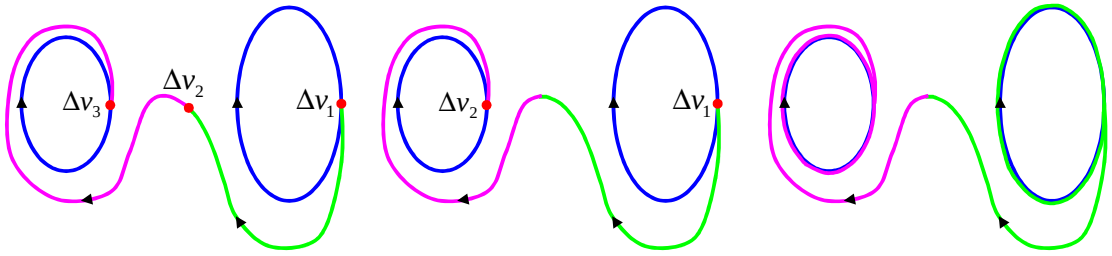

(a) Type 1 (b) Type 2 (c) Type 3

Figure 5.20. Three Strategies to Generate Transfers with Poincaré Maps

manifold is propagated for three years. Similarly, stable manifolds associated with the horseshoe are generated by discretizing the orbit into 300 points and propagating each manifold for three years. Then, a Poincaré map of these manifolds is created such that the surface of section is the line $x = x_{L_3}$. Note that any desired location for the section may be selected; however, from experience, locating the hyperplane at L_3 yields low transfer costs. The resulting Poincaré map appears in Figure 5.21. The green points represent intersections of the unstable manifolds departing from the Lyapunov orbit with the surface of section, while the pink points, generated by propagating in negative time, correspond to intersections of the stable manifolds that are approaching the horseshoe trajectory with the map. In the one-sided map in Figure 5.21, only those unstable trajectories that pass through the surface of section with decreasing x-position are recorded; only stable trajectories which pass through with an increasing x-position (in reverse time) are retained. A simple search algorithm isolates pairs of unstable and stable points on the map that are very near each other. The pair of points employed in this example is marked by the blue box in Figure 5.21. Once a pair of points is isolated, the two corresponding manifold trajectories are used to compute transfers.

Given a pair of unstable and stable manifolds from the Poincaré map, a Type 1 transfer with three maneuvers is computed. The resulting trajectory is plotted in

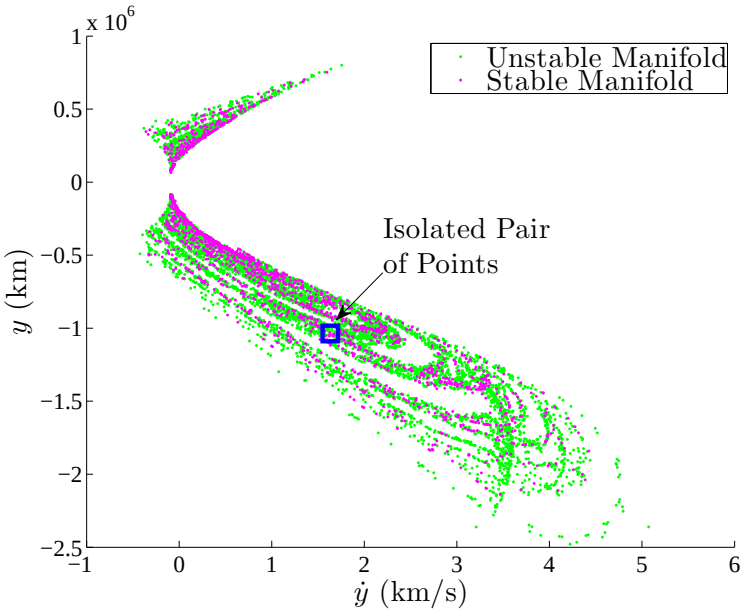

Figure 5.21. Poincaré Map of Unstable L_1 Lyapunov Manifolds and Stable Horseshoe Manifolds in the Saturn-Titan System

Figure 5.22. The transfer originates on the purple Lyapunov orbit. A Δv maneuver is implemented to exit the periodic Lyapunov orbit and move along the dotted green trajectory in the figure. A second maneuver connects the path to the dotted pink trajectory. Finally, a third and final Δv allows entry into the horseshoe orbit, plotted in blue. The Δv magnitudes and TOF are listed in Table 5.8.

Eliminating the interior maneuver yields the two-impulse Type 2 transfer as plotted in Figure 5.23. Not surprisingly, this transfer appears nearly the same as the Type 1 transfer in Figure 5.22; the original interior maneuver is relatively small. The trajectory is numerically corrected to be continuous in position and velocity except at the departure and insertion points, where a discontinuity in velocity is represented by the two Δv maneuvers in the plot. See Table 5.8 for a listing of the Δv and TOF values.

Lifting the constraint on the departure and arrival points yields a heteroclinic connection (Type 3) that is illustrated in Figure 5.24. The trajectory flowing from

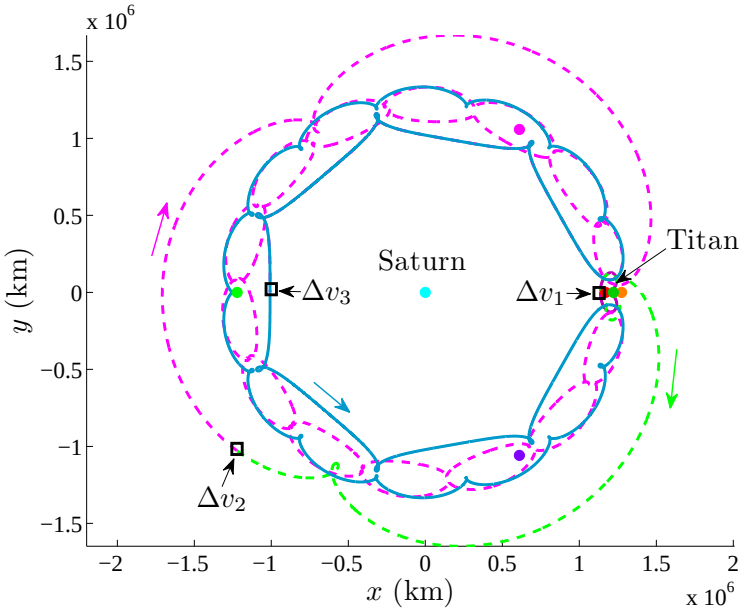

Figure 5.22. Three-Maneuver Transfer from an L_1 Lyapunov Orbit to a Horseshoe Trajectory in the Saturn-Titan System

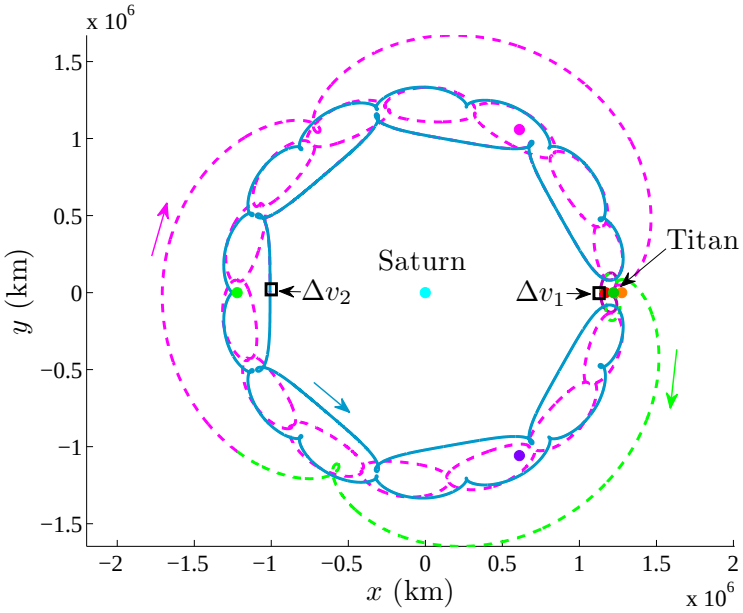

Figure 5.23. Two-Maneuver Transfer from an L_1 Lyapunov Orbit to a Horseshoe Trajectory in the Saturn-Titan System

the Lyapunov to the horseshoe orbit is completely continuous, therefore it is a cost-free transfer. The dotted green and pink trajectories complete several revolutions about the Lyapunov and horseshoe orbits, respectively. To aid in visual clarity, the Lyapunov and horseshoe orbits are plotted in purple and blue over the heteroclinic trajectory so that the initial and final orbits are apparent in this complex image. The TOF for the heteroclinic connection is computed by subtracting the appropriate number of periods of the Lyapunov and the horseshoe from the total TOF of the continuous trajectory. This subtraction is to negate the time added to the TOF due to stacking additional revolutions of the orbits at the beginning and end of the transfer as the manifolds wind off and wind onto the appropriate periodic orbits. The TOF for this Type 3 transfer is listed in Table 5.8. Clearly, the trade-off for these low-cost transfers is an extended transfer time.

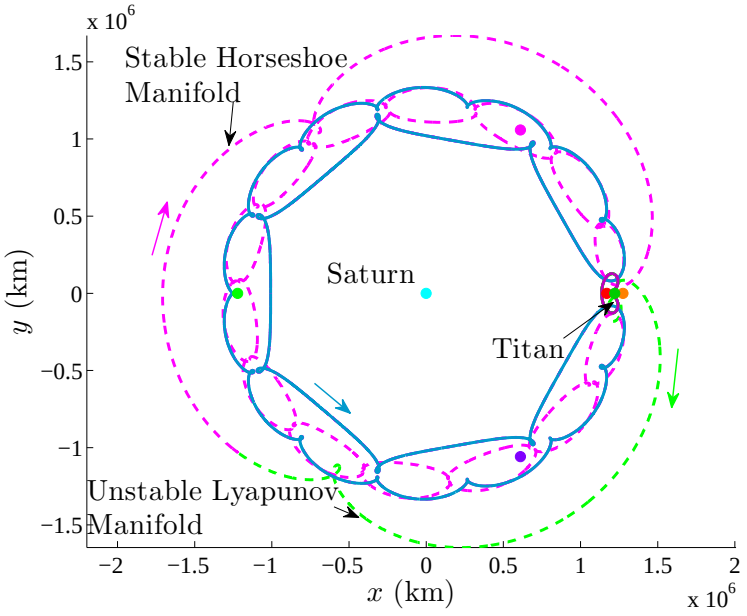

Figure 5.24. Heteroclinic Connection Between an L_1 Lyapunov Orbit and a Horseshoe Trajectory in the Saturn-Titan System

A summary of the Δv costs and TOF for the previous example is presented in Table 5.8. All three transfer types deliver nearly the same TOF, which is much longer

than the sample transfers computed using a single unstable manifold. However, the cost, Δv_T, is much lower for these transfers computed with the Poincaré map. The sample Type 1 and Type 2 transfers both yield a low cost, and the Type 3 transfer is theoretically cost-free.

Table 5.8 Transfer from an L_1 Lyapunov to a Horseshoe Orbit Using a Poincaré Map in the Saturn-Titan System

Type	$\lvert\Delta v_1\rvert$ (m/s)	$\lvert\Delta v_2\rvert$ (m/s)	$\lvert\Delta v_3\rvert$ (m/s)	$\lvert\Delta v_T\rvert$ (m/s)	TOF (days)
1	9.0836	2.3718	0.4185	11.8739	561.0863
2	6.1592	4.1353	N/A	10.2945	561.1455
3	N/A	N/A	N/A	0	561.1691

A sample transfer connecting an L_2 Lyapunov to a horseshoe orbit in the Saturn-Titan system is also computed using a Poincaré map. The same process employed in the previous example is used to compute a Poincaré map, pictured in Figure 5.25, of the appropriate manifolds associated with the L_2 Lyapunov orbit and horseshoe orbit. Using the methods detailed in the previous example, transfers of Types 1, 2, and 3 are computed using a pair of points isolated on the map as an initial guess. All three transfer types are nearly identical, therefore only the cost-free transfer of Type 3 appears in Figure 5.26. The continuous trajectory flows along the Lyapunov orbit, onto an associated unstable manifold, then onto a stable manifold associated with the horseshoe trajectory, and finally approaches the horseshoe orbit. The Δv costs and TOF for each transfer type in this example are listed in Table 5.9. Again, the Δv costs are very low, and eventually drop to zero. The TOF is nearly the same for all three transfer types as the sequence eventually delivers the heteroclinic-type transfer. The TOF for this example departing from an L_2 Lyapunov orbit is significantly longer than the example shown departing from an L_1 Lyapunov orbit in Table 5.8, but this

extended TOF reflects the increased number of revolutions the transfer trajectory completes around the system.

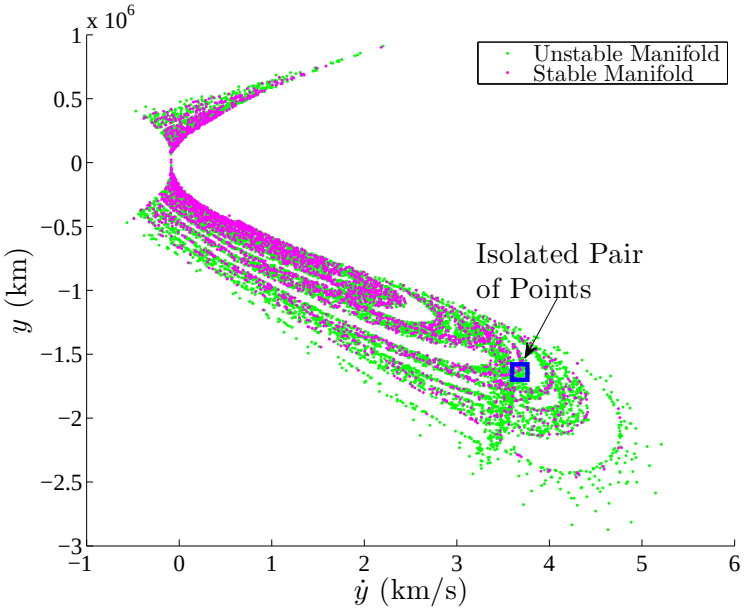

Figure 5.25. Poincaré Map of Unstable L_2 Lyapunov Manifolds and Stable Horseshoe Manifolds in the Saturn-Titan System

Table 5.9 Transfer from an L_2 Lyapunov to a Horseshoe Orbit Using a Poincaré Map in the Saturn-Titan System

Type	$\lvert\Delta v_1\rvert$ (m/s)	$\lvert\Delta v_2\rvert$ (m/s)	$\lvert\Delta v_3\rvert$ (m/s)	$\lvert\Delta v_T\rvert$ (m/s)	TOF (days)
1	1.4794	3.7757	1.3965	6.6516	726.2750
2	1.0596	2.4851	N/A	3.5477	726.2617
3	N/A	N/A	N/A	0	726.1898

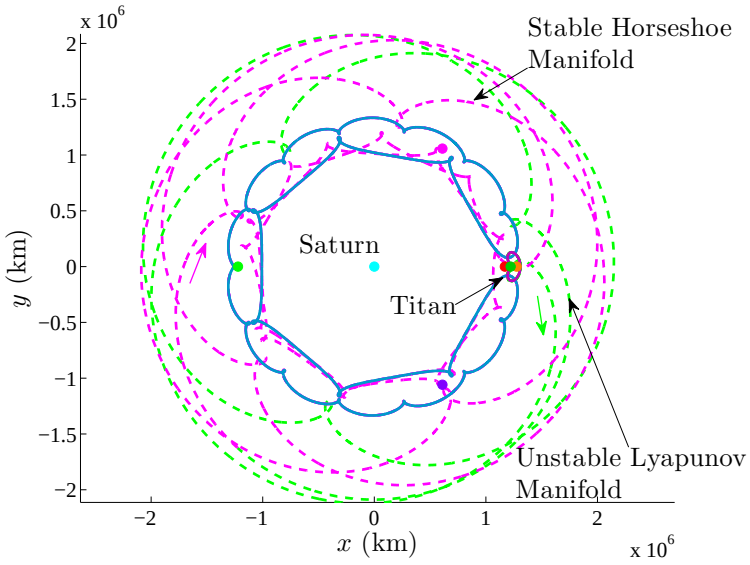

Figure 5.26. Heteroclinic Connection Between an L_2 Lyapunov Orbit and a Horseshoe Trajectory in the Saturn-Titan System

5.4.3 Examples: Lyapunov-to-Horseshoe Transfers in the Sun-Jupiter Three-Body System

To examine the possibility of transfers to horseshoe orbits in a very large system, Poincaré maps are also used to find transfers between a Sun-Jupiter L_1 Lyapunov orbit and a horseshoe trajectory. Unstable manifold corresponding to 300 fixed points on the Lyapunov orbit are propagated for 50 years, and stable manifolds associated with 300 fixed points on the horseshoe orbit are propagated for 700 years. The Poincaré map resulting from the intersection of the appropriate invariant manifolds with the surface of section is plotted in Figure 5.27. A pair of points is isolated from the map, and transfer trajectories of Types 1, 2, and 3 are computed. Again, all three types look nearly identical; a cost-free heteroclinic connection transfer does emerge and is plotted in Figure 5.28. The costs and TOF for each of the three transfer types in this example are listed in Table 5.10. Notice that the total Δv for the initial three-maneuver transfer, Type 1, is significantly larger than the other two transfer types. However, the multiple shooting algorithm successfully shifts the interior points

to remove the interior maneuver and produce a Type 2 result. The TOF remains very similar. Shifting the locations along the departing and arrival orbits eventually yields a cost-free Type 3 transfer. Although the Δv requirements for this example are reduced to a low cost, 451 years for the TOF is extremely long for mission application purposes.

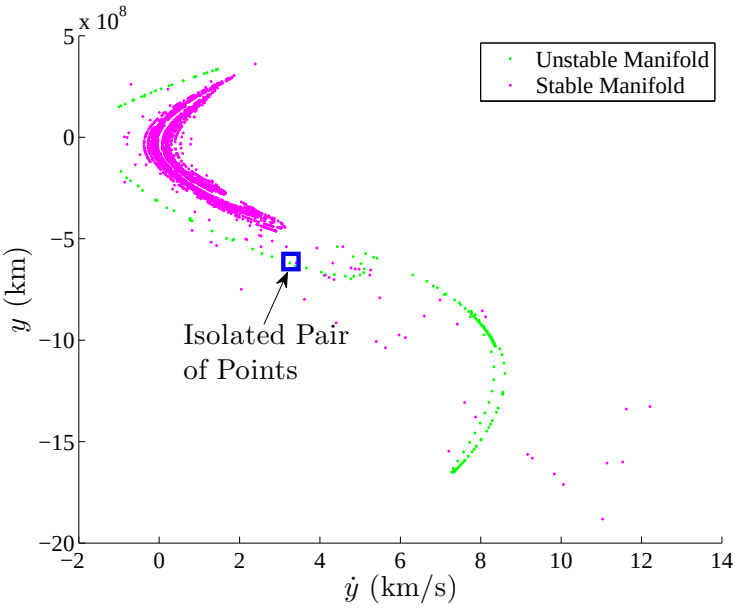

Figure 5.27. Poincaré Map of Unstable L_1 Lyapunov Manifolds and Stable Horseshoe Manifolds in the Sun-Jupiter System

Table 5.10 Transfer from an L_1 Lyapunov to a Horseshoe Orbit Using a Poincaré Map in the Sun-Jupiter System

Type	$\lvert\Delta v_1\rvert$ (m/s)	$\lvert\Delta v_2\rvert$ (m/s)	$\lvert\Delta v_3\rvert$ (m/s)	$\lvert\Delta v_T\rvert$ (m/s)	TOF (years)
1	6.8064	192.0084	8.3524	207.1672	451.4299
2	0.1344	2.3229	N/A	2.4573	451.5972
3	N/A	N/A	N/A	0	451.5940

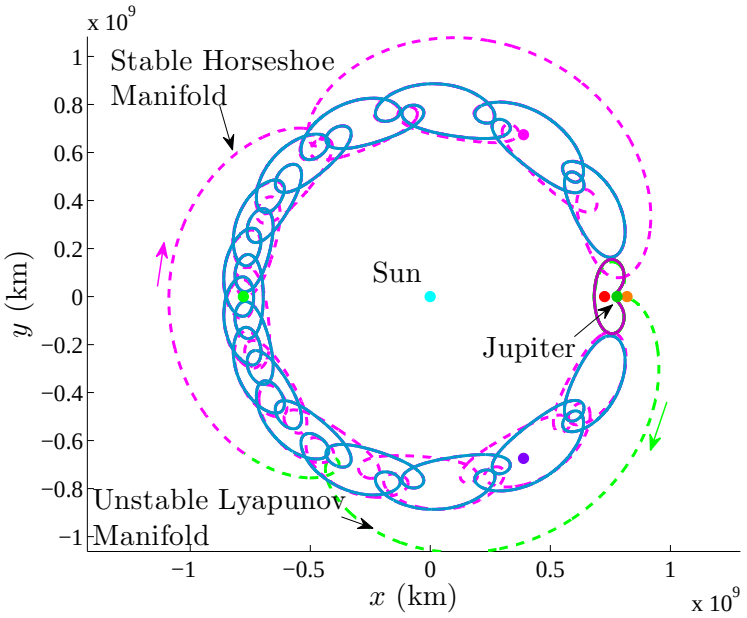

Figure 5.28. Heteroclinic Connection Between an L_1 Lyapunov Orbit and a Horseshoe Trajectory in the Sun-Jupiter System

In a final example, transfers utilizing Poincaré maps are computed that originate from an L_2 Lyapunov orbit and deliver the vehicle to a horseshoe trajectory in the Sun-Jupiter system. The Poincaré map for this example is computed using the same method as previous examples. The resulting map is plotted in Figure 5.29. A pair of nearly intersecting points is isolated on the map and used to produce transfers of Types 1, 2, and 3. The cost-free heteroclinic connection, transfer Type 3, is representative of this example and is plotted in Figure 5.30. The costs and TOF for each of the three transfer types are listed in Table 5.11. As in the previous example departing an L_1 orbit in the Sun-Jupiter system, the total Δv for the three-maneuver scheme in transfer Type 1 is significantly higher, although all three types share a similar TOF of about 443 years, which is prohibitively long for mission applications. Nevertheless, to examine the trade-off between Δv cost and TOF, a comparison of the various methods explored for computing transfers to periodic horseshoe orbits is explored.

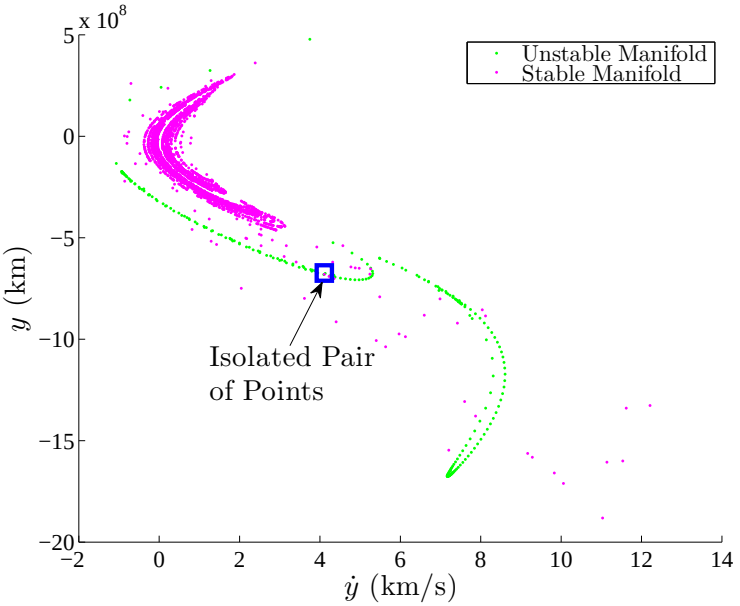

Figure 5.29. Poincaré Map of Unstable L_2 Lyapunov Manifolds and Stable Horseshoe Manifolds in the Sun-Jupiter System

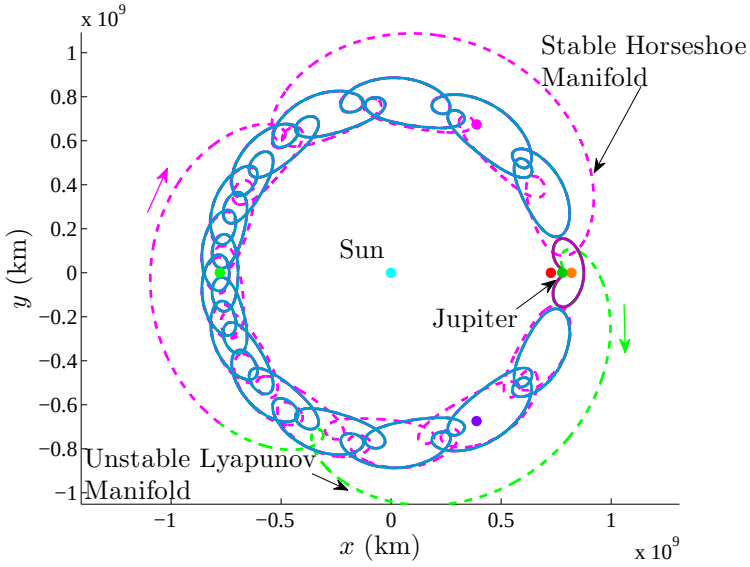

Figure 5.30. Heteroclinic Connection Between an L_2 Lyapunov Orbit and a Horseshoe Trajectory in Sun-Jupiter System

Table 5.11 Transfer from an L_2 Lyapunov to a Horseshoe Orbit Using a Poincaré Map in the Sun-Jupiter System

Type	$\|\Delta v_1\|$ (m/s)	$\|\Delta v_2\|$ (m/s)	$\|\Delta v_3\|$ (m/s)	$\|\Delta v_T\|$ (m/s)	TOF (years)
1	48.2642	22.6958	34.0120	104.9721	443.5977
2	0.3656	3.8745	N/A	4.2401	443.4067
3	N/A	N/A	N/A	0	443.4075

5.5 Comparison of Δv Costs and Transfer Times-of-Flight

The various approaches for computing transfers between libration point orbits and horseshoe trajectories offer assorted maneuver costs and transfer times. It is useful to compare the TOF and the associated maneuver costs from each of the examples that exploit the various strategies for determining transfers. Recall that the first approach introduced in Section 5.2 simply uses a single-impulse adjustment to shift between two orbits that possess a position intersection. An alternative method from Section 5.3 uses intersections between unstable manifolds associated with a Lyapunov orbit to connect the Lyapunov orbit to a horseshoe orbit. Finally, the third technique, described in Section 5.4, exploits a Poincaré map constructed with the unstable manifolds departing a Lyapunov orbit and the stable manifolds that approach a horseshoe orbit to determine low-cost transfer trajectories.

To aid in the comparison of the results from the examples in the Saturn-Titan system, the total cost, Δv_T, is represented as a function of TOF in Figure 5.31. Note that the example targeted from a Hohmann transfer approximation is not represented in the plot since the required Δv is unreasonably large and therefore not viable. The direct shifts using intersecting libration point orbits and horseshoe trajectories appear in blue. Obviously, the instantaneous change in the velocity vectors require zero TOF. Clearly, a wide range of Δv values is observed for such shifts. Some examples

departing from an L_3 Lyapunov do exist for less than 100 m/s, thus, careful selection of the intersecting points can retain a reasonable cost, but no attempt is made to incorporate the costs or time to reach the departure orbit. The sample transfers that employ an unstable manifold as it departs the Lyapunov orbit are plotted in pink. Again, a reasonably large range of costs is observed, although the TOF does not vary greatly. Likely, some future exploration may yield costs on the order of 100 m/s for these types of transfers as well. Lastly, the sample transfers computed using stable and unstable manifolds and Poincaré maps are plotted in orange. These transfers are clearly of the lowest cost (or free), but their TOF is considerably larger than the other types of transfers; a long TOF is common with low-energy transfers though. Note that variation in both TOF and Δv could be found by selecting a different Poincaré section.

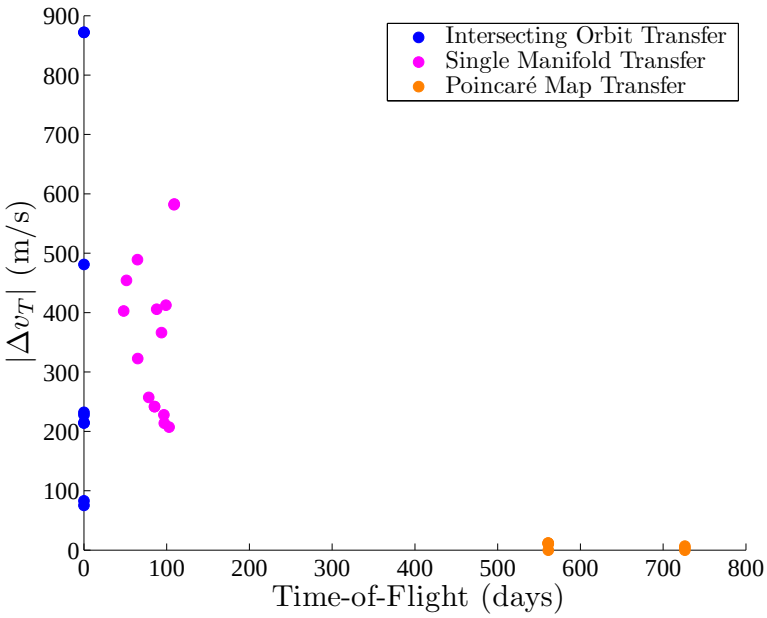

Figure 5.31. Comparison of Δv and TOF for Sample Transfers in the Saturn-Titan System

To compare the results from examples in the Sun-Jupiter system, Δv_T vs. TOF (in years) is plotted in Figure 5.32. Again, the targeted Hohmann transfer example is not included. Note that shifts using intersecting orbits are not computed for this sys-

tem. For the sample transfers produced here, the same general observations from the Saturn-Titan system also emerge in the Sun-Jupiter system. The transfers computed using one unstable Lyapunov manifold are more expensive, yet require less time than the transfers computed using the Poincaré map. The transfers computed with the Poincaré map again deliver very low costs, but the TOF, which is around 450 years, is exceptionally long.

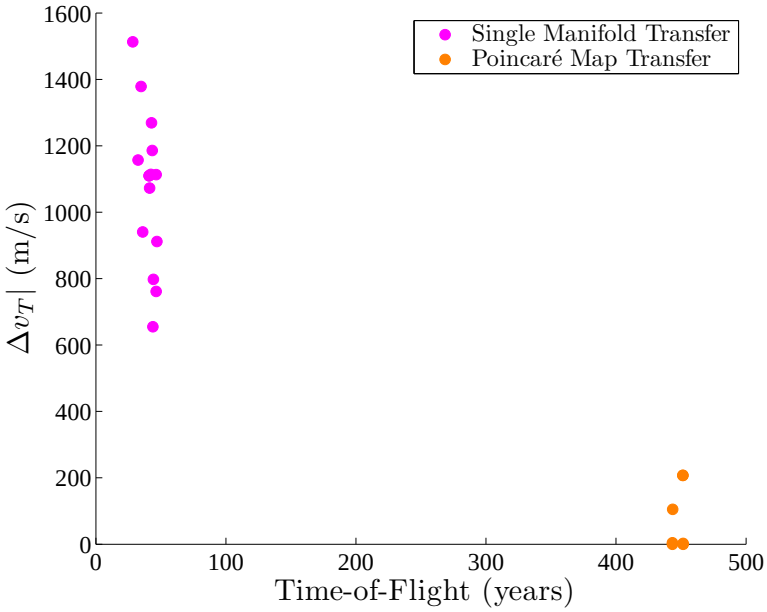

Figure 5.32. Comparison of Δv and TOF for Sample Transfers in the Sun-Jupiter System

6. SUMMARY AND RECOMMENDATIONS

In this chapter, a summary of the preliminary investigation into transfers from libration point orbits to horseshoe orbits is presented. Additionally, some recommendations for further development of the research are provided; specifically, possible extensions in terms of transfer design concepts and computational tools are listed.

6.1 Summary

A preliminary analysis of transfers from libration point orbits to horseshoe orbits is the principal focus of this investigation; the Saturn-Titan system and the Sun-Jupiter system are used as representative systems. Prior to the investigation of transfer trajectories, families of periodic horseshoe orbits are computed. To facilitate the computation of transfer trajectories, invariant manifolds associated with both unstable periodic Lyapunov orbits as well as periodic horseshoe trajectories are examined. Transfers between these types of orbits require some type of transfer concept and a corresponding initial guess.

Arrival in the vicinity of a given horseshoe orbit and a subsequent insertion are constructed based on three different types of concepts. The first concept simply links a libration point orbit and a horseshoe orbit that intersect in position space at the appropriate time. Great variation in the Δv cost of such instantaneous velocity adjustments is observed, based upon the selection of departure and arrival orbits, as well as the difference in energy between the orbits and the required directional changes at the point of intersection. The second transfer concept exploits the natural dynamics of the system. The transfer flows naturally from an unstable Lyapunov orbit along its unstable manifold and, then, only one Δv is required to enter into the horseshoe orbit. Although this technique utilizes the natural flow surrounding the

departure orbit, much variation in Δv is observed upon arrival in the vicinity of the horseshoe orbit.

A third and final transfer concept utilizes the natural flow near both the departure and arrival orbits. A one-sided Poincaré map is employed to represent the intersections of a selected surface of section with the unstable manifolds departing a Lyapunov (departure) orbit and the stable manifolds flowing towards a horseshoe (arrival) orbit. This method allows for more flexibility in the design of a trajectory. Instead of guessing a particular unstable manifold and checking the cost of insertion to assess feasibility, this design concept exploits the insight available in the Poincaré map. Selecting a pair of unstable and stable manifolds that nearly intersect on the map as an initial guess for a transfer trajectory is a convenient way to determine a low-cost transfer. Using Poincaré maps, extremely low-energy transfers are observed in both the Saturn-Titan and Sun-Jupiter examples although, as expected, the time-of-flight along the Sun-Jupiter transfers is prohibitively long. In fact, in all of the sample transfers generated in this investigation, heteroclinic connections are available to link a Lyapunov orbit and horseshoe orbit and thus, theoretically, cost-free transfers to the horseshoe orbits exist. The primary conclusions of this investigation are as follows:

(i) Horseshoe orbits are feasible as low-cost options, particularly for end-of-life mission scenarios. Transfers to the horseshoe orbits from Lyapunov orbits can be computed that theoretically require no cost in terms of impulsive maneuvers, but incur very long times-of-flight. The lengthy time-of-flight requires a trade-off, but it is quite likely that many other transfers exist with a shorter time-of-flight and still manageable cost. This investigation is only intended as a preliminary analysis of possible transfer options.

(ii) Poincaré maps are a useful tool in designing low-cost transfer trajectories to unstable horseshoe orbits. They offer notable advantages and insight over some alternative transfer concepts and computational methods. Specifically, Poincaré

maps constructed from invariant manifolds offer insight into the natural flow near both the departure and arrival orbits. This insight allows for a more informed initial guess of a possible low-cost transfer.

Thus, periodic horseshoe orbits are viable for certain mission scenarios, and Poincaré maps offer a convenient initial guess for low-cost transfers to enter into unstable horseshoe orbits.

6.2 Recommendations for Future Development

This investigation into transfer trajectories to reach horseshoe orbits is only preliminary. A variety of extensions are warranted in terms of both transfer concepts and the most appropriate computational tools. In terms of transfer concepts, further issues to be addressed are as follows:

(i) The scope of this investigation can be expanded to include transfers computed between three-dimensional orbits. Many spacecraft move along three-dimensional paths, therefore the computation of three-dimensional horseshoe orbits and the associated transfer trajectories is appropriate.

(ii) An investigation into the original delivery of a vehicle to the "departure" orbit that initiates the transfer is warranted. The method used to enter into the departure orbit may depend on the system involved.

(iii) The investigation could also be extended to include transfer trajectories to tadpole orbits, a type of orbit closely related to the horseshoe orbits that only encompasses one equilateral libration point.

(iv) It is of interest to compute transfers and the associated costs for a specific mission scenario. Transfers computed for a potential mission to study specific asteroids in horseshoe orbits near Earth, such as Cruithne or 2002 AA_{29}, are interesting options. Naturally, then, it is also of interest to investigate transfers

to horseshoe orbits in systems other than Saturn-Titan and Sun-Jupiter, such as the Sun-Earth system.

To support transfer trajectory design and increase computational capabilities, several suggestions to be considered include:

(i) Poincaré maps are only employed to determine transfer trajectories at select energy levels in this investigation; however, an extension of the maps at various energy levels could reveal further insight into transfer options.

(ii) Optimization algorithms could be employed to determine transfers with a desired combination of Δv cost and time-of-flight. For example, the location of the Poincaré surface of section is currently selected arbitrarily, but an optimization scheme could be used to strategically place the surface of section to determine transfers with desirable cost and time-of-flight characteristics.

Further development of transfer concepts and computational tools is necessary to facilitate these recommendations that are offered for future development.

LIST OF REFERENCES

LIST OF REFERENCES

[1] V. Szebehely. *Theory of Orbits: The Restricted Problem of Three Bodies*. Academic Press Inc., New York, New York, 1967.

[2] M. Connors, P. Chodas, S. Mikkola, P. Weigert, C. Veillet, and K. Innanen. Discovery of an Asteroid and Quasi-Satellite in an Earth-like Horseshoe Orbit. *Meteoritics and Planetary Science*, 37:1435–1441, 2002.

[3] E. W. Brown. On a New Family of Periodic Orbits in the Problem of Three Bodies. *Monthly Notices of the Royal Astronomical Society*, 71:438–454, 1911.

[4] S. F. Dermott and C. D. Murray. The Dynamics of Tadpole and Horseshoe Orbits: I. Theory. *Icarus*, 48(1):1–11, October 1981.

[5] P. A. Wiegert, K. A. Innanen, and S. Mikkola. An asteroidal companion to the Earth. *Nature*, 387:686–686, June 1997.

[6] S. F. Dermott and C. D. Murray. The Dynamics of Tadpole and Horseshoe Orbits: II. The Coorbital Satellites of Saturn. *Icarus*, 48(1):12–22, October 1981.

[7] W. R. Johnson. SIM Trajectory Design. AIAA/AAS Astrodynamics Specialists Conference and Exhibit, AIAA 2004-5398, August 2004.

[8] K. C. Howell, J. M. Longuski, D. Craig Davis, C. Patterson, M. Kakoi, J. Chen, M. Okutsu, and C. H. Yam. Encore and End-of-Life Options for the Cassini Spacecraft. Final Report JPL 1283234, prepared for the Jet Propulsion Laboratory, February 2007.

[9] C. H. Yam, D. C. Davis, J. M. Longuski, and K. C. Howell. Saturn Impact Trajectories for Cassini End-of-Life. AAS/AIAA Astrodynamics Specialists Conference, Mackinac Island, Michigan, AAS 07-257, August 2007.

[10] D. C. Davis, C. Patterson, and K. C. Howell. Solar Gravity Perturbations to Facilitate Long-Term Orbits: Application to Cassini. AAS/AIAA Astrodynamics Specialists Conference, Mackinac Island, Michigan, AAS 07-275, August 2007.

[11] I. Newton. *The Principia: Mathematical Principals of Natural Philosophy*. University of California Press, Berkeley, California, 1999. Translation by I. B. Cohen and A. Whitman.

[12] F. Diacu. The Solution of the n-Body Problem. *The Mathematical Intelligencer*, 18:66–70, 1996.

[13] J. Barrow-Green. *Poincaré and the Three Body Problem*. The American Mathematical Society, Providence, Rhode Island, 1997.

[14] E. Rabe. Determination and Survey of Periodic Trojan Orbits in the Restricted Problem of Three Bodies. *The Astronomical Journal*, 66(9):500–513, November 1961.

[15] A. F. Schanzle. Horseshoe-Shaped Orbits in the Jupiter-Sun Restricted Problem. *The Astronomical Journal*, 72(2):149–157, March 1967.

[16] D. B. Taylor. Horseshoe Periodic Orbits in the Restricted Problem of Three Bodies for a Sun-Jupiter Mass Ratio. *Astronomy and Astrophysics*, 103:288–294, 1981.

[17] J. Llibre and M. Ollé. The Motion of Saturn Coorbital Satellites in the Restricted Three-Body Problem. *Astronomy and Astrophysics*, 378(3):1087–1099, November 2001.

[18] J. L. Junkins, P. Singla, M. Mortari, W. Bottke, and D. Durda. A Study of Six Near-Earth Asteroids. International Conference on Computational and Experimental Engineering and Sciences, INDIA, December 1-10, 2005.

[19] E. Barrabés and S. Mikkola. Families of Periodic Horseshoe Orbits in the Restricted Three-Body Problem. *Astronomy and Astrophysics*, 432(3):1115–1129, March 2005.

[20] E. Barrabés and M. Ollé. Invariant Manifolds of L_3 and Horseshoe Motion in the Restricted Three-Body Problem. *Nonlinearity*, 19(9):2065–2089, 2006.

[21] E. Barrabés, J. M. Mondelo, and M. Ollé. Dynamical Aspects of Multi-Round Horseshoe-Shaped Homoclinic Orbits in the RTBP. *Celestial Mechanics and Dynamical Astronomy*, 105(1-3):197–210, 2009.

[22] L. A. D'Amario and T. N. Edelbaum. Minimum Impulse Three-Body Trajectories. *AIAA Journal*, 12(4):455–462, 2009.

[23] G. Gómez, A. Jorba, J. Masdemont, and C. Simó. Study of the Transfer from the Earth to a Halo Orbit Around the Equilibrium Point L_1. *Astronomy and Astrophysics*, 103:288–294, 1981.

[24] K. C. Howell. Families of Orbits in the Vicinity of the Collinear Libration Points. *Journal of the Astronautical Sciences*, 49(1):107–125, January-March 2001.

[25] K. C. Howell, B. T. Barden, and M. W. Lo. Application of Dynamical Systems Theory to Trajectory Design for a Libration Point Mission. *Journal of the Astronautical Sciences*, 45(2):161–178, April-June 1997.

[26] K. C. Howell, D. L. Mains, and B. T. Barden. Transfer Trajectories from Earth Parking Orbits to Sun-Earth Halo Orbits. AAS/AIAA Spaceflight Mechanics Meeting, Cocoa Beach, Florida, AAS 94-160, February 1994.

[27] J. R. Stuart. Fuel-Optimal Low-Thrust Transfers Between Libration Point Orbits. M.S. Thesis, School of Aeronautics and Astronautics, Purdue University, May 2011.

[28] L. R. Irrgang. Investigation of Transfer Trajectories to and from the Equilateral Libration Points L_4 and L_5 in the Earth-Moon System. M.S. Thesis, School of Aeronautics and Astronautics, Purdue University, August 2008.

[29] D. J. Grebow. Trajectory Design in the Earth-Moon System and Lunar South Pole Coverage. Ph.D. Dissertation, School of Aeronautics and Astronautics, Purdue University, May 2010.

[30] T. Pavlak. Mission Design Applications in the Earth-Moon System: Transfer Trajectories and Stationkeeping. M.S. Thesis, School of Aeronautics and Astronautics, Purdue University, May 2010.

[31] A. E. Roy. *Orbital Motion*. Institute of Physics Publishing, Bristol, 4th edition, 2005.

[32] W. H. Press. *Numerical Recipes: The Art of Scientific Computing*. Cambridge University Press, New York, New York, 2007.

[33] V. V. Markellos and A. A. Halioulias. Numerical Determination of Asymmetric Periodic Solutions. *Astrophysics and Space Science*, 46:183–193, January 1977.

[34] H. B. Keller. Numerical Solution of Bifurcation and Nonlinear Eigenvalue Problems. In P. H. Rabinowitz, editor, *Applications of Bifurcation Theory*, pages 359–384. Academic Press, 1977.

[35] K. Chen. *Matrix Preconditioning Techniques and Applications*. Cambridge University Press, New York, New York, 2005.

[36] T. S. Parker and L. O. Chua. *Practical Numerical Algorithms for Chaotic Systems*. Springer-Verlag, New York, New York, 1989.

[37] K. E. Davis, R. L. Anderson, D. J. Scheeres, and G. H. Born. The Use of Invariant Manifolds for Transfers Between Unstable Periodic Orbits of Different Energies. *Celestial Mechanics and Dynamical Astronomy*, 107:471–485, June 2010.

[38] D. W. Jordan and P. Smith. *Nonlinear Ordinary Differential Equations: An Introduction to Dynamical Systems*. Oxford University Press Inc., New York, 3rd edition, 1999.

[39] J. D. Hadjidemetriou. Symmetric and Asymmetric Librations in Extrasolar Planetary Systems: A Global View. In A. Celletti and S. Ferraz-Mello, editors, *Periodic, Quasi-Periodic and Chaotic Motions in Celestial Mechanics: Theory and Applications*, pages 225–244. Springer, 2006.

[40] B. T. Barden. Using Stable Manifolds to Generate Transfers in the Circular Restricted Problem of Three Bodies. M.S. Thesis, School of Aeronautics and Astronautics, Purdue University, December 1994.

[41] L. Perko. *Differential Equations and Dynamical Systems*. Springer, New York, 3rd edition, 1991.

[42] A. F. Haapala. Trajectory Design Using Periapse Maps and Invariant Manifolds. M.S. Thesis, School of Aeronautics and Astronautics, Purdue University, December 2010.

[43] C. D. Murray and S. F. Dermott. *Solar System Dynamics*. Cambridge University Press Inc., Cambridge, United Kingdom, 1999.

[44] T. M. Vaquero Escribano. Poincaré Sections and Resonant Orbits in the Restricted Three-Body Problem. M.S. Thesis, School of Aeronautics and Astronautics, Purdue University, May 2010.

[45] J. E. Prussing. Simple Proof of the Global Optimality of the Hohmann Transfer. *Journal of Guidance, Control, and Dynamics*, 15(4):1037–1038, July-August 1992.

[46] V. A. Chobotov, editor. *Orbital Mechanics*. American Institute of Aeronautics and Astronautics, Inc., Reston, Virginia, 3rd edition, 2002.

[47] W. S. Koon, M. W. Lo, J. E. Marsden, and S. D. Ross. Heteroclinic Connections between Periodic Orbits and Resonance Transitions in Celestial Mechanics. *Chaos*, 10(2):471–485, 2000.

[48] J. Guckenheimer and P. Holmes. *Nonlinear Oscillations, Dynamical Systems, and Bifurcations of Vector Fields*. Springer-Verlag, New York, 1983.